The Dissertation Committee for Heedong Goh
certifies that this is the approved version of the following dissertation:

Inverse Design of Metamaterials for Wave Control

Committee:

Loukas F. Kallivokas, Supervisor

Andrea Alù

Brady Cox

Michael R. Haberman

Mark F. Hamilton

Lance Manuel

Inverse Design of Metamaterials for Wave Control

by

Heedong Goh

DISSERTATION

Presented to the Faculty of the Graduate School of

The University of Texas at Austin

in Partial Fulfillment

of the Requirements

for the Degree of

DOCTOR OF PHILOSOPHY

The University of Texas at Austin

May 2020

Dedicated to my wife, Soyoona

Acknowledgments

In case someone asks me how I earned this Ph.D. degree, I provide my response below.

First, I am extremely grateful to supervisor Professor Loukas F. Kallivokas for introducing me to the field of metamaterials, which fascinated me from the very first meeting, we had soon after I arrived in Austin. It was unfair of him to use Star Trek as an example to a fan of all science fiction. However, as he promised, the study was full of intriguing ideas and mathematical/physical enlightenments beyond what I initially comprehended from artistic figures and animations. For every meeting, reviewing the literature, developing ideas, writing drafts, etc., Professor Kallivokas was a strict and careful "detective" asking questions in detail to disambiguate thoughts. He always has been patient and respectful, allowing me to bring any questions, hypotheses, doubts, (misleading) ideas, and failures. I truly enjoyed and appreciated every meeting and discussion we had.

Professor Mark F. Hamilton responded, "Why?" when I asked him to serve as a committee member. I wasn't able to answer, although I had a clear answer that applies to all my committee members. I considered the Final Exam as a one-time-only privilege of a student to present and discuss one's work with the greatest audience in the most intensive environment. I would

like to express my appreciation to my committee members, Professor Andrea Alù, Professor Brady Cox, Professor Michael R. Haberman, Professor Mark F. Hamilton, and Professor Lance Manuel, for suggestions, clarifications, and insights, which improved my research and study significantly.

I would like to extend my gratitude to Professor Oguzhan Bayrak and Professor Robert Gilbert for kind supports and encouragement. I would also like to show my appreciation to Professor Hae Sung Lee for encouraging me to study abroad to pursue a Ph.D. degree.

I appreciate former and current students of Mechanics, Uncertainty, and Simulation in Engineering for being such good friends for the well-being of each other in the windowless lab. I want to thank Dr. Jae Sang Moon and Dr. Seungbum Koo for helping me immensely inside and outside of the office.

I thank Mr. Daniel Quiroz and Ms. Leslie A. McCroddan. I probably asked thousands of questions and requests throughout my Ph.D. study.

The University of Texas at Austin has many great courses. Thanks to the lectures I attended, I was able to strengthen my mathematical and engineering backgrounds.

I attended three seminars organized respectively by Oden Institute for Computational Engineering and Sciences, Texas Acoustics, and the Austin Chapter of the Korean-American Scientists & Engineers Association. I thank the organizers, speakers, and audiences.

I would like to acknowledge research grants, fellowships, and scholar-

ships from the University of Texas at Austin VP for Research Grants; the Department of Civil, Architectural and Environmental Engineering; OTEFE Foundation; the Ministry of Education, Republic of Korea; the United States Association for Computational Mechanics; and the British Columbia Hydro and Power Authority Corporation. I was also supported by working as a teaching assistant in various classes, which were always rewarding.

There were many other pleasant memories with friends in Structural Engineering and the Korean squash team. Many thanks to Taemin Heo, Euijin Yang, and Jong Won Ma for the birthday present. I was deeply touched and wasn't able to tell them, until now, that it wasn't my birthday.

I was fortunate to meet Dr. Donghan Shin, Dr. Hunyoung Shin, and Dr. Seongjoon Kang. With them, I share most of the good memories of my early years in Austin. I wonder when we will be able to meet in one place again.

I want to thank my paternal grandmother for calling me Dr. Goh from my earliest memory. I remember my maternal grandfather writing `DOS` commands on a whiteboard to teach my sister and me. Like he was, I also became an engineer who loves classical music and has curly hairs. I wish I could share my accomplishment with them.

I believe that I have the best father, mother, and sister, who gave endless supports to this big baby bird. I also have the best parents-in-law, who understand the value of a Ph.D. degree.

Finally, I would like to express my deepest gratitude to my Soyoona for everything, including her existence. I adore every place we went together because we went together. Every moment that we had together shaped my mind and body.

Soyoona, I am happy to be with you and will be happier with you. This dissertation is dedicated to you.

Inverse Design of Metamaterials for Wave Control

Heedong Goh, Ph.D.
The University of Texas at Austin, 2020

Supervisor: Loukas F. Kallivokas

Metamaterials are engineered materials, whose spatially periodic arrangement of their constituent materials endows the composite assembly with rather unconventional properties, when macroscopically observed. In the context of the three wave-supporting physics regimes –elastodynamics, acoustics, and electromagnetics– metamaterials present unique opportunities for previously unimaginable user control over the resulting wave behavior.

To date, the design of metamaterials is mostly done on an *ad hoc* basis, relying mostly on one-of-a-kind or incremental physical experiments and forward computational modeling.

This dissertation introduces a systematic methodology, rooted in *inverse problem theory*, for engineering the dispersive properties of periodic media to meet *a priori*, *user-defined*, *wave control objectives*. Both *scalar* and *vector* waves are considered.

In the developed methodology, the material properties and geometry parameters of the unit cell of the periodic medium become the inversion variables. The inversion is driven by the user-defined wave control objective, constrained by the dispersive characteristics of the unit cell.

Though the methodology is flexible enough and can accommodate fairly broad dispersion engineering objectives, here the focus is on band-gaping propagating waves at user-defined frequency ranges. Numerical results in the frequency domain demonstrate that the inversion process yields unit cells that indeed attain the user-defined dispersive behavior. The inverted-for unit cells are then used to build metamaterial assemblies of not only finite periodicity, as opposed to infinite, but of fairly *narrow periodicity*, and are tested in the time domain against broadband excitations: it is shown that it is possible to attain the desired wave control with sub-wavelength size metamaterial assemblies.

Table of Contents

List of Figures

Chapter 1

Introduction

This dissertation introduces a systematic method, rooted in inverse problem theory, for engineering the unit cell of a periodic medium as a means of controlling wave propagation within the medium.

A wave is a physical phenomenon that carries energy in space and time through a wave-supporting medium. In general, waves propagate with different speeds at different frequencies and/or along different directions: the particular wave behavior is dictated by the material composition and the geometry of the medium. Mathematically, the complex wave motion characteristics are uniquely and completely described by the medium's dispersion relation: thus, engineering the dispersive properties of a medium is a suitable vehicle for controlling energy propagation.

Engineering the dispersive properties of a unit cell of a periodic medium may result in unconventional behavior of the periodic assembly at the macro scale, effectively endowing the periodic medium with metamaterial status. Of particular interest in this dissertation are metamaterials that allow for band-gaping propagating waves –giving rise to wave steering, lensing or focusing, and shielding.

To engineer the unit-cell's dispersive behavior, we develop a design methodology that, mathematically, is cast as a dispersion-constrained inverse medium problem. The Lagrangian of the inverse problem consists of an objective functional and of the side-imposed Floquet-Bloch unit cell eigenvalue problem –the latter representing the physical constraint. Any suitably parameterized unit-cell material property or geometric quantity can be used as design or inversion variable. For example, herein, for the elastic metamaterial case, we used the Lamé parameters, the mass density, and geometric parameters as the design variables.

Selecting a suitable objective functional is challenging: when interested only in band-gap design, we propose the Floquet-Bloch problem discriminant as the objective functional, whereas for general dispersion engineering, we propose a group-velocity-based objective functional.

To validate the theoretical development, numerical results show that the inverse metamaterial design methodology can robustly render unit-cell designs achieving the user-defined target dispersive behavior, including unidirectional and, more importantly, omni-directional band-gaps, for the scalar, as well as the more challenging vector (elastic) wave case. Furthermore: we use time-domain experiments to demonstrate that, even though the unit-cell designs are predicated on infinite periodicity, metamaterial assemblies of fairly narrow periodicity can quite satisfactorily result in the target wave-controlling behavior, including steering and shielding.

1.1 Thesis organization

This dissertation consists of three journal articles on the inverse design of metamaterials for scalar and vector waves. Two of three articles have already been published, while the third one is under review.

Chapter 2 introduces an inverse approach for designing band-gap metamaterials for a given user-defined target frequency range. We propose using the discriminant of the quadratic form of the Floquet-Bloch eigenvalue problem to drive the inverse problem; the discriminant serves as a numerically robust identifier of propagating and non-propagating states for each eigenmode. We demonstrate the design method by inverting for the material properties of a unit cell supporting scalar waves.

Chapter 3 introduces an inverse approach for more general dispersion engineering of metamaterials. Here, the inversion is driven by a user-defined group velocity profile, thus allowing wave control objectives that include, yet transcend band gaps. The method is demonstrated by designing material properties of unit cells for scalar wave control.

Chapter 4 extends the group velocity-driven inversion approach of the preceding chapter to the more challenging problem of vector waves. We show that the proposed design method can simultaneously control P and SV waves in elastodynamics. Uni- and omnidirectional band-gap designs are realized, while various time-domain analyses are used to demonstrate the efficacy of the designs in wave steering and shielding.

The methodology outlined in Chapters 2 to 4 focuses on inversion for the material properties of the unit cell; in Chapter 5, we extend the methodology to encompass unit-cell geometric parameters as inversion variables.

Concluding remarks are discussed in Chapter 6.

Chapter 2

Inverse metamaterial design for controlling band gaps in scalar wave problems[1]

We are concerned with the design of metamaterials capable of exhibiting a user-defined frequency band gap in periodic media supporting scalar waves. We cast the metamaterial design problem as an inverse medium problem, and seek to reveal the properties of the metamaterial unit cell that would enforce the gap. To drive the inversion, we use a scalar objective functional –the negativity of a discriminant of the coefficients of a quadratic wavenumber eigenvalue problem– that defines uniquely the evanescent state associated with the gap. We use the medium's dispersion characteristics to side-impose the underlying wave physics in the objective functional, and demonstrate the proposed inverse metamaterial design with numerical examples in both the frequency and time domains for the scalar wave case in one and two dimensions. The approach is systematic and can be generalized to the vector wave case, provided that the eigenvalue problem remains Hermitian.

[1]This chapter has been published in: Heedong Goh and Loukas F. Kallivokas, Inverse metamaterial design for controlling band gaps in scalar wave problems, *Wave Motion*, 88:85–105, 2019. The dissertation author had significant contributions to the article that included the development of the methodology, its implementation, the numerical results, and the related discussion.

2.1 Introduction

The need to design materials capable of exhibiting band gaps is driven, with increasing intensity, by applications in various engineering fields: whereas electronic band gaps have long been central to developments in the semiconductor industry [29], applications involving photonic and phononic crystals are currently driving novel applications in sensing and imaging [35,45]. A photonic crystal and a phononic crystal are spatially periodic composite structures capable of exhibiting electromagnetic or acoustic band gaps, respectively. In this context, a band gap is a frequency range where the propagation of waves is arrested. The crystal's spatially periodic structure is realized by assemblies of unit cells; typically, each unit cell is itself heterogeneous, with spatially varying optical or acoustic properties. Whereas the unit cell's constituent materials are real, the crystal's homogenized properties may assume non-physical values, thus granting metamaterial status to the crystal. Depending on the type of crystal, the wave type to be arrested in a band gap is different: de Broglie waves in the "electronic" crystal case, electromagnetic and sound waves, in the photonic and phononic crystal cases, respectively. Band-gap behavior similar to that exhibited in photonic or phononic crystals is also possible for elastic waves in elastic metamaterials. Whereas the one-dimensional elastic band-cap case is very similar to the photonic and phononic crystal cases, designing materials to exhibit band gaps in higher dimensions remains a challenge due to the presence of multiple directions and of different wave types that travel at different velocities (e.g., shear and compressional waves).

Most of the early studies on band-gap materials were the purview of solid-state physics (the electronic band gap) [4,29]. The photonic crystal case, and more recently the phononic case, have seen considerable development, especially since technological challenges in the fabrication of the crystals were overcome [33, 40]. More generally, the interest in understanding how waves interact with periodic structures possibly predates all the aforementioned developments and it seems to have originated in studies of the behavior of elastic or stress waves in periodic structures [8]. Irrespective of the underlying physics, the inverse design problem, or equivalently, the question of what should the unit cell be made of in order to deliver a prescribed or desired band gap has not been systematically addressed, relying mostly on *ad hoc* approaches, with very few exceptions [48, 52, 53, 56, 62].

In this paper, we are concerned with devising one such systematic approach for the material design of a metamaterial unit cell, when given a target design band gap. Herein, we focus exclusively on the scalar wave problem, which is common to acoustics, particular polarization cases in electromagnetics (e.g., TE or TM cases), and elastodynamics (e.g., SH case). Since the goal is to construct the spatial distribution of material properties driven by given data (or a sought performance outcome), the problem belongs to the class of inverse medium problems encountered in various other fields (e.g., geophysics): we thus borrow from our own past developments in the treatment of inverse medium problems using PDE-constrained optimization [18, 28], with suitable modifications to accommodate the band-gap objective. Specifically, we show

that the negativity of the discriminant of the coefficients of the problem's eigenvalue problem (cast in terms of the wavenumber) is sufficiently unique in delineating the band gap, and thus is a good choice to base the objective functional on. To form the Lagrangian, instead of side-imposing the governing PDE, we augment the objective functional with the side imposition of the problem's dispersion characteristics, or equivalently, the eigenvalue problem. Following the satisfaction of the first-order optimality conditions, the properties of the unit cell are obtained, leading to a metamaterial exhibiting the target band gap. We demonstrate the methodology with numerical results, leading to unit cell designs with either piecewise constant properties, or made of functionally-graded materials, in one and two spatial dimensions.

2.2 Preliminaries

To justify the particular choice of the objective functional that would drive the inversion for the metamaterial unit cell, we discuss first the dynamics of a periodic structure that lead to an eigenvalue problem for the unit cell. The eigenvalue problem characterizes fully the dispersion behavior and the frequency band structure of the metamaterial.

2.2.1 Bloch theorem and Bloch boundary condition

Consider the one-dimensional elastic metamaterial shown in Fig. 2.1, consisting of one-dimensional unit cells. In the frequency domain, the wave propagation within the metamaterial is governed by the one-dimensional scalar

Helmholtz equation:

$$\frac{\partial}{\partial x}\left[\mu(x)\frac{\partial}{\partial x}U(x)\right] + \omega^2\rho(x)\,U(x) = 0, \quad \forall x \in \mathbb{R}, \tag{2.1}$$

where ω is a temporal frequency and the two material properties μ (elastic modulus) and ρ (mass density) are periodic with periodicity p, i.e., $\mu(x+p) = \mu(x)$, and $\rho(x+p) = \rho(x)$; consequently, the Helmholtz operator in (2.1) is periodic. Then, by virtue of the Bloch theorem [4], the wavefunctions $U(x)$ that are solutions to (2.1) are Bloch waves, i.e.:

$$U(x) = e^{\mathrm{i}kx}u(x), \tag{2.2}$$

where $u(x+p) = u(x)\ \forall x$, and k is the (Bloch) wavenumber. Expression (2.2) leads also to the Bloch boundary condition:

$$U(x+p) = e^{\mathrm{i}kp}U(x), \tag{2.3}$$

which permits consideration of the unit cell only.

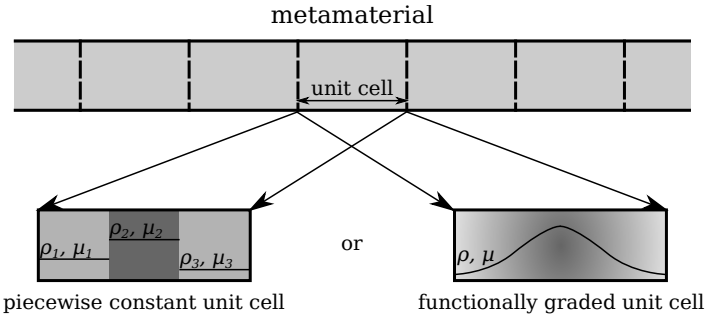

Figure 2.1: Typical one-dimensional metamaterial

We note that (2.1) is equally applicable to the acoustic, electromagnetic (polarized cases), and elastic cases, with different ascription of physical meaning to the material properties ρ and μ [33].

2.2.2 Eigenvalue problems and band structures

Next, we are interested in deriving the unit cell's eigenvalue problem. Since we intend to use finite elements for the numerical treatment of the inverse material design problem, the eigenvalue problem is derived in a weak or weighted-residual sense: we multiply (2.1) by a test function $V(x)$, where $V(x) = e^{\mathrm{i}\overline{k}x}v(x)$, with $v(0) = v(p)$, and a bar $\overline{(\cdot)}$ over a variable denoting complex-conjugation of the subtended quantity. Then:

$$\begin{aligned}
0 &= \int_0^p \overline{V}\left[\frac{\partial}{\partial x}\left(\mu\frac{\partial U}{\partial x}\right) + \omega^2\rho\, U\right] dx \\
&= \overline{V}\mu\frac{\partial U}{\partial x}\bigg|_{x=0}^{x=p} - \int_0^p \left[\frac{\partial \overline{V}}{\partial x}\mu\frac{\partial U}{\partial x} - \overline{V}\omega^2\rho\, U\right] dx \\
&= \overline{V}\mu\left(e^{\mathrm{i}kx}\mathrm{i}ku + e^{\mathrm{i}kx}\frac{\partial u}{\partial x}\right)\bigg|_{x=0}^{x=p} \\
&\quad - \int_0^p \left[\frac{\partial \overline{V}}{\partial x}\mu\left(e^{\mathrm{i}kx}\mathrm{i}ku + e^{\mathrm{i}kx}\frac{\partial u}{\partial x}\right) - \overline{V}\omega^2\rho\, e^{\mathrm{i}kx}u\right] dx. \qquad (2.4)
\end{aligned}$$

Equation (2.4) is a Hermitian form, which yields the Bloch eigenvalue problem [6, 27] in a weak sense:

$$0 = \int_0^p \left[\left(-\mathrm{i}k\overline{v} + \frac{\partial \overline{v}}{\partial x}\right)\mu\left(\mathrm{i}ku + \frac{\partial u}{\partial x}\right) - \overline{v}\omega^2\rho u\right] dx. \qquad (2.5)$$

In the above $u, v \in \mathcal{V}$, where $\mathcal{V}$ is defined as:

$$\mathcal{V} = \left\{u \in H^1(0,p)\middle|, u(0) = u(p)\right\}. \qquad (2.6)$$

There are two paths one can follow to obtain the band structure from the eigenvalue problem: for a given wavenumber k, one can solve for ω^2, which gives rise to a linear eigenvalue problem, or, alternatively, one can solve for the wavenumber k for a given ω, which gives rise to a quadratic eigenvalue problem.

A classical band structure, as that shown in Fig. 2.2(a), results from the solution of the linear eigenvalue problem: in the figure, $\hat{\omega} = \omega p/c_a$ and $\hat{k} = kp/\pi$ are normalized frequency and wavenumber, respectively, where c_a is an average wave velocity. The bands are symmetric about the origin of the Brillouin zone[2] Γ, and they are periodic. Thus, the bands between Γ and the center of the face X contain all the information of the band structure. We note that to solve the linear eigenvalue problem, we use real-valued wavenumbers k, and since the associated forms are Hermitian, ω^2 is always real-valued. Therefore, the resulting classical band structure can express propagating states only, with the evanescent states corresponding to band gaps that are only indirectly recoverable: the shadowed region in Fig. 2.2(a) corresponds to a no-solution condition for ω. Due to the above indirect definition of the band gap, the linear eigenvalue problem does not appear to be the best driver for the inverse problem. By contrast, the quadratic eigenvalue problem offers a direct definition of the evanescent state/band gap, as is discussed next. We note that, in the quadratic eigenvalue problem, for a given (real) ω, we solve

[2]The Brillouin zone is a unit cell in the spatial Fourier transform of the periodic domain. The first Brillouin zone contains the origin $\hat{k} = 0$, which is denoted by Γ. The boundary of the first Brillouin zone $\hat{k} = 1$, or the center of the face, is denoted by X.

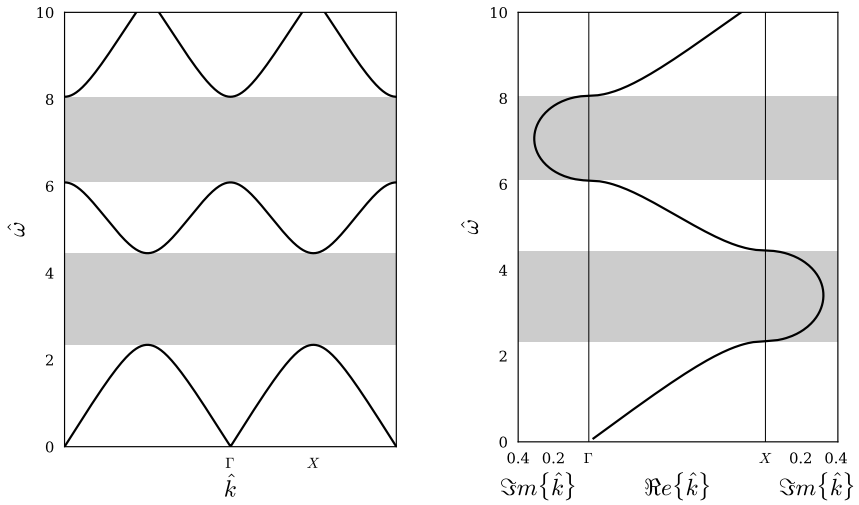

(a) Classical band structure (b) Complex band structure

Figure 2.2: Band structures: (a) The classical band structure plotted using the periodic zone scheme. (b) The complex band structure plotted using the reduced zone scheme; $\mathrm{Re}\{\hat{k}\}$ is in the middle panel, the non-zero $\mathrm{Im}\{\hat{k}\}$ for $\mathrm{Re}\{\hat{k}\} = 0$ is in the left panel, and the non-zero $\mathrm{Im}\{\hat{k}\}$ for $\mathrm{Re}\{\hat{k}\} = 1$ is in the right panel. Band gaps correspond to the shadow zones.

for k, which is, in general, complex. To illustrate, we rearrange the weak form (2.5) to yield the quadratic eigenvalue problem:

Given $\omega \in \mathbb{R}$, find $k \in \mathbb{C}$ and $u \in \mathcal{V} \setminus \{0\}$ such that:

$$0 = a_0(v,u) + k a_1(v,u) + k^2 a_2(v,u) \equiv P(k)(v,u), \ \forall v \in \mathcal{V} \tag{2.7}$$

where

$$a_0(v,u) = \int_0^p \left(\frac{\partial \overline{v}}{\partial x} \mu \frac{\partial u}{\partial x} - \omega^2 \overline{v} \rho u \right) dx, \tag{2.8a}$$

$$a_1(v,u) = \int_0^p \mathrm{i} \left(\frac{\partial \overline{v}}{\partial x} \mu u - \overline{v} \mu \frac{\partial u}{\partial x} \right) dx, \text{ and} \tag{2.8b}$$

$$a_2(v,u) = \int_0^p \overline{v} \mu u dx. \tag{2.8c}$$

Fig. 2.2(b) depicts the band structure resulting from the quadratic eigenvalue problem, where, because of the symmetry and the periodicity, the band structure is plotted only between Γ and X. We note that the band gaps correspond to the regions where $\Im m\{\hat{k}\}$ is non-zero; in particular, the left panel corresponds to $\mathrm{Re}\{\hat{k}\} = 0$, whereas the right panel corresponds to $\Re e\{\hat{k}\} = 1$. Clearly, whether recovered by the linear or the quadratic eigenvalue problems, the band gaps coincide, as shown in Fig. 2.2(a) and Fig. 2.2(b), respectively. However, the quadratic eigenvalue problem offers a sharper criterion for establishing the band gap than its linear counterpart, as it can be readily seen in Fig. 2.2(b): the criterion is a non-zero imaginary wavenumber part, which will be further exploited in defining the objective functional.

2.2.3 Eigenvalue problem discriminant

We revisit the eigenvalue problem (2.7) and replace the test function v with the eigenfunction u: there results a simple quadratic equation in the wavenumber k, i.e.,

$$\begin{aligned} 0 =& P(k)(u,u) \\ =& a_0(u,u) + k a_1(u,u) + k^2 a_2(u,u) \\ =& c + bk + ak^2, \end{aligned} \tag{2.9}$$

where the coefficients $a = a_2(u,u)$, $b = a_1(u,u)$, and $c = a_0(u,u)$ are always real-valued because they are the products of Hermitian forms operating on the same function. Then, the solutions of (2.9) are obtained by the quadratic formula:

$$k = \frac{-b \pm \sqrt{b^2 - 4ac}}{2a}, \tag{2.10}$$

where the discriminant $\mathcal{D}$ is defined as:

$$\mathcal{D} = b^2 - 4ac. \tag{2.11}$$

The negativity of the discriminant (2.11) ensures a non-zero imaginary part for the wavenumber: the latter was associated in the previous section with the presence of a band gap. Fig. 2.3 depicts the discriminant as a function of the temporal frequency ω, side-by-side with the band structure. Clearly, positive discriminants are associated with propagating states, while negative discriminants appear at evanescent states.

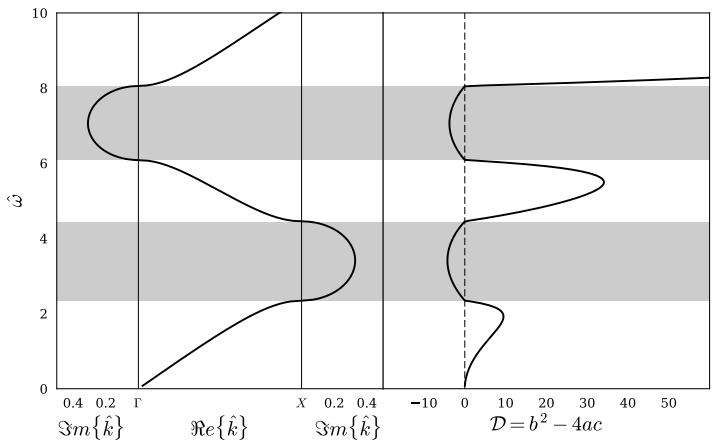

Figure 2.3: A typical band structure (left) and the discriminant of the associated quadratic eigenvalue problem (right): the discriminants are real-valued and are smoothly varying over the frequency range. Negative discriminants correspond to band gaps (shaded zones).

Thus, in summary, band gaps are equivalently characterized by either wavenumbers with non-zero imaginary parts or by negative discriminants, for a given temporal frequency. Either of the two band-gap indicators ($\text{Im}\{k\} \neq 0$ or $D < 0$) could be used to drive the inverse metamaterial design: however, only the discriminant-based indicator allows for differentiable objective functionals.

2.3 Inverse metamaterial design in 1D

2.3.1 Discriminant-based objective functional

Suppose we want to design a material that exhibits a band gap at frequencies between ω_s and ω_f. Then, the design goal in terms of the discriminant becomes:

Find ρ and μ such that

$$\mathcal{D} < 0,\ \omega \in (\omega_s, \omega_f), \tag{2.12}$$

or, by restating the above inequality problem as a minimization problem: Given $\omega_i \in (\omega_s, \omega_f)$, find ρ and μ such that:

$$\min D\left[\rho, \mu, u\right]. \tag{2.13}$$

The target band-gap interval is discretized into N frequencies $\omega^{(i)}$, with $i = 1, 2, \ldots, N$. Then, given $\omega^{(i)} \in (\omega_s, \omega_f)$, the objective functional can be written as:

$$D\left[\rho, \mu, u\right] = \sum_{i}^{N} \mathcal{D}_0^{(i)} \left[\rho, \mu, u_0^{(i)}\right], \text{ where} \tag{2.14a}$$

$$\begin{aligned} \mathcal{D}_0^{(i)} \left[\rho, \mu, u_0^{(i)}\right] = & a_1\left(u_0^{(i)}, u_0^{(i)}\right) a_1\left(u_0^{(i)}, u_0^{(i)}\right) \\ & - 4a_2\left(u_0^{(i)}, u_0^{(i)}\right) a_0\left(u_0^{(i)}, u_0^{(i)}\right). \end{aligned} \tag{2.14b}$$

In the above, we use $u_0^{(i)}$ to denote the fundamental eigenfunction at each frequency $\omega^{(i)}$, and u to represent the set of all $u_0^{(i)}$ across the target band gap. Similarly, $\mathcal{D}_0^{(i)}$ denotes the i-th discriminant of the fundamental mode eigenvalue problem. In one spatial dimension, the objective functional consists of the sum of the fundamental-mode discriminants $\mathcal{D}_0^{(i)}$ at the target frequencies $\omega^{(i)}$, and was proven sufficient for driving the inverse design. However, the fundamental mode may not be sufficient for waves in higher spatial dimensions, as is discussed in section 2.4, where suitable augmentations are presented.

2.3.2 The Lagrangian and the dispersion constraint

Resolution of the minimization problem (2.13) requires the direct sensitivity analysis of the objective functional D. Alternatively, an adjoint method could be enlisted to compute the gradient that drives the material parameter updates during the inversion process. To this end, the objective functional D could be augmented by the side imposition of a constraint – typically, a mathematical description of the underlying wave physics. Such an often-used constraint is the problem's partial differential equation (e.g., [18, 28]); here we opt to instead use the associated eigenvalue problem, effectively constraining the minimization by the dispersive properties of the target medium (e.g., [1, 36]). The resulting Lagrangian functional becomes:

$$L\left[\rho,\mu,u,k,v,\xi\right] = D\left[\rho,\mu,u\right] + E\left[\rho,\mu,u,k,v,\xi\right], \tag{2.15}$$

where the constraint $E\left[\rho,\mu,u,k,v,\xi\right]$ is defined as:

$$\begin{aligned} E\left[\rho,\mu,u,k,v,\xi\right] = &\sum_{i}^{N} \mathrm{Re}\left\{P\left(k_0^{(i)}\right)\left(v_0^{(i)},u_0^{(i)}\right)\right\} \\ &+ \sum_{i}^{N} \frac{\xi_0^{(i)}}{2}\left[a_2\left(u_0^{(i)},u_0^{(i)}\right) - 1\right]. \end{aligned} \tag{2.16}$$

In (2.16), $u_0^{(i)}$ is the fundamental mode eigenfunction (or the eigenfunction that is associated with the smallest eigenvalue), $k_0^{(i)}$ is the corresponding fundamental eigenvalue, $v_0^{(i)}$ is an adjoint eigenfunction, and $\xi_0^{(i)}$ is an adjoint variable at each frequency $\omega^{(i)}$ (the sets of all $k_0^{(i)}$, $\xi_0^{(i)}$, and $v_0^{(i)}$ are denoted by k, ξ, and v, respectively). Thus, the first term in (2.16) is the eigenvalue problem (2.7); without loss of generality, we impose the real part of the eigenvalue

problem to ensure its derivative is real-valued. The second term in (2.16) is the orthonormality condition that would guarantee a unique solution for the eigenvectors. With the above definition for the Lagrangian, the inverse design problem (2.13) is replaced by:

$$\min L\left[\rho, \mu, u, k, v, \xi\right]. \tag{2.17}$$

The minimization of the Lagrangian L would ensure the simultaneous minimization of the objective functional D (band-gap goal), and the satisfaction of the eigenvalue problem.

2.3.3 Optimality conditions

Next, we seek a stationary point of the Lagrangian (2.15) by requiring the satisfaction of the first-order optimality conditions. Accordingly, the first (Gâteaux) derivatives of L with respect to the state variables, to the adjoint variables, and to the (unknown) design material variables, are forced to vanish. The derivatives with respect to the adjoint variables lead to the state eigenvalue problem, whereas the derivatives with respect to the state variables lead to the adjoint eigenvalue problem. The derivatives with respect to the design variables lead to a control problem, from which we obtain the gradient of L for given trial designs of ρ and μ. The definitions of the derivatives are given in appendix section 2.8; here, we provide the final form of the optimality conditions:

1. **State eigenvalue problem**

   Given trials ρ and μ, find $k_0^{(i)} \in \mathbb{C}$ and $u_0^{(i)} \in \mathcal{V} \setminus \{0\}$ such that

$$0 = P\left(k_0^{(i)}\right)\left(\tilde{v}_0^{(i)}, u_0^{(i)}\right) \ \forall \tilde{v}_0^{(i)} \in \mathcal{V} \tag{2.18a}$$

$$0 = \frac{\tilde{\xi}_0^{(i)}}{2}\left[a_2\left(u_0^{(i)}, u_0^{(i)}\right) - 1\right] \ \forall \tilde{\xi}_0^{(i)} \in \mathbb{R}. \tag{2.18b}$$

2. **Adjoint eigenvalue problem**

   Given trials ρ, μ, and state variables $k_0^{(i)}$ and $u_0^{(i)}$, find $\xi_0^{(i)} \in \mathbb{R}$ and $v_0^{(i)} \in \mathcal{V}$ such that

$$\begin{aligned} 0 =& P\left(k_0^{(i)}\right)\left(v_0^{(i)}, \tilde{u}_0^{(i)}\right) + \xi_0^{(i)} a_2\left(u_0^{(i)}, \tilde{u}_0^{(i)}\right) + 4a_1\left(u_0^{(i)}, u_0^{(i)}\right) a_1\left(u_0^{(i)}, \tilde{u}_0^{(i)}\right) \\ & - 8a_2\left(u_0^{(i)}, u_0^{(i)}\right) a_0\left(u_0^{(i)}, \tilde{u}_0^{(i)}\right) - 8a_0\left(u_0^{(i)}, u_0^{(i)}\right) a_2\left(u_0^{(i)}, \tilde{u}_0^{(i)}\right) \\ & \qquad \forall \tilde{u}_0^{(i)} \in \mathcal{V} \end{aligned} \tag{2.19a}$$

$$0 = \tilde{k}_0^{(i)} a_1\left(v_0^{(i)}, u_0^{(i)}\right) + 2\tilde{k}_0^{(i)} k_0^{(i)} a_2\left(v_0^{(i)}, u_0^{(i)}\right) \ \forall \tilde{k}_0^{(i)} \in \mathbb{C}. \tag{2.19b}$$

3. **Gradient of L**

   Given trials ρ, μ, state variables $k_0^{(i)}$ and $u_0^{(i)}$, adjoint variables $\xi_0^{(i)}$ and $v_0^{(i)}$, find $g_\rho \in \mathcal{S}$ and $g_\mu \in \mathcal{S}$ such that

$$\begin{aligned} \int_0^p \tilde{\rho}\, g_\rho dx =& \sum_i^N \mathrm{Re}\left\{4a_2\left(u_0^{(i)}, u_0^{(i)}\right) \int_0^p \overline{u}_0^{(i)} \omega^2 \tilde{\rho}\, u_0^{(i)} dx\right\} \\ & - \sum_i^N \mathrm{Re}\left\{\int_0^p \overline{v}_0^{(i)} \omega^2 \tilde{\rho}\, u_0^{(i)} dx\right\} \ \forall \tilde{\rho} \in \mathcal{S} \end{aligned} \tag{2.20a}$$

$$\int_0^p \tilde{\mu}\, g_\mu dx = \sum_i^N \mathrm{Re}\left\{ 2a_1\left(u_0^{(i)}, u_0^{(i)}\right) \int_0^p \mathrm{i}\left(\frac{\partial \overline{u}_0^{(i)}}{\partial x}\tilde{\mu}\, u_0^{(i)} - \overline{u}_0^{(i)}\tilde{\mu}\frac{\partial u_0^{(i)}}{\partial x}\right) dx \right\}$$
$$- \sum_i^N \mathrm{Re}\left\{ 4a_2\left(u_0^{(i)}, u_0^{(i)}\right) \int_0^p \frac{\partial \overline{u}_0^{(i)}}{\partial x}\tilde{\mu}\frac{\partial u_0^{(i)}}{\partial x} dx \right\}$$
$$- \sum_i^N \mathrm{Re}\left\{ 4a_0\left(u_0^{(i)}, u_0^{(i)}\right) \int_0^p \overline{u}_0^{(i)}\tilde{\mu}\, u_0^{(i)} dx \right\}$$
$$+ \sum_i^N \mathrm{Re}\left\{ k_0^{(i)} \int_0^p \mathrm{i}\left(\frac{\partial \overline{v}_0^{(i)}}{\partial x}\tilde{\mu}\, u_0^{(i)} - \overline{v}_0^{(i)}\tilde{\mu}\frac{\partial u_0^{(i)}}{\partial x}\right) dx \right\}$$
$$+ \sum_i^N \mathrm{Re}\left\{ \int_0^p \frac{\partial \overline{v}_0^{(i)}}{\partial x}\tilde{\mu}\frac{\partial u_0^{(i)}}{\partial x} dx \right\}$$
$$+ \sum_i^N \mathrm{Re}\left\{ \left(k_0^{(i)}\right)^2 \int_0^p \overline{v}_0^{(i)}\tilde{\mu}\, u_0^{(i)} dx \right\}$$
$$+ \sum_i^N \mathrm{Re}\left\{ \frac{\xi_0^{(i)}}{2} \int_0^p \overline{u}_0^{(i)}\tilde{\mu}\, u_0^{(i)} dx \right\} \quad \forall \tilde{\mu} \in \mathcal{S}, \tag{2.20b}$$

where

$$\mathcal{S} = \left\{ u \in H^0(0,p) | u(0) = u(p) \right\}, \tag{2.21}$$

and g_ρ and g_μ are the Fréchet derivatives, or gradients, of L with respect to ρ and μ, respectively.

The search directions d_ρ and d_μ are constructed from the gradients g_ρ and g_μ, and the properties are then updated using any gradient-based scheme [49], e.g., steepest descent, conjugate gradient, etc. Given appropriate

step sizes α_ρ and α_μ, the material profiles are updated by

$$\rho \leftarrow \rho + \alpha_\rho d_\rho, \tag{2.22a}$$

$$\mu \leftarrow \mu + \alpha_\mu d_\mu. \tag{2.22b}$$

The overall inversion algorithm, including the computational details for the search directions and the step sizes, is discussed in section 2.3.5.

2.3.4 Band gap width control

An algorithm based on the described minimization of the Lagrangian would, in general, drive the discriminants for the band gap frequencies to negative territory, but would not necessarily stop from enlarging the band gap beyond the target regime, since no stopping criterion has been prescribed thus far. In this section, we discuss two approaches for limiting the band-gap width to the target size.

The simplest method is to implement a termination criterion by monitoring the negativity of the discriminants $\mathcal{D}_0^{(i)}$ at discrete frequencies $\omega^{(i)}$ within the target band gap. Let N_D denote the number of frequencies at which the discriminant becomes negative. Then, the inversion is terminated when

$$N_D \geq N, \tag{2.23}$$

i.e., when the number of frequencies at which the discriminant becomes negative exceeds the number of discrete frequencies within the target band gap.

Alternatively, one could replace the summations in (2.14) and (2.16)

with conditional summations, per:

$$D\left[\rho,\mu,u\right] = \sum_{i \mid \mathcal{D}_0^{(i)}>0}^{N} \mathcal{D}_0^{(i)} \quad \text{and} \tag{2.24}$$

$$E\left[\rho,\mu,u,k,v,\xi\right] = \sum_{i \mid \mathcal{D}_0^{(i)}>0}^{N} \mathrm{Re}\left\{P\left(k_0^{(i)}\right)\left(v_0^{(i)},u_0^{(i)}\right)\right\} + \sum_{i \mid \mathcal{D}_0^{(i)}>0}^{N} \frac{\xi_0^{(i)}}{2}\left[a_2\left(u_0^{(i)},u_0^{(i)}\right)-1\right]. \tag{2.25}$$

That is, the summations are carried only over the number of frequencies within the target band gap for which the associated (fundamental mode) discriminant is positive. By definition, the objective functional (2.24) has a lower bound (zero): the inversion process stops automatically when the discriminant becomes negative for every frequency $\omega^{(i)}$ in the target band gap. This second method is particularly useful for higher-dimensional problems, as it will be shown, where multiple modes and multiple directions are present.

In reporting numerical results, we used the first stopping criterion (2.23) for one-dimensional problems, and the second criterion (2.24)-(2.25) for two-dimensional problems.

2.3.5 Inversion process

We discuss next the inversion process that iteratively updates the unit cell properties to yield a metamaterial assembly capable of exhibiting a prescribed band gap. Other inverse design problems can be similarly accommodated depending on particular manufacturing constraints that may limit the

range of considered material properties.

First, we choose initial guesses ρ_0 and μ_0 for the material properties ρ and μ. Then, using the trial material properties, the state eigenvalue problem (2.18) is solved to obtain the state variables $k_0^{(i)}$ and $u_0^{(i)}$. Then, using the state variables and the trial properties, the adjoint eigenvalue problem (2.19) is solved to obtain the adjoint variables $\xi_0^{(i)}$ and $v_0^{(i)}$. Next, armed with both the state and adjoint variables, the reduced gradient of the Lagrangian L is computed, per (2.20). The search directions for the material properties are obtained from the gradient of L using any gradient-based scheme; here, we opt for a nonlinear conjugate gradient method [21, 49]. The step size is obtained using a backtracking algorithm [49], and, finally, the properties are updated using (2.22). The process is repeated until the inverted material satisfies the termination criterion (2.23). We also stop the iterations when the backtracking algorithm fails to satisfy the sufficient-decrease condition; in such a case, we restart the inversion with different initial search length or initial guess for the material properties.

The most computationally-intensive parts of the inversion process are the state and the adjoint solutions, which contain N number of eigenvalue solutions, and N number of linear system solutions. However, the computation of the eigenvalue solution and the linear system solution for each frequency $\omega^{(i)}$ in the target band gap is independent from each other, and thus, the inversion process can be efficiently parallelized.

The details of the inversion process are listed in Algorithm 1.

Algorithm 1 Inversion process

1: Define the frequency range and the number of frequency points N in the target band gap
2: Define the geometry of the unit cell (e.g. period, number of distinct material elements, etc.)
3: Set the initial search length
4: Set initial guess for the material properties ρ_0 and μ_0
5: Set $N_D = 0$
6: Initialize the iteration counter $l \leftarrow 0$
7: **for** $N_D < N$ **do**
8: Solve the state eigenvalue problem ▷ equation (2.18)
9: Compute N_D ▷ equation (2.23)
10: Solve the adjoint eigenvalue problem ▷ equation (2.19)
11: Compute the gradient of L ▷ equation (2.20)
12: Obtain the search direction (e.g., conjugate gradient method)
13: Update the material properties ρ_{l+1} and μ_{l+1} using backtracking algorithm; stop if sufficient-decrease condition is violated
14: Set $l \leftarrow l + 1$.
15: **end for**

2.3.6 Extensions for topology design

Thus far, in the outlined inversion methodology, it is only the material parameters ρ and μ that have been considered as unknown design variables, whereas the topology of the unit cell has been considered fixed (the material thicknesses are set *a priori*). However, the same framework can be used to accommodate unknown thicknesses (or, more generally, unknown topology), with the addition of an equality constraint to the Lagrangian (the sum of the thicknesses must equal the size of the unit cell), and suitable modifications to the control problem. Specifically, of the three optimality conditions discussed in section 2.3.3, the state and adjoint eigenvalue problems would remain the same, but the gradients of L (the control problem) would have to be complemented by the derivatives of L with respect to the unknown thicknesses. Thus, it would be possible to simultaneously invert for both the topology and the properties, using the same discriminant-based objective functional.

2.4 Generalization to higher spatial dimensions

We claim that the discriminant-based objective functional (2.14) can also be used to drive the inverse design problem for scalar waves in higher dimensions, since the negativity of the discriminant is still a unique indicator of a band gap owing to the fact that the associated sesquilinear forms, $a_0(v,u)$, $a_1(v,u)$, and $a_2(v,u)$, remain Hermitian. Higher spatial dimensions introduce additional complexities associated with the presence of multiple directions (in wavenumber space), and multiple modes. Yet, as it will be discussed, the inver-

sion framework presented in section 2.3 is capable of accommodating multiple modes and multiple user-defined directions, including omni-directional band gap targets.

To fix ideas, consider the n-dimensional ($n = 2, 3$) scalar Helmholtz equation:

$$\text{div } [\mu(\boldsymbol{x})\text{grad}\, U(\boldsymbol{x})] + \omega^2 \rho(\boldsymbol{x}) U(\boldsymbol{x}) = 0, \ \forall \boldsymbol{x} \in \mathbb{R}^n, \tag{2.26}$$

with the periodicity relations $\mu\left(\boldsymbol{x} + \sum_{i=1}^{n} m_i \mathbf{p}_i\right) = \mu(\boldsymbol{x})$ and $\rho\left(\boldsymbol{x} + \sum_{i=1}^{n} m_i \mathbf{p}_i\right)$ $= \rho(\boldsymbol{x})$, $\forall m_i \in \mathbb{Z}$; $\mathbf{p}_i \in \mathbb{R}$ are primitive lattice vectors, which define the meta-material topology when given a unit cell. Then, the Bloch theorem suggests

$$U(\boldsymbol{x}) = u(\boldsymbol{x}) e^{\mathbf{i}\mathbf{k}\cdot\boldsymbol{x}}, \tag{2.27}$$

where $u\left(\boldsymbol{x} + \sum_{i=1}^{n} m_i \mathbf{p}_i\right) = u(\boldsymbol{x})$, and $\mathbf{k}$ denotes wavevector.

2.4.1 Eigenvalue problem and band structure

Following lines similar to those described in section 2.2.2, and while setting $\mathbf{k} = k\mathbf{d} + \mathbf{d}_0$, we obtain the weak form of the quadratic eigenvalue problem corresponding now to the n-dimensional equation (2.26):

Given ω, $\mathbf{d}$, and $\mathbf{d}_0$, find $k \in \mathbb{C}$ and $u \in \mathcal{W} \setminus \{0\}$ such that

$$0 = a_0(v, u) + k a_1(v, u) + k^2 a_2(v, u) \equiv P(k)(v, u) \ \ \forall v \in \mathcal{W}, \tag{2.28}$$

where

$$\mathcal{W} = \left\{ u \in H^1(\Omega) \middle| u(\boldsymbol{x}) = u\left(\boldsymbol{x} + \sum_{i=1}^{n} m_i \mathbf{p}_i\right) \ \forall \boldsymbol{x} \in \partial\Omega \right\}, \tag{2.29a}$$

$$\begin{aligned} a_0(v,u) = &\int_\Omega \left[\operatorname{grad}\overline{v} \cdot \operatorname{grad} u - \overline{v}\omega^2\rho\, u\right] d\Omega \\ &+ \mathrm{i}\int_\Omega \left[\operatorname{grad}\overline{v} \cdot \mu \mathbf{d}_0 u - \mathbf{d}_0\overline{v} \cdot \mu \operatorname{grad} u\right] d\Omega \\ &+ \int_\Omega \mathbf{d}_0\overline{v} \cdot \mu \mathbf{d}_0 u d\Omega, \end{aligned} \tag{2.29b}$$

$$\begin{aligned} a_1(v,u) = &\mathrm{i}\int_\Omega \left[\operatorname{grad}\overline{v} \cdot \mu \mathbf{d} u - \mathbf{d}\overline{v} \cdot \mu \operatorname{grad} u\right] d\Omega \\ &+ \int_\Omega \left[\mathbf{d}\overline{v} \cdot \mu \mathbf{d}_0 u + \mathbf{d}_0\overline{v} \cdot \mu \mathbf{d} u\right] d\Omega, \text{ and} \end{aligned} \tag{2.29c}$$

$$a_2(v,u) = \int_\Omega \mathbf{d}\overline{v} \cdot \mu \mathbf{d} u d\Omega. \tag{2.29d}$$

In the above, Ω is the domain of the unit cell and $\partial\Omega$ is its boundary. Then, the complex band structure can be obtained by solving (2.28) for different choices of direction $\mathbf{d}$ and offset $\mathbf{d}_0$ (the offset $\mathbf{d}_0$ is required for the high-symmetry line that is not connected to the center of the Brillouin zone Γ, otherwise $\mathbf{d}_0 = \mathbf{0}$). For example, for a square unit cell with a typical triangular irreducible Brillouin zone, we use $\mathbf{d} = (1, 0)$ and $\mathbf{d}_0 = \mathbf{0}$ for Γ-X; $\mathbf{d} = (1/\sqrt{2}, 1/\sqrt{2})$ and $\mathbf{d}_0 = \mathbf{0}$ for Γ-M; and $\mathbf{d} = (0, 1)$ and $\mathbf{d}_0 = (1, 0)$ for X-M.

Similarly to the one-dimensional case, we are interested in comparing the complex band structure to the one obtained by considering the sign of the problem's discriminant. The discriminant, using (2.28), is again expressed in terms of the sesquilinear forms, as:

$$\mathcal{D} = a_1(u,u)a_1(u,u) - 4a_0(u,u)a_2(u,u). \tag{2.30}$$

To highlight the equivalency between the complex band structure and the discriminant sign, we focus on a prototype square unit cell, as shown in Fig. 2.4(b). The unit cell consists of a square inclusion of dimensions (0.5×0.5) embedded concentrically within a square of unit sides. The properties of the inclusion are $\rho_1 = 1.9$, $\mu_1 = 1.7$, whereas the background medium has $\rho_2 = 0.5$ and $\mu_2 = 0.6$. The figure's gray shading is driven by the wave speeds of the two media ($c_1 = 0.95$ and $c_2 = 1.1$). Figs. 2.4(a) and 2.4(c) depict the real and imaginary part, respectively, of the complex band structure that was obtained by solving the quadratic eigenvalue problem (2.28), plotted along the high-symmetry lines of the irreducible Brillouin zone (see insert in Fig. 2.4(a)).

The shaded zones in both Figs. 2.4(a) and 2.4(c) correspond to band gaps, and are characterized by a nonzero imaginary part ($\mathrm{Im}\{\hat{k}\} \neq 0$). We note that there are multiple modes depicted in the figures. More interestingly, Fig. 2.4(d) depicts the discriminant for each of the modes shown in the complex band structure and for the same range of frequencies. We note that the regions where all modal discriminants are negative coincide with the band gaps shown in the complex band structure.

2.4.2 Lagrangian in higher dimensions

To define the Lagrangian in higher dimensions, we follow the concepts outlined in the one-dimensional formulation of section 2.3.2, while accounting for multiple directions and multiple modes. We denote the number of directions by n_d and the number of modes by n_m. Thus, we replace the one-

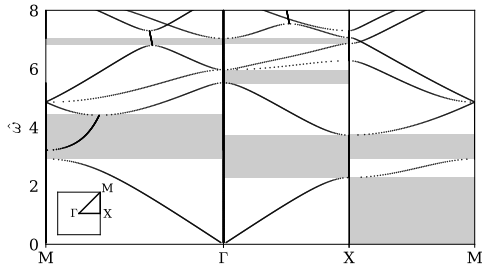

(a) Real part of the band structure, $\mathrm{Re}\{\hat{k}\}$

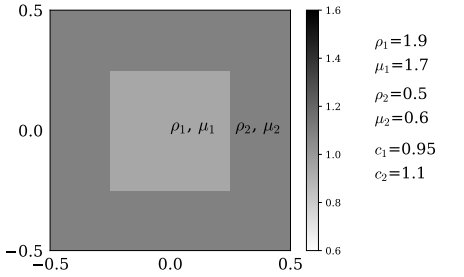

(b) Material profile (shaded by wave speed)

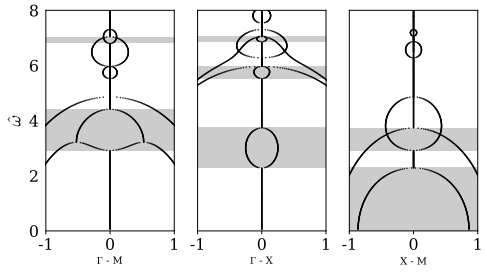

(c) Imaginary part of the band structure, $\mathrm{Im}\{\hat{k}\}$

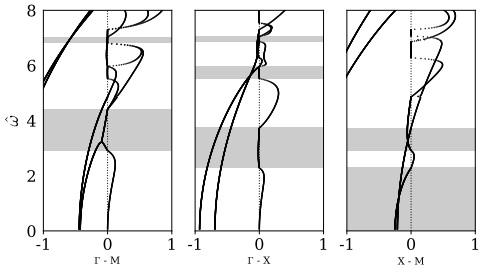

(d) Discriminant, $\mathcal{D} \times 10^3$

Figure 2.4: (a), (c): Real and imaginary parts of a typical band structure of a two-dimensional scalar wave problem; (b) unit cell topology and material properties; (d) discriminant of the associated quadratic eigenvalue problem. Multiple modes are present in each direction; band gaps are observed where all modal discriminants are negative (gaps highlighted with gray shading)

dimensional definitions (2.24) and (2.25) for the objective functional and the constraint, respectively, using conditional summations, to yield:

$$D[\rho,\mu,u] = \sum_{i}^{N}\sum_{j}^{n_d}\left[\sum_{s\,|\,\mathcal{D}_s^{(i,j)}>0}^{n_m}\mathcal{D}_s^{(i,j)}\right] \quad \text{and} \tag{2.31}$$

$$\begin{aligned} E[\rho,\mu,u,k,v,\xi] = &\sum_{i}^{N}\sum_{j}^{n_d}\left[\sum_{s\,|\,\mathcal{D}_s^{(i,j)}>0}^{n_m}\mathrm{Re}\left\{P\left(k_s^{(i,j)}\right)\left(v_s^{(i,j)},u_s^{(i,j)}\right)\right\}\right] \\ &+\sum_{i}^{N}\sum_{j}^{n_d}\left[\sum_{s\,|\,\mathcal{D}_s^{(i,j)}>0}^{n_m}\frac{\xi_s^{(i,j)}}{2}\left[a_2\left(u_s^{(i,j)},u_s^{(i,j)}\right)-1\right]\right]. \end{aligned} \tag{2.32}$$

In the above, index i is used to denote different temporal frequencies $\omega^{(i)}$ ($i = 1,\ldots,N$), index j is used to denote different directions $\mathbf{d}^{(j)}$ ($j = 1,\ldots,n_d$), and s is used to denote the s-th modal quantities (k_s, u_s of the state pair, and ξ_s, v_s of the adjoint pair), with $s = 1,\ldots,n_m$. The higher-dimensional Lagrangian is defined again as $L = D + E$.

The conditional summation in (2.31) implies, by construction, a lower bound for the objective functional D, and allows for a simple termination criterion, as discussed in section 2.3.4. We note that if a uni-directional band gap is aimed for, then $n_d = 1$, whereas for an omni-directional band gap, $n_d > 1$. In general, the minimum number for n_d depends on the topology and the sought type of band gap (uni-, multi-, or omni-directional). In our experience, driving the inversion with directions from the origin to the high-symmetry points of the Brillouin zone proved sufficient for an omni-directional band gap, without requiring multiple directions spanning the entire Brillouin zone. For example, in the case of the square unit cell, $\mathbf{d}^{(1)} = (1,0)$ (from

Γ to X) and $\mathbf{d}^{(2)} = (1/\sqrt{2}, 1/\sqrt{2})$ (from Γ to M), are sufficient for an omni-directional band gap.

2.4.3 Optimality conditions

The first-order optimality conditions are obtained similarly to the one-dimensional case, by enforcing the vanishing of the Lagrangian's first derivatives. There results:

1. **State eigenvalue problem**

   Given ρ and μ, find $k_s^{(i,j)} \in \mathbb{C}$ and $u_s^{(i,j)} \in \mathcal{W} \setminus \{0\}$ such that

$$0 = P\left(k_s^{(i,j)}\right)\left(\tilde{v}_s^{(i,j)}, u_s^{(i,j)}\right) \ \forall \tilde{v}_s^{(i,j)} \in \mathcal{W} \tag{2.33a}$$

$$0 = \frac{\tilde{\xi}_s^{(i,j)}}{2}\left[a_2\left(u_s^{(i,j)}, u_s^{(i,j)}\right) - 1\right] \ \forall \tilde{\xi}_s^{(i,j)} \in \mathbb{R}. \tag{2.33b}$$

2. **Adjoint eigenvalue problem**

   Given ρ, μ, $k_s^{(i,j)}$, and $u_s^{(i,j)}$, find $\xi_s^{(i,j)} \in \mathbb{R}$ and $v_s^{(i,j)} \in \mathcal{W}$ such that

$$\begin{aligned} 0 = {} & P\left(k_s^{(i,j)}\right)\left(v_s^{(i,j)}, \tilde{u}_s^{(i,j)}\right) + \xi_s^{(i,j)} a_2\left(u_s^{(i,j)}, \tilde{u}_s^{(i,j)}\right) \\ & + 4a_1\left(u_s^{(i,j)}, u_s^{(i,j)}\right) a_1\left(u_s^{(i,j)}, \tilde{u}_s^{(i,j)}\right) \\ & - 8a_2\left(u_s^{(i,j)}, u_s^{(i,j)}\right) a_0\left(u_s^{(i,j)}, \tilde{u}_s^{(i,j)}\right) \\ & - 8a_0\left(u_s^{(i,j)}, u_s^{(i,j)}\right) a_2\left(u_s^{(i,j)}, \tilde{u}_s^{(i,j)}\right) \ \forall \tilde{u}_s^{(i,j)} \in \mathcal{W} \end{aligned} \tag{2.34a}$$

$$0 = \tilde{k}_s^{(i,j)} a_1\left(v_s^{(i,j)}, u_s^{(i,j)}\right) + 2\tilde{k}_s^{(i,j)} k_s^{(i,j)} a_2\left(v_s^{(i,j)}, u_s^{(i,j)}\right) \ \forall \tilde{k}_s^{(i,j)} \in \mathbb{C}. \tag{2.34b}$$

3. **Gradient of L**

Given ρ, μ, $k_s^{(i,j)}$, $u_s^{(i,j)}$, $\xi_s^{(i,j)}$ and $v_s^{(i,j)}$, find $g_\rho \in \mathcal{T}$ and $g_\mu \in \mathcal{T}$ such that

$$\int_\Omega \tilde{\rho}\, g_\rho d\Omega = \sum_i^N \sum_j^{n_d} \sum_{s \mid \mathcal{D}_s^{(i,j)}>0}^{n_m} \mathrm{Re}\left\{ 4a_2\left(u_s^{(i,j)}, u_s^{(i,j)}\right) \int_\Omega \overline{u}_s^{(i,j)} \omega^2 \tilde{\rho}\, u_s^{(i,j)} d\Omega \right\}$$
$$- \sum_i^N \sum_j^{n_d} \sum_{s \mid \mathcal{D}_s^{(i,j)}>0}^{n_m} \mathrm{Re}\left\{ \int_\Omega \overline{v}_s^{(i,j)} \omega^2 \tilde{\rho}\, u_s^{(i,j)} d\Omega \right\} \quad \forall \tilde{\rho} \in \mathcal{T} \tag{2.35a}$$

$$\int_\Omega \tilde{\mu}\, g_\mu d\Omega = \sum_i^N \sum_j^{n_d} \sum_{s \mid \mathcal{D}_s^{(i,j)}>0}^{n_m} \operatorname{Re}\left\{2a_1\left(u_s^{(i,j)}, u_s^{(i,j)}\right) \int_\Omega \mathrm{i}\left(\operatorname{grad}\overline{u}_s^{(i,j)} \cdot \tilde{\mu}\, \mathbf{d}^{(j)} u_s^{(i,j)} - \mathbf{d}^{(j)}\overline{u}_s^{(i,j)} \cdot \tilde{\mu} \operatorname{grad} u_s^{(i,j)}\right) d\Omega\right\}$$

$$- \sum_i^N \sum_j^{n_d} \sum_{s \mid \mathcal{D}_s^{(i,j)}>0}^{n_m} \operatorname{Re}\left\{4a_2\left(u_s^{(i,j)}, u_s^{(i,j)}\right) \int_\Omega \operatorname{grad}\overline{u}_s^{(i,j)} \cdot \tilde{\mu} \operatorname{grad} u_s^{(i,j)} d\Omega\right\}$$

$$- \sum_i^N \sum_j^{n_d} \sum_{s \mid \mathcal{D}_s^{(i,j)}>0}^{n_m} \operatorname{Re}\left\{4a_0\left(u_s^{(i,j)}, u_s^{(i,j)}\right) \int_\Omega \overline{u}_s^{(i,j)} \tilde{\mu}\, u_s^{(i,j)} d\Omega\right\}$$

$$+ \sum_i^N \sum_j^{n_d} \sum_{s \mid \mathcal{D}_s^{(i,j)}>0}^{n_m} \operatorname{Re}\left\{k_s^{(i,j)} \int_\Omega \mathrm{i}\left(\operatorname{grad}\overline{v}_s^{(i,j)} \cdot \tilde{\mu}\, \mathbf{d}^{(j)} u_s^{(i,j)} - \mathbf{d}^{(j)}\overline{v}_s^{(i,j)} \cdot \tilde{\mu} \operatorname{grad} u_s^{(i,j)}\right) d\Omega\right\}$$

$$+ \sum_i^N \sum_j^{n_d} \sum_{s \mid \mathcal{D}_s^{(i,j)}>0}^{n_m} \operatorname{Re}\left\{\int_\Omega \operatorname{grad}\overline{v}_s^{(i,j)} \cdot \tilde{\mu} \operatorname{grad} u_s^{(i,j)} d\Omega\right\}$$

$$+ \sum_i^N \sum_j^{n_d} \sum_{s \mid \mathcal{D}_s^{(i,j)}>0}^{n_m} \operatorname{Re}\left\{\left(k_s^{(i,j)}\right)^2 \int_\Omega \overline{v}_s^{(i,j)} \tilde{\mu}\, u_s^{(i,j)} d\Omega\right\}$$

$$+ \sum_i^N \sum_j^{n_d} \sum_{s \mid \mathcal{D}_s^{(i,j)}>0}^{n_m} \operatorname{Re}\left\{\frac{\xi_s^{(i,j)}}{2} \int_\Omega \overline{u}_s^{(i,j)} \tilde{\mu}\, u_s^{(i,j)} d\Omega\right\} \quad \forall \tilde{\mu} \in \mathcal{T}, \quad (2.35b)$$

where

$$\mathcal{T} = \left\{ u \in H^0(\Omega) \middle| u(\boldsymbol{x}) = u\left(\boldsymbol{x} + \sum_{i=1}^n m_i \mathbf{p}_i\right) \ \forall \boldsymbol{x} \in \partial\Omega \right\}. \quad (2.36)$$

We note that the 1D inversion process described in section 2.3.5 remains, largely, the same.

2.5 Numerical examples

In this section, we demonstrate the performance of the band-gap-driven material inversion with numerical examples in one and two dimensions. We discuss first the one-dimensional cases.

We perform inversions with different target band-gap ranges and different unit-cell material arrangements. All inversions are performed in the frequency-domain; a time-domain simulation with the (multi-cell) metamaterial that resulted from the inversion methodology is also included to attest to the effect the metamaterial has in arresting the propagation of the targeted frequency band.

The objective functional (2.13) is capable of accommodating various material arrangements. Herein, for most of the numerical examples, we fix the topology, i.e., we constrain the number of different materials and their respective extent within the unit cell, using piecewise constant approximations for the density ρ and the modulus μ. We note that a continuously-varying or functionally-graded material can also be accommodated, as it will be shown, by simply increasing the number of allowed materials within the unit cell.

We choose the same initial guesses for ρ and μ for all one-dimensional examples, thus setting $\rho = 3000\ \mathrm{kg/m^3}$ and $\mu = 2.0\times10^{11}\ \mathrm{N/m^2}$. The length of the unit cell is set to 1 m. We use standard quadratic elements to approximate the state and adjoint eigenfunctions. Small perturbations (of unit magnitude) are added to the material properties of all elements of the mesh except for

the two out-most elements, in order not to start the inversion with a perfectly homogeneous initial guess (if the initial guess is homogeneous, the inversion will yield a constant gradient due to the periodicity). We use PETSc [5]. and SLEPc [10, 51] to implement the inversion.

2.5.1 Band-gap targets with different central frequencies

We invert first for a unit cell comprising 5 materials, and for band gaps exhibiting the same gap width (1000 Hz), but different central frequencies (5500 Hz, 6500 Hz, and 7500 Hz, respectively). Specifically, Figs. 2.5, 2.6, and 2.7 depict the results for band gaps of $5000 - 6000$ Hz, $6000 - 7000$ Hz, and $7000 - 8000$ Hz, respectively. In all three figures, the left column shows both the Brillouin zone and the discriminant as a function of frequency, while the band-gap region is shown as shaded. The right column shows the inverted material profile (density and modulus) responsible for the resulting band gap. It can be seen that in all cases the targeted band-gap regions have been sharply recovered.

2.5.2 Band-gap targets with different frequency width

We perform inversions with different target frequency widths using again 5 material elements. Figs. 2.8 and 2.9 show the results for band gaps in the $5000 - 7000$ Hz, and $5000 - 9000$ Hz range, respectively. Both the narrow (2 kHz) and the wider (4 kHz) band gaps are well delineated, as shown with the shaded regions. Notice that in the first case (Fig. 2.8), the first gap that

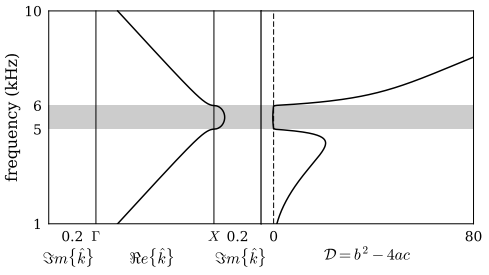

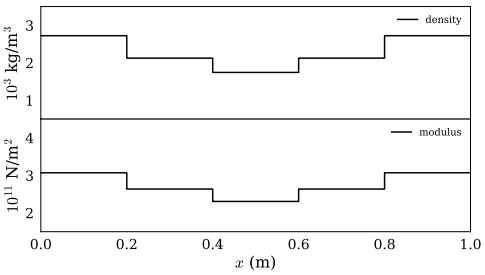

(a) Band structure (left) and discriminant (right)

(b) Unit-cell density and modulus distribution

Figure 2.5: Inversion for 5 material elements with a target band gap of $5 - 6$ kHz

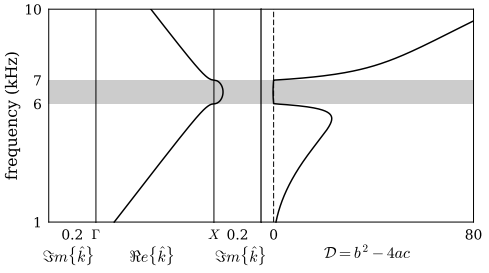

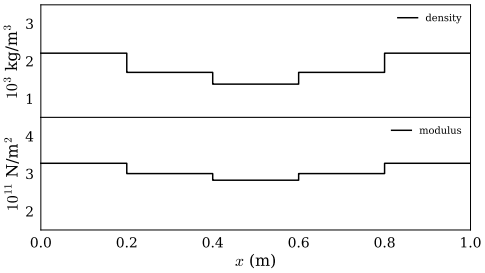

(a) Band structure (left) and discriminant (right)

(b) Unit-cell density and modulus distribution

Figure 2.6: Inversion for 5 material elements with a target band gap of $6 - 7$ kHz

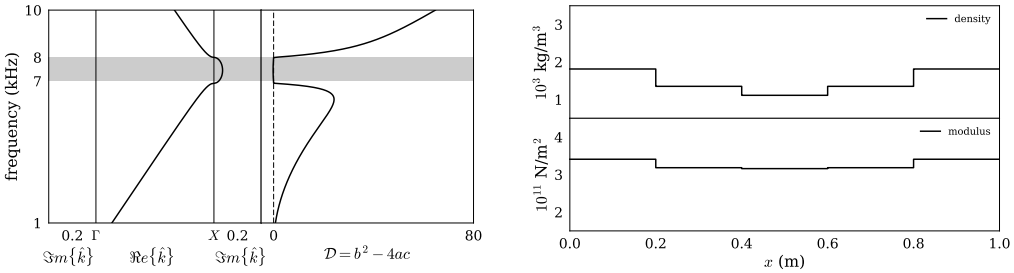

(a) Band structure (left) and discriminant (right)

(b) Unit-cell density and modulus distribution

Figure 2.7: Inversion for 5 material elements with a target band gap of $7 - 8$ kHz

appears in the band structure is the target band gap; however, in the second case (Fig. 2.9), the inversion led to a unit cell that exhibits a first gap at lower frequencies (around 3 kHz) than the target gap, in addition to the target band gap (5-9 kHz).

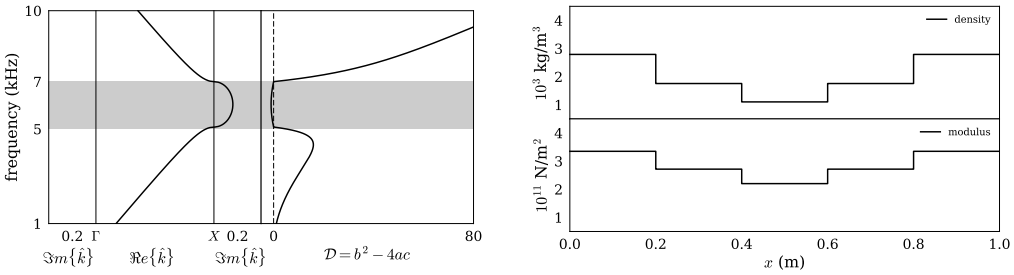

(a) Band structure (left) and discriminant (right)

(b) Unit-cell density and modulus distribution

Figure 2.8: Inversion for 5 material elements with a target band gap of $5 - 7$ kHz

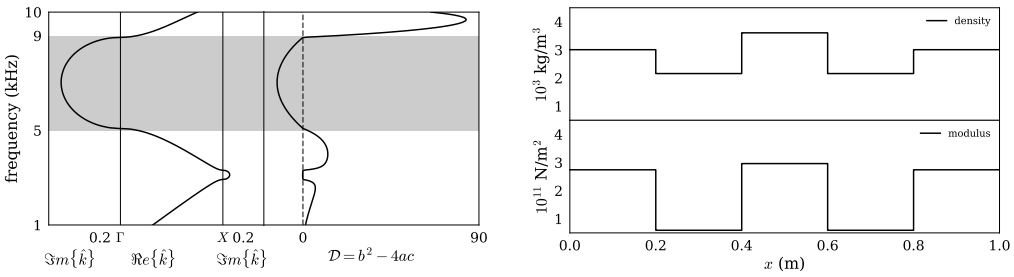

(a) Band structure (left) and discriminant (right)

(b) Unit-cell density and modulus distribution

Figure 2.9: Inversion for 5 material elements with a target band gap of $5 - 9$ kHz

2.5.3 Band-gap targets with different number of unit-cell material elements

Next, we relax the 5-material constraint for the unit cell to allow for 40 different piecewise-constant materials of equal thickness, thus approximating a materially continuously-varying unit cell. The desired band gap is set to $5000 - 6000$ Hz. Fig. 2.10 depicts the resulting density and modulus unit-cell distributions, alongside with the band-gap structure. Moreover, Fig. 2.11 shows the resulting material distribution when the material constraint for the unit cell has been reinstated and set to 3. We note that the band-gap structures are identical between the two cases: this is evidence of multiplicity, i.e., different unit-cell material arrangements are capable of exhibiting the same band-gap. In practice, manufacturing constraints on the number and/or the type of materials could drive the inversion for a fixed topology.

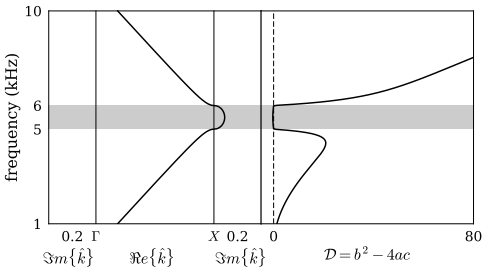

(a) Band structure (left) and discriminant (right)

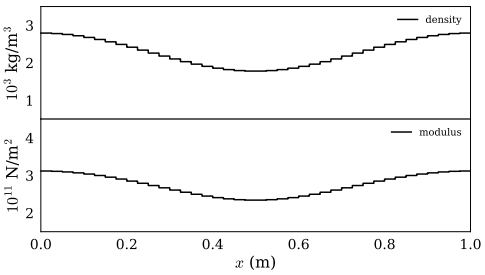

(b) Unit-cell density and modulus distribution

Figure 2.10: Inversion for 40 material elements with a target band gap of $5-6$ kHz

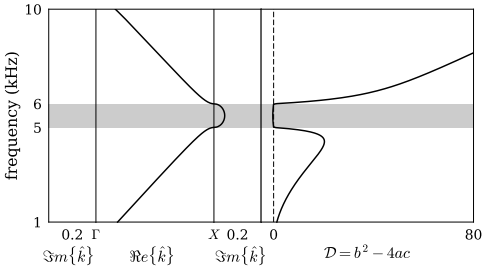

(a) Band structure (left) and discriminant (right)

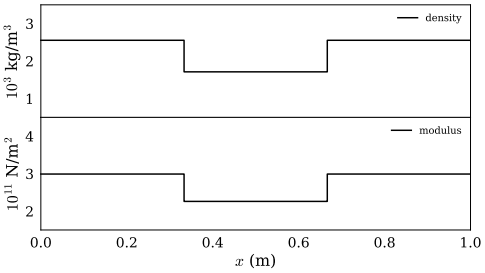

(b) Unit-cell density and modulus distribution

Figure 2.11: Inversion for 3 material elements with a target band gap of $5-6$ kHz

2.5.4 Metamaterial time-domain simulations

Next, we use the inverted 5-material unit cell design depicted in Fig. 2.8(b) to construct a metamaterial by stacking 8 unit cells (8m-long) together, within a 10m-long domain (Fig. 2.12). We subject the metamaterial block to a dichromatic sinusoidal load given by:

$$f(t) = \sin(2\pi f_1 t) + \sin(2\pi f_2 t), \tag{2.37}$$

where $f_1 = 6000$Hz and $f_2 = 2000$Hz. Near the origin and to the left of the applied source (source at $x = 0.067$m) and at $x = 10$m we apply absorbing boundary conditions (Fig. 2.12). The selected unit cell exhibits, by virtue of

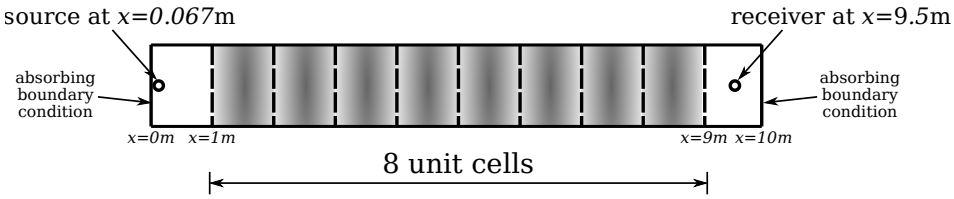

Figure 2.12: Metamaterial time-domain simulation schematic

the inverse design, a band gap between $5000 - 7000$Hz. Thus, the propagation of f_1 should be arrested, and the resulting signal should be monochromatic at the f_2 frequency. Fig. 2.13 depicts the time-domain results. The first-row figures (Fig. 2.13(a) and 2.13(b)) depict the response of a homogeneous medium. By comparing the signal at the entry point ($x = 0$m) with the signal at the domain end ($x = 10$m) in the waterfall plot, it can be seen that the dichromatic signal's frequency content remains intact during the propagation. By contrast, the waterfall plot in Fig. 2.13(c), which corresponds to

the metamaterial, shows that the entering dichromatic signal was reduced to a monochromatic signal at exit, with only the f_2 frequency component surviving, as intended. To illustrate the effect with broader-band driving signals, we

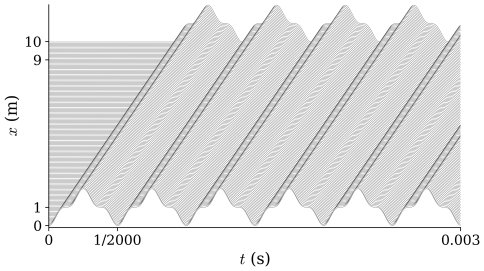

(a) Waterfall plot of the homogeneous case

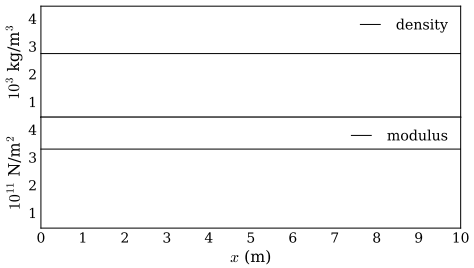

(b) Material profiles of the homogeneous case

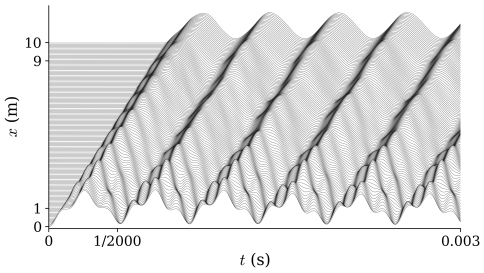

(c) Waterfall plot of the metamaterial case

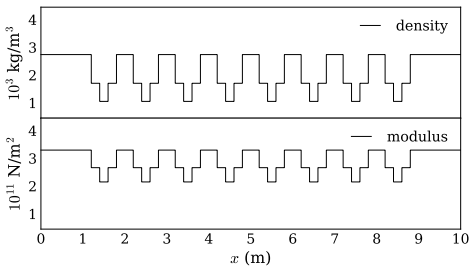

(d) Material profiles of the metamaterial case

Figure 2.13: Time-domain simulation of a metamaterial block subjected to a dichromatic load: (a) dichromatic signal with $f_1 = 2000$Hz and $f_2 = 6000$Hz propagates within the homogeneous medium without frequency component loss; (c) dichromatic signal is reduced to a monochromatic signal when propagating through the metamaterial block ($f_2 = 6000$Hz is arrested).

next subject the same metamaterial structure to a Ricker pulse with a central frequency at 10kHz. The Ricker pulse is defined as:

$$f(t) = \frac{(0.25u^2 - 0.5)e^{-0.25u^2} - 13e^{-13.5}}{0.5 + 13e^{-13.5}},\ 0 \leq t \leq \frac{6\sqrt{6}}{\omega_r}, \tag{2.38}$$

where $u = \omega_r t - 3\sqrt{6}$ and $\omega_r = 2\pi \cdot 10000$ is the central circular frequency. The response is again recorded at $x = 10$m and its discrete Fourier Transform is shown in Fig. 2.14 together with the band structure. The dashed line represents the DFT of the homogeneous material response, whereas the solid line represents the DFT of the metamaterial response. We note that the band gap between $5 - 7$kHz worked well by forcing the response to near silence. Notice that the metamaterial exhibits a second band gap between $11.8 - 12.4$kHz, which also had an amplitude-reducing effect on the response.

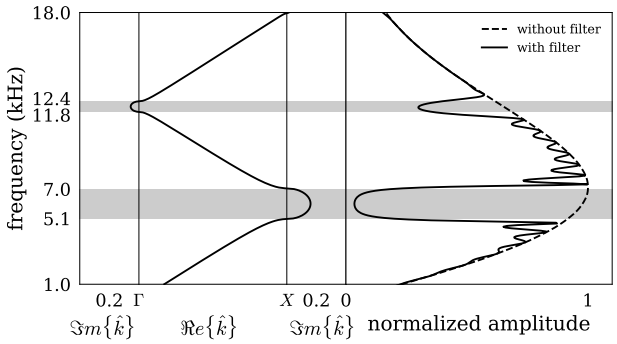

Figure 2.14: DFT response of a homogeneous material and metamaterial subjected to a Ricker pulse: waves are attenuated at the band-gap regions (highlighted with shades).

Asymmetric material profiles The preceding examples have all resulted in symmetric material profiles. This is due to the fact that the initial guesses were symmetric. Using asymmetric distributions as initial guesses, one can obtain asymmetric material profiles through inversion. To illustrate, we start with an initial guess with the same amount of perturbation on the properties

as the one we used for all the preceding examples. However, in this case we perturb only the properties of the second element to force an asymmetric initial guess. The results are depicted in Fig. 2.15). The target band-gap region is identical to the one we obtained previously (Fig. 2.5), yet the recovered unit-cell is asymmetric.

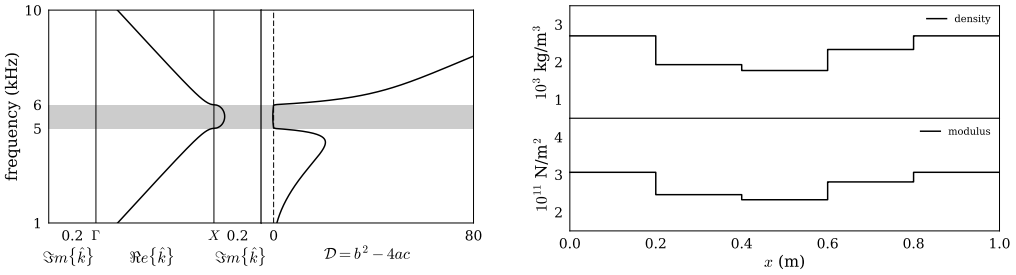

(a) Band structure (left) and discriminant (right)

(b) Unit-cell density and modulus distribution

Figure 2.15: Inversion for 5 material elements with a target frequency range of $5-6$ kHz: asymmetric material properties are obtained by asymmetric initial guesses.

2.5.5 Omni-directional band gap design in 2D

We discuss the application of the inversion methodology to two dimensions. Our reference unit cell is a square with sides p, with a concentrically embedded square inclusion with sides equal to $0.5p$. Under this fixed topology, we seek to invert for the material properties of both the inclusion (ρ_1 and μ_1) and of the background square host (ρ_2 and μ_2). The primitive lattice vectors are $\mathbf{p}_1 = (1, 0)$ and $\mathbf{p}_2 = (0, 1)$, where $\|\mathbf{p}_1\| = \|\mathbf{p}_2\| = 1 \equiv p$. We are interested in an omni-directional band gap, and to this end, we use two directions

($n_d = 2$), $\mathbf{d}^{(1)} = (1, 0)$ (Γ to X), and $\mathbf{d}^{(2)} = (1/\sqrt{2}, 1/\sqrt{2})$ (Γ to M). We set the number of modes to $n_m = 4$, and the number of frequencies in the target band gap to $N = 30$. We discuss three examples with different target band gaps: $3 - 4$, $4 - 5$, and $4 - 6$ rad/s.

We start with the initial material profile of $\rho_1 = 1.1$, $\mu_1 = 1.1$, $\rho_2 = 1.0$, and $\mu_2 = 1.0$ for all three examples. The band structure of the initial guess is shown in Fig. 2.16: it is very similar to that of a homogeneous medium, exhibiting, however, narrow directional band gaps and degeneracy breakings.

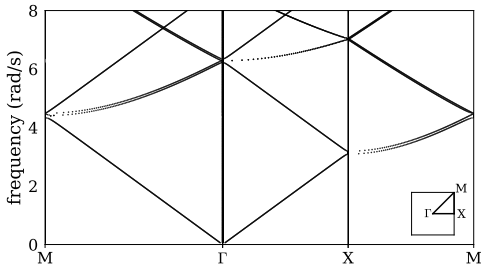

(a) Real part of the band structure, Re$\{\hat{k}\}$

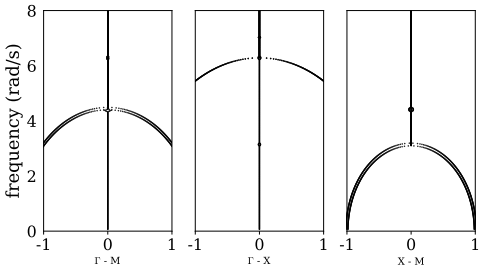

(b) Imaginary part of the band structure, Im$\{\hat{k}\}$

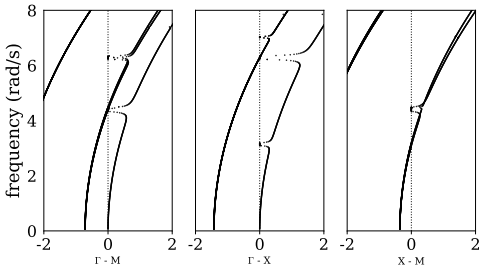

(c) Discriminant, $\mathcal{D} \times 10^3$

Figure 2.16: Complex band structure and discriminant of the initial guess

Figs. 2.17, 2.18, and 2.19 show the results of the inverse designs for

the different target band gaps, $3-4$, $4-5$, and $4-6$ rad/s, respectively. In each figure, subplots (a) show the trajectory of the objective functional as the number of iterations increases (semi-log plot): there is, roughly, a four-order reduction from the initial guess. Subplots (b) show the converged material profile, i.e., the inverted-for material parameters ρ_1, μ_1, ρ_2, and μ_2 (the shading is driven by the wave speeds). Subplots (c) show the real part, while subplots (d) show the imaginary part of the band structure of the designed unit cell. Subplots (e) show the associated discriminant. As it can be seen, in all cases, the targeted omni-directional band gaps (shown in subplots (c), (d), and (e) with shaded strips) have been realized.

We note that, in all cases, an, unduly, small search length was used (10^{-7}), resulting in a moderate number of iterations. For the examples reported herein, the search length can be reduced significantly (2 orders of magnitude) without affecting the quality of the converged profiles. The number of iterations can be further reduced by increasing the sampling frequency points in the target band gap.

2.6 Conclusions

We discussed an approach for the inverse design of metamaterials, driven by a user-defined band gap. To this end, we showed that the sign of the discriminant of the associated quadratic eigenvalue problem serves as a sharp indicator of propagating and evanescent states. Then, we formulated an inverse medium problem using the discriminant as the driving objective

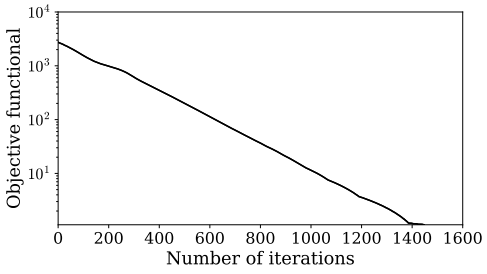

(a) Objective functional

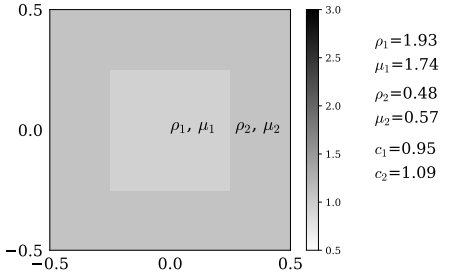

(b) Material profile (shaded by wave speed)

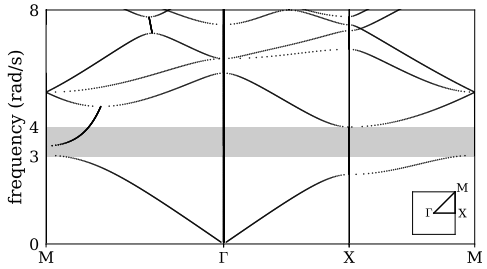

(c) Real part of the band structure, $\mathrm{Re}\{\hat{k}\}$

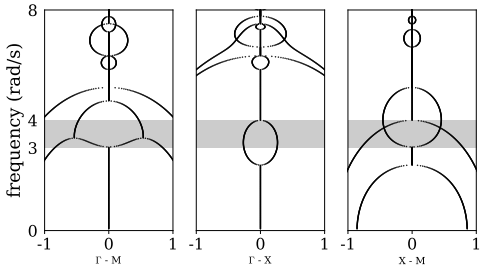

(d) Imaginary part of the band structure, $\mathrm{Im}\{\hat{k}\}$

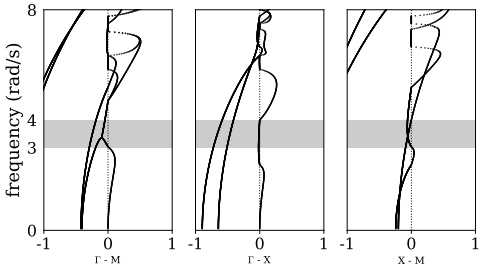

(e) Discriminant, $\mathcal{D} \times 10^3$

Figure 2.17: Inversion for 2 materials elements for an omni-directional band gap at $3 - 4$ rad/s; band gap shown shaded

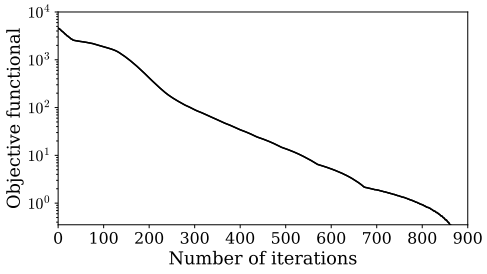

(a) Objective functional

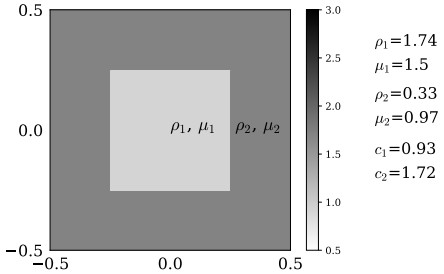

(b) Material profile (shaded wave speed)

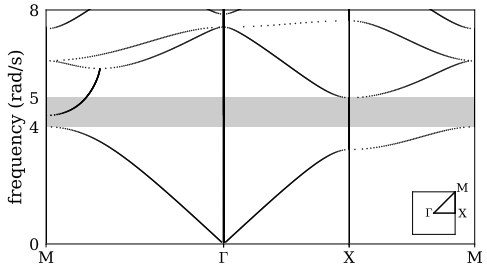

(c) Real part of the band structure, $\mathrm{Re}\{\hat{k}\}$

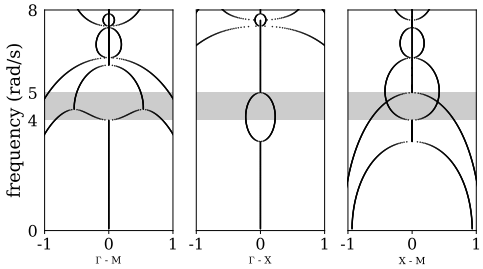

(d) Imaginary part of the band structure, $\mathrm{Im}\{\hat{k}\}$

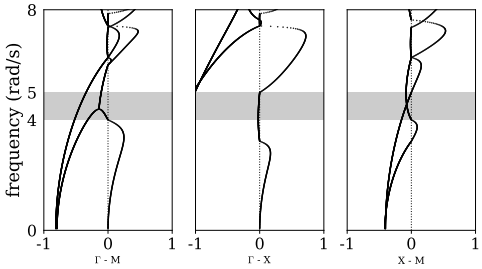

(e) Discriminant, $\mathcal{D} \times 10^3$

Figure 2.18: Inversion for 2 materials elements for an omni-directional band gap at $4 - 5$ rad/s; band gap shown shaded

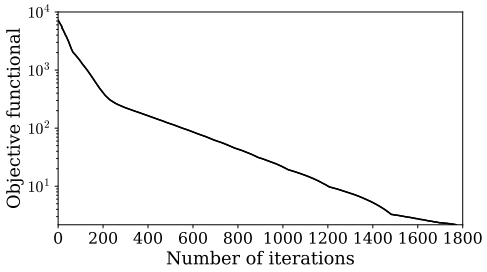

(a) Objective functional

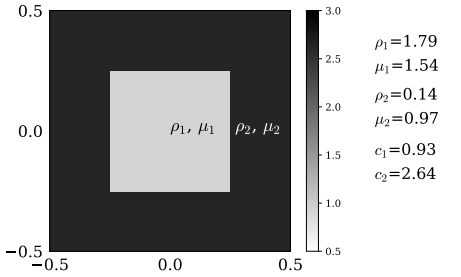

(b) Material profile (shaded wave speed)

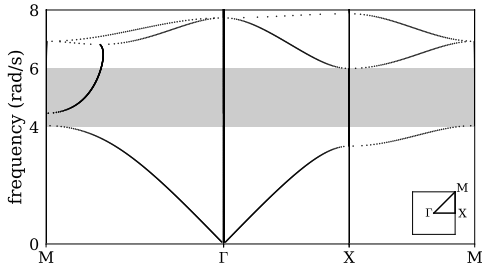

(c) Real part of the band structure, $\mathrm{Re}\{\hat{k}\}$

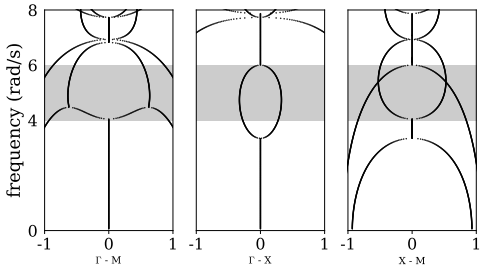

(d) Imaginary part of the band structure, $\mathrm{Im}\{\hat{k}\}$

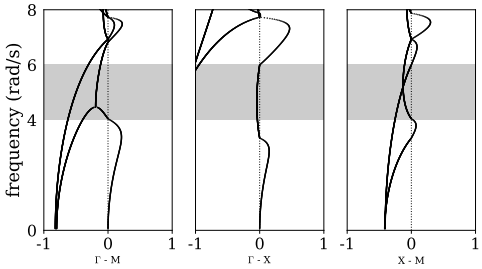

(e) Discriminant, $\mathcal{D} \times 10^3$

Figure 2.19: Inversion for 2 materials elements for an omni-directional band gap at $4 - 6$ rad/s; band gap shown shaded

functional, and the associated eigenvalue problem as a side constraint. We demonstrated the performance of the inversion method with various numerical examples in one and two dimensions using scalar waves.

In summary, we conclude:

- The discriminant uniquely identifies propagating and evanescent states, and, thus, forms an ideal basis for band-gap design;
- The proposed discriminant-based objective functional does not require prior knowledge of the exact band structure;
- The proposed discriminant-based objective functional is differentiable, which is necessary for gradient-based optimization algorithms;
- The inversion process is capable of designing band-gap materials with various target band gaps; and
- The inverted band-gap materials can be used in metamaterials to attenuate incoming waves at the band-gap frequencies.

2.7 Acknowledgment

Partial support for the first author was provided by a University of Texas at Austin VPR Research Grant; the support is gratefully acknowledged. We also wish to thank the anonymous reviewers and the editors for their constructive comments.

2.8 Appendix: Gâteaux derivatives of L

The 1st-order Gâteaux derivative with respect to u of F, or $\delta_u F[u](\tilde{u})$, is defined as

$$\delta_u F[u](\tilde{u}) = \left.\frac{d}{d\varepsilon}\right|_{\varepsilon=0} F[u + \varepsilon\tilde{u}], \tag{2.39}$$

where $\tilde{u}$ is the direction of the Gâteaux derivative. The Fréchet derivative g_u is defined as [57]

$$\int_\Omega \tilde{u} g_u d\Omega = \delta_u F[u](\tilde{u}). \tag{2.40}$$

The (Gâteaux) derivatives of the Lagrangian L are given below; to reduce the notational congestion, we replace $[\rho, \mu, u, k, v, \xi]$ with $[\ldots]$.

The derivatives with respect to the adjoint variables are:

$$\delta_{v_0^{(i)}} L[\ldots]\left(\tilde{v}_0^{(i)}\right) = \mathrm{Re}\left\{P\left(k_0^{(i)}\right)\left(\tilde{v}_0^{(i)}, u_0^{(i)}\right)\right\} \text{ and} \tag{2.41}$$

$$\begin{aligned}\delta_{\xi_0^{(i)}} L[\ldots]\left(\tilde{\xi}_0^{(i)}\right) &= \frac{\tilde{\xi}_0^{(i)}}{2}\left[a_2\left(u_0^{(i)}, u_0^{(i)}\right) - 1\right] \\ &= \mathrm{Re}\left\{\frac{\tilde{\xi}_0^{(i)}}{2}\left[a_2\left(u_0^{(i)}, u_0^{(i)}\right) - 1\right]\right\}.\end{aligned} \tag{2.42}$$

The derivatives with respect to the state variables are:

$$\delta_{u_0^{(i)}} L[\ldots]\left(\tilde{u}_0^{(i)}\right) = \delta_{u_0^{(i)}} D[\ldots]\left(\tilde{u}_0^{(i)}\right) + \delta_{u_0^{(i)}} E[\ldots]\left(\tilde{u}_0^{(i)}\right) \text{ and} \tag{2.43}$$

$$\delta_{k_0^{(i)}} L[\ldots]\left(\tilde{k}_0^{(i)}\right) = \delta_{k_0^{(i)}} D[\ldots]\left(\tilde{k}_0^{(i)}\right) + \delta_{k_0^{(i)}} E[\ldots]\left(\tilde{k}_0^{(i)}\right), \tag{2.44}$$

where

$$\begin{aligned}
\delta_{u_0^{(i)}} D\left[\ldots\right]\left(\tilde{u}_0^{(i)}\right) &= 4a_1\left(u_0^{(i)}, u_0^{(i)}\right) \mathrm{Re}\left\{a_1\left(u_0^{(i)}, \tilde{u}_0^{(i)}\right)\right\} \\
&\quad - 8a_2\left(u_0^{(i)}, u_0^{(i)}\right) \mathrm{Re}\left\{a_0\left(u_0^{(i)}, \tilde{u}_0^{(i)}\right)\right\} \\
&\quad - 8a_0\left(u_0^{(i)}, u_0^{(i)}\right) \mathrm{Re}\left\{a_2\left(u_0^{(i)}, \tilde{u}_0^{(i)}\right)\right\} \\
&= \mathrm{Re}\left\{4a_1\left(u_0^{(i)}, u_0^{(i)}\right) a_1\left(u_0^{(i)}, \tilde{u}_0^{(i)}\right)\right\} \\
&\quad - \mathrm{Re}\left\{8a_2\left(u_0^{(i)}, u_0^{(i)}\right) a_0\left(u_0^{(i)}, \tilde{u}_0^{(i)}\right)\right\} \\
&\quad - \mathrm{Re}\left\{8a_0\left(u_0^{(i)}, u_0^{(i)}\right) a_2\left(u_0^{(i)}, \tilde{u}_0^{(i)}\right)\right\}, \qquad (2.45) \\
\delta_{u_0^{(i)}} E\left[\ldots\right]\left(\tilde{u}_0^{(i)}\right) &= \mathrm{Re}\left\{P\left(k_0^{(i)}\right)\left(v_0^{(i)}, \tilde{u}_0^{(i)}\right)\right\} \\
&\quad + \mathrm{Re}\left\{\xi_0^{(i)} a_2\left(u_0^{(i)}, \tilde{u}_0^{(i)}\right)\right\}, \qquad (2.46) \\
\delta_{k_0^{(i)}} D\left[\ldots\right]\left(\tilde{k}_0^{(i)}\right) &= 0, \text{ and} \qquad (2.47) \\
\delta_{k_0^{(i)}} E\left[\ldots\right]\left(\tilde{k}_0^{(i)}\right) &= \mathrm{Re}\left\{\tilde{k}_0^{(i)} a_1\left(v_0^{(i)}, u_0^{(i)}\right) + 2k_0^{(i)}\tilde{k}_0^{(i)} a_2\left(v_0^{(i)}, u_0^{(i)}\right)\right\}. \qquad (2.48)
\end{aligned}$$

The derivatives with respect to the design variables (ρ and μ) are:

$$\begin{aligned}
\delta_\rho L\left[\ldots\right](\tilde{\rho}) &= \delta_\rho D\left[\ldots\right](\tilde{\rho}) + \delta_\rho E\left[\ldots\right](\tilde{\rho}) \text{ and} \qquad (2.49) \\
\delta_\mu L\left[\ldots\right](\tilde{\mu}) &= \delta_\mu D\left[\ldots\right](\tilde{\mu}) + \delta_\mu E\left[\ldots\right](\tilde{\mu}), \qquad (2.50)
\end{aligned}$$

where

$$\begin{aligned}
\delta_\rho D[\ldots](\tilde{\rho}) &= -\sum_i^N 4a_2\left(u_0^{(i)}, u_0^{(i)}\right) \delta_\rho a_0\left(u_0^{(i)}, u_0^{(i)}\right) \\
&= \sum_i^N \mathrm{Re}\left\{4a_2\left(u_0^{(i)}, u_0^{(i)}\right) \int_0^p \overline{u}^{(i)} \omega^2 \tilde{\rho}\, u_0^{(i)} dx\right\}, \qquad (2.51)
\end{aligned}$$

$$\delta_\rho E[\ldots](\tilde{\rho}) = \sum_i^N \delta_\rho \mathrm{Re}\left\{a_0\left(v_0^{(i)}, u_0^{(i)}\right)\right\}$$
$$= -\sum_i^N \mathrm{Re}\left\{\int_0^p \overline{v}^{(i)}\omega^2\tilde{\rho}\, u_0^{(i)} dx\right\}, \tag{2.52}$$

$$\delta_\mu D[\ldots](\tilde{\mu}) = \sum_i^N 2a_1\left(u_0^{(i)}, u_0^{(i)}\right)\ \delta_\mu a_1\left(u_0^{(i)}, u_0^{(i)}\right)$$
$$- \sum_i^N 4a_2\left(u_0^{(i)}, u_0^{(i)}\right)\ \delta_\mu a_0\left(u_0^{(i)}, u_0^{(i)}\right)$$
$$- \sum_i^N 4a_0\left(u_0^{(i)}, u_0^{(i)}\right)\ \delta_\mu a_2\left(u_0^{(i)}, u_0^{(i)}\right)$$
$$= \sum_i^N \mathrm{Re}\left\{2a_1\left(u_0^{(i)}, u_0^{(i)}\right)\int_0^p \mathrm{i}\left(\frac{\partial\overline{u}^{(i)}}{\partial x}\tilde{\mu}\, u_0^{(i)} - \overline{u}^{(i)}\tilde{\mu}\frac{\partial u_0^{(i)}}{\partial x}\right)dx\right\}$$
$$- \sum_i^N \mathrm{Re}\left\{4a_2\left(u_0^{(i)}, u_0^{(i)}\right)\int_0^p \frac{\partial\overline{u}^{(i)}}{\partial x}\tilde{\mu}\frac{\partial u_0^{(i)}}{\partial x}dx\right\}$$
$$- \sum_i^N \mathrm{Re}\left\{4a_0\left(u_0^{(i)}, u_0^{(i)}\right)\int_0^p \overline{u}^{(i)}\tilde{\mu}\, u_0^{(i)} dx\right\}, \text{ and} \tag{2.53}$$

$$\delta_\mu E[\ldots](\tilde{\mu}) = \sum_i^N \delta_\mu \mathrm{Re}\left\{P\left(k_0^{(i)}\right)\left(v_0^{(i)}, u_0^{(i)}\right)\right\} + \sum_i^N \frac{\xi_0^{(i)}}{2}\delta_\mu a_2\left(u_0^{(i)}, u_0^{(i)}\right)$$
$$= \sum_i^N \mathrm{Re}\left\{k_0^{(i)}\int_0^p \mathrm{i}\left(\frac{\partial\overline{v}^{(i)}}{\partial x}\tilde{\mu}\, u_0^{(i)} - \overline{v}^{(i)}\tilde{\mu}\,\frac{\partial u_0^{(i)}}{\partial x}\right)dx\right\}$$
$$+ \sum_i^N \mathrm{Re}\left\{\int_0^p \frac{\partial\overline{v}^{(i)}}{\partial x}\tilde{\mu}\frac{\partial u_0^{(i)}}{\partial x}dx\right\}$$
$$+ \sum_i^N \mathrm{Re}\left\{\left(k_0^{(i)}\right)^2\int_0^p \overline{v}^{(i)}\tilde{\mu}\, u_0^{(i)} dx\right\}$$
$$+ \sum_i^N \mathrm{Re}\left\{\frac{\xi_0^{(i)}}{2}\int_0^p \overline{u}^{(i)}\tilde{\mu}\, u_0^{(i)} dx\right\}. \tag{2.54}$$

Chapter 3

Group velocity-driven inverse metamaterial design[1]

We are concerned with controlling wave propagation in elastic media by engineering their dispersive properties. To this end, we discuss a flexible and systematic framework for designing the material composition of the unit cell of a periodic medium when given a target dispersion relation or, equivalently, a target group velocity profile at a user-defined frequency range. We cast the inverse medium design problem as a dispersion-constrained optimization problem that minimizes the distance between the target and the computed group velocity profiles. We rely on the Hellmann-Feynman theorem to obtain the computed group velocity of a trial unit cell, and use a gradient-based algorithm to drive the engineered medium's material properties to convergence. We demonstrate numerically the capabilities of the approach using scalar waves in one and two dimensions. We also use the method to design metamaterials exhibiting user-defined omni-directional band gaps, and provide numerical

[1]This chapter has been published in: Heedong Goh and Loukas F. Kallivokas, Group velocity-driven inverse metamaterial design, *Journal of Engineering Mechanics*, 145(12):04019094, 2019. The dissertation author had significant contributions to the article that included the development of the methodology, its implementation, the numerical results, and the related discussion.

evidence of the metamaterial's intended performance via time-domain simulations.

3.1 Introduction

The interest in understanding and modeling wave propagation in periodic structures is centuries old, originating possibly with the modeling of spring-mass chains; important contributions can be found in the seminal works of Newton [42], Rayleigh [50], and Brillouin [8]. Recent renewed attention to waves in periodic structures is due to the ability to design and manufacture periodic media at various length scales that exhibit unconventional properties [41], which, in turn, can be harnessed to advantage. Whereas the periodic structure's unit cell constituent materials have conventional properties (e.g., positive mass density and positive elastic modulus) the composite periodic structure's homogenized properties may exhibit singly-negative, or doubly-negative material properties, thus endowing the structure with metamaterial status.

The exotic or unconventional properties of metamaterials are exploited to drive novel applications in solid state physics, in photonics, and in phononics; related contributions of note include the works of [35, 45] in subwavelength focusing, and of [3, 9, 43, 55] in invisibility cloaking. The aforementioned, as well as similar developments in optics have fueled interest in extending the gains realized therein to the case of media supporting elastic waves, most notably for seismic shielding applications [2, 15, 30, 37, 38, 44], despite the dif-

ficulties imposed by the presence of two different bulk wave types and large wavelengths.

Whether in optics or elastodynamics, key interests include the design of metamaterials capable of steering or channeling waves, band-gaping, filtering, focusing, etc [13, 14, 16, 17, 20, 26, 59]. Irrespective of the application field, to date, metamaterial design is done on an *ad hoc* basis, driven mostly by physical insight: no systematic process has been proposed to guide either the topological or material inverse problems associated with the design of a metamaterial when given a target outcome. Examples of a few exceptions include band-gap maximization [48, 56], wave amplitude control [7, 52], design for effective medium properties [62], a topological optimization for optical waveguides [11], optimal design of seismic metamaterials [61], and the systematic approach for metamaterial band gap design in [23].

Specifically, in [23], we proposed a method for designing a metamaterial exhibiting a user-defined band gap, using the discriminant of the associated quadratic eigenvalue problem as the inverse medium problem driver. Though systematic, the approach is limited to band gaps: broader design considerations, including wave directivity control, spectrum-specific wave speed control, multiple target band gaps, etc, can only be accommodated if the design approach considers the dispersive behavior in a holistic manner. Thus, to design the topology or the material properties of a metamaterial in order for it to exhibit a user-prescribed behavior, requires engineering the metamaterial's dispersive characteristics, or, equivalently, its dispersion curve(s)/surface(s).

A suitable metric –perhaps the most suitable– for engineering the dispersion curve is its "derivative," i.e., the group velocity, for it readily allows for the simultaneous consideration of several of the aforementioned design targets.

It is noted that engineering the dispersion curve(s), or equivalently the group velocity profile, is a *bona fide* inverse medium problem. In this article, we describe a systematic method for designing a metamaterial unit cell to exhibit a user-defined group velocity profile. The associated inverse medium problem borrows from the systematic framework used in related work in inverse medium geoscience problems [18, 28, 31, 36].

The structure of the article is as follows: we briefly review the dispersive characteristics of a periodic medium and discuss the complex band structure, band gaps, and group velocity. Then, we define the metamaterial unit cell design problem driven by a target group velocity profile, and describe the resolution of the associated inverse medium problem. Numerical examples resulting in the design of one- and two-dimensional unit cells are provided to demonstrate the method's capabilities in the frequency domain, including the design of a unit cell exhibiting an omni-directional user-defined band gap. Lastly, we reinforce the findings via time-domain simulations, with limited-width metamaterial blocks that show subwavelength performance.

3.2 Preliminaries

We are interested in controlling a medium's dispersive properties. To fix ideas, we use a target group velocity profile to drive the inverse metamaterial

design problem. Band gaps and other similar design goals emerge as particular cases of the group velocity design problem. To describe the approach, we appeal first to the properties of the eigenvalue problem of a periodic medium.

3.2.1 The periodic medium and its complex dispersion relation

A periodic medium is characterized by a dispersion relation exhibiting band gaps, backward propagating waves, slow and fast waves, mode conversions, etc. To arrive at the dispersion relation of a periodic medium, we begin with a quadratic eigenvalue problem. To this end, consider the scalar Helmholtz equation in N_{d}-dimensional space, i.e.,

$$0 = \operatorname{div}\left[\mu\left(\boldsymbol{x}\right)\operatorname{grad} U\left(\boldsymbol{x}\right)\right] + \rho\left(\boldsymbol{x}\right)\omega^2 U\left(\boldsymbol{x}\right), \quad \boldsymbol{x} \in \mathbb{R}^{N_{\mathrm{d}}}, \tag{3.1}$$

where, for a scalar elastodynamic problem, $U\left(\boldsymbol{x}\right)$ is the displacement, $\mu\left(\boldsymbol{x}\right)$ is shear modulus, $\rho\left(\boldsymbol{x}\right)$ is density, and ω denotes the temporal frequency. For a periodic medium, the spatial distribution of the material properties satisfy

$$\rho\left(\boldsymbol{x}\right) = \rho\left(\boldsymbol{x} + \sum_{i=1}^{N_{\mathrm{d}}} m_i \mathbf{p}_i\right) \quad \text{and} \tag{3.2a}$$

$$\mu\left(\boldsymbol{x}\right) = \mu\left(\boldsymbol{x} + \sum_{i=1}^{N_{\mathrm{d}}} m_i \mathbf{p}_i\right) \quad \forall \boldsymbol{x} \in \mathbb{R}^{N_{\mathrm{d}}},\ \forall m_i \in \mathbb{Z}. \tag{3.2b}$$

Each primitive vector $\mathbf{p}_i \in \mathbb{R}^{N_{\mathrm{d}}}$ defines the periodicity in the i-th direction, and m_i is an arbitrary integer. For example, a choice of $\mathbf{p}_1 = (1, 0)$ and $\mathbf{p}_2 = (0, 1)$ defines a square periodic unit cell in a two dimensional plane. Then, the *Bloch theorem* [4] provides the general solution of equation (3.1)

under the periodicity relations (3.2), as

$$U(\boldsymbol{x}) = e^{\mathrm{i}\mathbf{k}\cdot\boldsymbol{x}} u(\boldsymbol{x}), \tag{3.3}$$

where the displacement-like quantity $u(\boldsymbol{x})$ is also periodic with the same periodicity $\mathbf{p}_i$ of the medium, and $\mathbf{k}$ is the Bloch wavevector. Thus, the general solution $U(\boldsymbol{x})$ consists of a plane wave $e^{\mathrm{i}\mathbf{k}\cdot\boldsymbol{x}}$ enveloped by the periodic function $u(\boldsymbol{x})$. The Bloch theorem allows us to obtain an eigenvalue problem defined over a unit cell Ω_{cell} by substituting the general solution (3.3) into the Helmholtz equation (3.1). Then, in weak form, the eigenvalue problem can be cast as [6]

$$0 = \int_{\Omega_{\text{cell}}} \left[(-\mathrm{i}k\mathbf{d}\overline{v} + \operatorname{grad}\overline{v}) \cdot \mu \, (\mathrm{i}k\mathbf{d}u + \operatorname{grad} u) - \overline{v}\rho\,\omega^2 u \right] d\Omega. \tag{3.4}$$

In equation (3.4), $k = \mathbf{k}\cdot\mathbf{d}$ is the wavevector in any direction of interest $\mathbf{d}$, v is a test function, and an overline $\overline{(\,)}$ denotes complex conjugation of the subtended quantity. For a given real-valued ω, the eigenvalue problem (3.4) can be solved for a complex-valued k. Specifically, we rearrange the weak form (3.4) to obtain the following quadratic eigenvalue problem:
Given $\omega \in \mathbb{R}$ and $\mathbf{d} \in \mathbb{R}^{N_{\text{d}}}$, find $k \in \mathbb{C}$ and $u \in \mathcal{V} \setminus \{0\}$ such that

$$0 = a_0(v,u) + k a_1(v,u) + k^2 a_2(v,u) \equiv P(k)(u,v) \qquad \forall v \in \mathcal{V}, \tag{3.5}$$

where

$$\mathcal{V} = \left\{ u \in H^1(\Omega_{\text{cell}}) \middle| u(\boldsymbol{x}) = u\left(\boldsymbol{x} + \sum_{i=1}^{N_{\text{d}}} m_i \mathbf{p}_i \right) \ \forall \boldsymbol{x} \in \partial\Omega_{\text{cell}} \right\}, \quad (3.6a)$$

$$a_0(v,u) = \int_{\Omega_{\text{cell}}} \left[\operatorname{grad} \overline{v} \cdot \mu \operatorname{grad} u - \overline{v}\omega^2 \rho\, u \right] d\Omega, \quad (3.6b)$$

$$a_1(v,u) = \mathrm{i} \int_{\Omega_{\text{cell}}} \left[\operatorname{grad} \overline{v} \cdot \mu \mathbf{d} u - \mathbf{d}\overline{v} \cdot \mu \operatorname{grad} u \right] d\Omega, \quad \text{and} \quad (3.6c)$$

$$a_2(v,u) = \int_{\Omega_{\text{cell}}} \mathbf{d}\overline{v} \cdot \mu \mathbf{d} u d\Omega. \quad (3.6d)$$

Notice that the dispersion relation is symmetric about $\mathbf{k} = \mathbf{0}$, and periodic with periodicity of $2\pi\mathbf{q}_i$. Moreover, $\mathbf{q}_i$ are the reciprocal primitive vectors satisfying $\mathbf{p}_i \cdot \mathbf{q}_j = 2\pi\delta_{ij}$, where δ_{ij} is a Kronecker delta. The complete dispersion relation, or equivalently, the band structure is the collection of dispersion curves obtained from solving (3.5).

We note that the quadratic eigenvalue problem (3.5) is also characterized by a discriminant $\mathcal{D}$, which allows distinguishing between propagating and non-propagating states [23]. Specifically, by replacing the test function v with u in (3.5), we obtain

$$\begin{aligned} 0 &= P(k)(u,u) \\ &= a_0(u,u) + k a_1(u,u) + k^2 a_2(u,u) \\ &= c + bk + ak^2, \end{aligned} \quad (3.7)$$

where a, b, and c are real-valued scalars due to the Hermitian character of $a_i(\cdot,\cdot)$. Then, the discriminant of the quadratic equation (3.7) is given by

$$\mathcal{D} = b^2 - 4ac. \quad (3.8)$$

A positive $\mathcal{D}$ implies a propagating state, or a real-valued k, and a negative $\mathcal{D}$ implies a non-propagating state, or a complex-valued k. If the sole aim of the unit cell design is to engineer the periodic structure to exhibit user-defined band gaps, the design problem can be driven by the discriminant, as was done in [23]. If, however, broader design goals are of interest, e.g., a target slow-wave region, lensing, or focusing, then relying on the discriminant alone is not sufficient. The more general problem of engineering the dispersive properties requires consideration of the group velocity: in the next section, we relate the group velocity to the parameters of the eigenvalue problem (3.5).

3.2.2 Group velocity in terms of the eigenpair

The group velocity $\mathbf{v}_g$ is defined as the real part of the complex group velocity [39], i.e.,

$$\mathbf{v}_g = \mathrm{Re}\left\{\mathrm{grad}_{\mathbf{k}}\omega\right\} = \sum_{i=1}^{N_\mathrm{d}} \mathrm{Re}\left\{\frac{\partial\omega}{\partial k_i}\right\}\mathbf{e}_i, \tag{3.9}$$

where $\mathbf{e}_i$ are orthonormal bases. Substituting v with u, and taking a partial derivative of equation (3.5) with respect to k of equation (3.5), results in

$$\begin{aligned}
0 =& \frac{\partial}{\partial k}P(k)\,(u,u) \\
=& 2\omega\frac{\partial\omega}{\partial k}a_{0,2}\,(u,u) + a_1\,(u,u) + 2ka_2\,(u,u) \\
&+ 2\mathrm{Re}\left\{a_{0,0}\left(\frac{\partial u}{\partial k},u\right)\right\} + 2\omega^2\mathrm{Re}\left\{a_{0,2}\left(\frac{\partial u}{\partial k},u\right)\right\} + 2k\mathrm{Re}\left\{a_1\left(\frac{\partial u}{\partial k},u\right)\right\} \\
&+ 2k^2\mathrm{Re}\left\{a_2\left(\frac{\partial u}{\partial k},u\right)\right\}.
\end{aligned} \tag{3.10}$$

In deriving (3.10), we decomposed $a_0(v,u)$ into two parts: a term with no ω-dependency, denoted by $a_{0,0}(v,u)$, and a term exhibiting ω^2-dependency, denoted by $\omega^2 a_{0,2}(v,u)$, i.e.,

$$a_0(v,u) = a_{0,0}(v,u) + \omega^2 a_{0,2}(v,u). \tag{3.11}$$

Taking the real part of equation (3.10), results in

$$\begin{aligned} 0 \; &= 2\omega \mathrm{Re}\left\{\frac{\partial \omega}{\partial k}\right\} a_{0,2}\left(u,u\right) + a_1\left(u,u\right) + 2\mathrm{Re}\left\{k\right\} a_2\left(u,u\right) \\ &+ 2\mathrm{Re}\left\{ a_{0,0}\left(\frac{\partial u}{\partial k}, u\right) + \omega^2 a_{0,2}\left(\frac{\partial u}{\partial k}, u\right) + k a_1\left(\frac{\partial u}{\partial k}, u\right) + k^2 a_2\left(\frac{\partial u}{\partial k}, u\right)\right\}. \end{aligned} \tag{3.12}$$

Assuming $\partial u/\partial k \in \mathcal{V}$, the terms involving $\partial u/\partial k$ in (3.12) vanish because u is the eigenvector satisfying (3.5). Then, the group velocity in the direction $\mathbf{d}$, or $\mathbf{v}_g \cdot \mathbf{d}$, is written in terms of the eigenpair (u,k) as:

$$\begin{aligned} v_g = \mathbf{v}_g \cdot \mathbf{d} &= \mathrm{Re}\left\{\frac{\partial \omega}{\partial k}\right\} \\ &= \mathrm{Re}\left\{ -\frac{a_1(u,u) + 2k\, a_2(u,u)}{2\omega\, a_{0,2}(u,u)} \right\} = -\frac{a_1(u,u) + 2\mathrm{Re}\left\{k\right\} a_2(u,u)}{2\omega\, a_{0,2}(u,u)}. \end{aligned} \tag{3.13}$$

Equation (3.13) can be regarded as the (scalar) elastodynamic equivalent of the *Hellmann-Feynman theorem* in quantum mechanics, which relates the derivative of the total energy to the derivative of the associated Hamiltonian. A similar approach for computing the group velocity in optics is reported in [54].

As it can be seen from equation (3.13), the group velocity in a given direction $\mathbf{d}$ is expressed explicitly in terms of the eigenvectors and eigenvalues of the associated eigenvalue problem. Thus, engineering the dispersive properties

of a unit cell to achieve a user-defined wave control outcome is equivalent to prescribing the group velocity along user-defined directions $\mathbf{d}$. Wave-steering, lensing, focusing, band gaps, etc, can all be cast in terms of a target group velocity profile (along one or multiple directions). For example, designing for a user-defined band gap requires that the target group velocity, for a set of desired directions, vanish, i.e.,

$$v_g = \mathbf{v}_g \cdot \mathbf{d} = -\frac{a_1(u,u) + 2\mathrm{Re}\left\{k\right\} a_2(u,u)}{2\omega\, a_{0,2}(u,u)} = 0. \tag{3.14}$$

We note that the band-gap criterion $\mathcal{D} < 0$ established in [23] is equivalent to prescribing a zero group velocity (See Appendix section 3.7.1 for proof).

We capture schematically the preceding discussion by considering the square unit cell depicted in Fig. 3.1, composed of 2 concentric square zones of piecewise constant material properties written in terms of non-dimensionalized quantities:

$$u^* = \frac{u}{p},\ \rho^* = \frac{\rho}{\rho_{\mathrm{avg}}},\ \mu^* = \frac{\mu}{\mu_{\mathrm{avg}}},\ x^* = \frac{x}{p},\ \omega^* = \frac{\omega p}{c_{\mathrm{avg}}},\ \text{and } k^* = kp, \tag{3.15}$$

where $p = \max|\mathbf{p}_i|$ and $(\,)_{\mathrm{avg}}$ is used for area-averaged quantities. The average wave speed c_{avg} is computed by $\sqrt{\mu_{\mathrm{avg}}/\rho_{\mathrm{avg}}}$. Then, Fig. 3.2(a) and Fig. 3.2(b) show the dispersion relation in terms of the complex band structure. In Fig. 3.2(a), hollow gray circles are used to denote the real part of the complex-valued k^*, whereas black dots are used for real-valued k^*. Because of the symmetry and periodicity of the dispersion relation, the band structure is provided only along the high symmetry lines Γ-X, Γ-M, and X-M, which circumscribe the irreducible Brillouin zone. The shaded zone shown in Fig. 3.2(a)

corresponds to an omni-directional band gap in the range $\omega^* \in (3.3, 3.6)$. Fig. 3.2(b) shows the imaginary part of the band structure: notice that the region corresponding to nonzero $\mathrm{Im}\{k^*\}$ represents the band gap. Similarly, Fig. 3.2(c) shows the discriminant $\mathcal{D}$ distribution: notice that the range of ω^* for which $\mathcal{D} < 0$ identifies uniquely the band gap. Lastly, Fig. 3.2(d) shows the group velocity, where clearly the zone where the velocity vanishes delineates the same band gap identified in Figs. 3.2(a), 3.2(b), and 3.2(c): for band gaps, all four representations shown in Fig. 3.2 are equivalent.

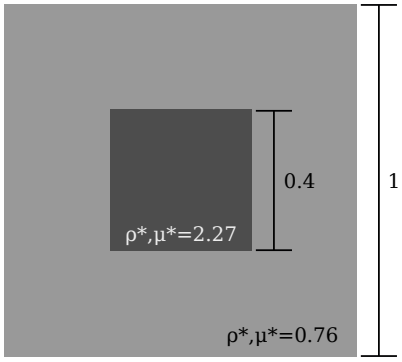

Figure 3.1: A square unit cell prototype

3.3 Group velocity control

In this section, we introduce the inverse problem and the associated solution method for designing a unit cell of a periodic medium when a target group velocity profile is given. We begin by defining the objective functional and the optimality conditions, where the inverse design problem is cast as a

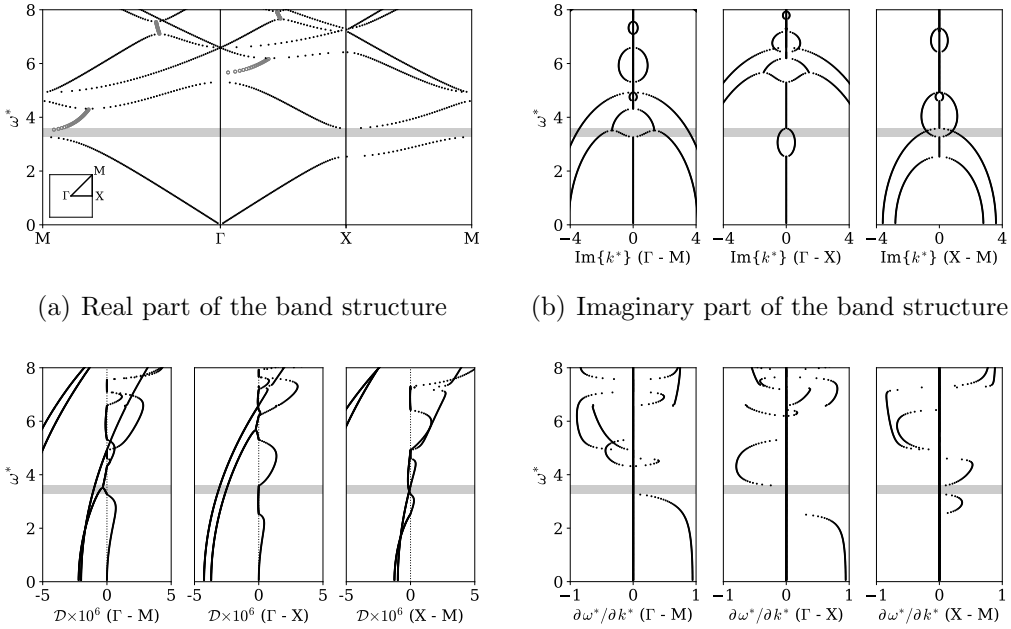

(a) Real part of the band structure

(b) Imaginary part of the band structure

(c) Discriminant $\mathcal{D}$

(d) Group velocity v_g

Figure 3.2: Complex band structure, discriminant, and group velocity: an omni-directional band gap is shown shaded in the range $\omega^* \in (3.3, 3.6)$; (a) real part of the band structure: real-valued k^* are shown as dots, whereas hollow circles are used for complex-valued k^*; (b) imaginary part of the band structure: non-propagating states (band gap) have nonzero imaginary part; (c) discriminant $\mathcal{D}$ distribution: non-propagating states (band gap) correspond to negative $\mathcal{D}$ values; (d) group velocity: non-propagating states (band gap) correspond to zero v_g

minimization problem. Then, we introduce a gradient-based inversion process to iteratively update the trial design variables ρ and μ to converge to the optimum. The design variables depend on the desirable parameterization of the unit cell, e.g., they can be material properties when the topology is fixed, or topological parameters when material properties are fixed, etc. Herein, we choose material properties ρ and μ as design variables, for a fixed unit cell topology.

3.3.1 Objective functional

We use a misfit functional to drive the inverse medium problem. The misfit functional M is defined using the distance between the computed group velocities of a trial unit cell and the prescribed target group velocities at different temporal frequencies, modes, and directions, i.e.,

$$\begin{aligned} M\left[\rho,\mu,u_{\alpha,\beta,\gamma},k_{\alpha,\beta,\gamma}\right] &= \sum_{\alpha}^{N_{\text{freq}}}\sum_{\beta}^{N_{\text{dir}}}\sum_{\gamma}^{N_{\text{mode}}}\frac{1}{2}\left[\left(\mathbf{v}_g\right)_{\alpha,\gamma}\cdot\mathbf{d}_\beta-\left(v_g^m\right)_{\alpha,\beta,\gamma}\right]^2 \\ &= \sum_{\alpha}^{N_{\text{freq}}}\sum_{\beta}^{N_{\text{dir}}}\sum_{\gamma}^{N_{\text{mode}}}\frac{1}{2}\Bigg[\text{Re}\left\{-\frac{a_1(u_{\alpha,\beta,\gamma},u_{\alpha,\beta,\gamma})+2k_{\alpha,\beta,\gamma}\,a_2(u_{\alpha,\beta,\gamma},u_{\alpha,\beta,\gamma})}{2\omega_\alpha\,a_{0,2}(u_{\alpha,\beta,\gamma},u_{\alpha,\beta,\gamma})}\right\} \\ &\qquad -\left(v_g^m\right)_{\alpha,\beta,\gamma}\Bigg]^2, \end{aligned} \tag{3.16}$$

where, N_{freq}, N_{dir}, and N_{mode} denote the number of frequencies, directions, and modes, respectively, over which the target group velocity $\left(v_g^m\right)_{\alpha,\beta,\gamma}$ is defined. Indices, α, β, and γ are used to denote the individual frequency, direction, and mode, respectively; to reduce notational congestion, we henceforth omit

the subscripts, i.e.,

$$v_g^m = \left(v_g^m\right)_{\alpha,\beta,\gamma},\ \mathbf{v}_g = \left(\mathbf{v}_g\right)_{\alpha,\gamma},\ \mathbf{d} = \mathbf{d}_\beta,$$
$$u = u_{\alpha,\beta,\gamma},\ k = k_{\alpha,\beta,\gamma},\ \text{and}\ \omega = \omega_\alpha. \tag{3.17}$$

We note that, should a band gap be a design target, then v_g^m should be set to zero.

Next, we augment the misfit functional M by side-imposing the dispersion relation using Lagrangian multipliers, i.e., let

$$L\left[\rho, \mu, u, k, v, \xi\right] = M\left[\rho, \mu, u, k\right] + E\left[\rho, \mu, u, k, v, \xi\right], \tag{3.18}$$

where L denotes the unit cell's Lagrangian, and E is the associated eigenvalue problem constraint defined as

$$\begin{aligned} E\left[\rho, \mu, u, k, v, \xi\right] = &\sum_{\alpha}^{N_{\text{freq}}} \sum_{\beta}^{N_{\text{dir}}} \sum_{\gamma}^{N_{\text{mode}}} \text{Re}\left\{P(k)(v, u)\right\} \\ &+ \sum_{\alpha}^{N_{\text{freq}}} \sum_{\beta}^{N_{\text{dir}}} \sum_{\gamma}^{N_{\text{mode}}} \frac{\xi}{2}\left[a_2(u, u) - 1\right]. \end{aligned} \tag{3.19}$$

In (3.19), the first term is the eigenvalue problem, whereas the second term is the side-imposition of the orthonormality condition that ensures a unique set of eigenvectors; v and ξ are the adjoint variables corresponding to u and k, respectively, where the indices α, β and γ have been again omitted. The unknown design variables μ and ρ are scalar quantities. Therefore, the inverse metamaterial design problem is defined as:

Given v_g^m, find ρ and μ such that

$$\min L\left[\rho, \mu, u, k, v, \xi\right]. \tag{3.20}$$

Various algorithms can be used to solve the minimization problem (3.20). For a differentiable L, gradient-based algorithms are, in general, computationally efficient when compared to gradient-free algorithms. We discuss next the optimality conditions, and a gradient-based approach to resolve the unit cell's properties.

3.3.2 Optimality conditions and adjoint sensitivity analysis

We seek a stationary point for L (3.20). Equivalently, we seek to satisfy the first-order optimality conditions, which read:

$$0 = \delta_v L\left[\ldots\right](\tilde{v}) \;\; \forall \tilde{v} \in \mathcal{V}, \;\; 0 = \delta_\xi L\left[\ldots\right]\left(\tilde{\xi}\right) \;\; \forall \tilde{\xi} \in \mathbb{R}; \tag{3.21a}$$

$$0 = \delta_u L\left[\ldots\right](\tilde{u}) \;\; \forall \tilde{u} \in \mathcal{V}, \;\; 0 = \delta_k L\left[\ldots\right]\left(\tilde{k}\right) \;\; \forall \tilde{k} \in \mathbb{C}; \quad \text{and} \tag{3.21b}$$

$$0 = \delta_\rho L\left[\ldots\right](\tilde{\rho}) \;\; \forall \tilde{\rho} \in \mathcal{W}, \;\; 0 = \delta_\mu L\left[\ldots\right](\tilde{\mu}) \;\; \forall \tilde{\mu} \in \mathcal{W}. \tag{3.21c}$$

We use $[\ldots]$ to abbreviate $[\rho, \mu, u, k, v, \xi]$ and $\tilde{(\,)}$ to denote the direction of the Gâteaux derivative. The function space $\mathcal{W}$ is defined as

$$\mathcal{W} = \left\{ u \in H^0(\Omega_{\text{cell}}) \middle| u(\boldsymbol{x}) = u\left(\boldsymbol{x} + \sum_{i=1}^{N_{\text{d}}} m_i \mathbf{p}_i\right) \;\; \forall \boldsymbol{x} \in \partial\Omega_{\text{cell}} \right\}. \tag{3.22}$$

We use an adjoint method to bypass a direct sensitivity analysis, which is, typically, required of any gradient-based algorithm. Accordingly, the first two optimality conditions (3.21a) and (3.21b) are first enforced for trial ρ and μ, and then the third optimality condition (3.21c) is used to define the Fréchet derivatives of L with respect to ρ and μ, denoted by g_ρ and g_μ, respectively. We note that (3.21c) will be satisfied only at the optimum. The detailed expression

of the Gâteaux derivatives implicated in the optimality conditions (3.21) are given in Appendix section 3.7.2. Enforcing (3.21a) yields the state eigenvalue problem:

Given $\rho \in \mathcal{W}$, $\mu \in \mathcal{W}$, and $\omega \in \mathbb{R}$, find $k \in \mathbb{C}$ and $u \in \mathcal{V} \setminus \{0\}$ such that

$$0 = P(k)(\tilde{v}, u) \ \forall \tilde{v} \in \mathcal{V} \quad \text{and} \tag{3.23a}$$

$$0 = \frac{\tilde{\xi}}{2} \left[a_2(u,u) - 1 \right] \ \forall \tilde{\xi} \in \mathbb{R}. \tag{3.23b}$$

The enforcement of (3.21b) yields the adjoint eigenvalue problem:

Given $\rho \in \mathcal{W}$, $\mu \in \mathcal{W}$, $\omega \in \mathbb{R}$, $k \in \mathbb{C}$, and $u \in \mathcal{V} \setminus \{0\}$, find $\xi \in \mathbb{R}$ and $v \in \mathcal{V}$ such that

$$\begin{aligned} 0 = {} & P(k)(v, \tilde{u}) + \xi a_2(u, \tilde{u}) - \frac{a_1(u,\tilde{u}) + 2\mathrm{Re}\left\{k\right\} a_2(u,\tilde{u})}{\omega a_{0,2}(u,u)} \left(v_g - v_g^m \right) \\ & + \frac{a_1(u,u) + 2\mathrm{Re}\left\{k\right\} a_2(u,u)}{\omega \left[a_{0,2}(u,u) \right]^2} a_{0,2}(u,\tilde{u}) \left(v_g - v_g^m \right) \ \forall \tilde{u} \in \mathcal{V} \quad \text{and} \end{aligned} \tag{3.24a}$$

$$0 = \tilde{k} a_1(v,u) + 2\tilde{k} k a_2(v,u) - \frac{\tilde{k} a_2(u,u)}{\omega a_{0,2}(u,u)} \left(v_g - v_g^m \right) \ \forall \tilde{k} \in \mathbb{C}. \tag{3.24b}$$

Lastly, given $\rho \in \mathcal{W}$, $\mu \in \mathcal{W}$, $\omega \in \mathbb{R}$, the solution of the state eigenvalue problem (3.23) (u, k), and the solution of the adjoint eigenvalue problem (3.24)

(v, ξ), find $g_\rho \in \mathcal{W}$ and $g_\mu \in \mathcal{W}$ such that (see Appendix section 3.7.2):

$$\int_{\Omega_{\text{cell}}} \tilde{\rho} g_\rho d\Omega = \sum_{\alpha}^{N_{\text{freq}}} \sum_{\beta}^{N_{\text{dir}}} \sum_{\gamma}^{N_{\text{mode}}} \text{Re}\left\{ - \int_{\Omega_{\text{cell}}} \overline{v} \omega^2 \tilde{\rho}\, u d\Omega \right\}$$
$$+ \sum_{\alpha}^{N_{\text{freq}}} \sum_{\beta}^{N_{\text{dir}}} \sum_{\gamma}^{N_{\text{mode}}} \text{Re}\left\{ - \left(\frac{\int_{\Omega_{\text{cell}}} \text{i} \left(\text{grad}\, \overline{u} \cdot \mu\, \mathbf{d} u - \mathbf{d}\overline{u} \cdot \mu \text{grad}\, u \right) d\Omega}{2\omega \left(\int_{\Omega_{\text{cell}}} \overline{u} \rho u d\Omega \right)^2} \right.\right.$$
$$\left.\left. + \frac{2k \int_{\Omega_{\text{cell}}} \overline{u} \mu u d\Omega}{2\omega \left(\int_{\Omega_{\text{cell}}} \overline{u} \rho u d\Omega \right)^2} \right) \left(\int_{\Omega_{\text{cell}}} \overline{u} \tilde{\rho} u d\Omega \right) (v_g - v_g^m) \right\}$$
$$\forall \tilde{\rho} \in \mathcal{W} \quad \text{and} \tag{3.25a}$$

$$\int_{\Omega_{\text{cell}}} \tilde{\mu} g_\mu d\Omega = \sum_{\alpha}^{N_{\text{freq}}} \sum_{\beta}^{N_{\text{dir}}} \sum_{\gamma}^{N_{\text{mode}}} \text{Re}\left\{ k \int_{\Omega_{\text{cell}}} \text{i} \left(\text{grad}\, \overline{v} \cdot \tilde{\mu}\, \mathbf{d} u - \mathbf{d}\overline{v} \cdot \tilde{\mu}\, \text{grad}\, u \right) d\Omega \right\}$$
$$+ \sum_{\alpha}^{N_{\text{freq}}} \sum_{\beta}^{N_{\text{dir}}} \sum_{\gamma}^{N_{\text{mode}}} \text{Re}\left\{ \int_{\Omega_{\text{cell}}} \text{grad}\, \overline{v} \cdot \tilde{\mu}\, \text{grad}\, u d\Omega \right\}$$
$$+ \sum_{\alpha}^{N_{\text{freq}}} \sum_{\beta}^{N_{\text{dir}}} \sum_{\gamma}^{N_{\text{mode}}} \text{Re}\left\{ k^2 \int_{\Omega_{\text{cell}}} \overline{v} \tilde{\mu}\, u d\Omega \right\}$$
$$+ \sum_{\alpha}^{N_{\text{freq}}} \sum_{\beta}^{N_{\text{dir}}} \sum_{\gamma}^{N_{\text{mode}}} \text{Re}\left\{ \frac{\xi}{2} \int_{\Omega_{\text{cell}}} \overline{u} \tilde{\mu}\, u d\Omega \right\}$$
$$+ \sum_{\alpha}^{N_{\text{freq}}} \sum_{\beta}^{N_{\text{dir}}} \sum_{\gamma}^{N_{\text{mode}}} \text{Re}\left\{ \left(\frac{\int_{\Omega_{\text{cell}}} \text{i} \left(\text{grad}\, \overline{u} \cdot \tilde{\mu} \mathbf{d} u - \mathbf{d}\overline{u} \cdot \tilde{\mu} \text{grad}\, u \right) d\Omega}{2\omega \int_{\Omega_{\text{cell}}} \overline{u} \rho u d\Omega} \right.\right.$$
$$\left.\left. + \frac{2k \int_{\Omega_{\text{cell}}} \overline{u} \tilde{\mu} u d\Omega}{2\omega \int_{\Omega_{\text{cell}}} \overline{u} \rho u d\Omega} \right) (v_g - v_g^m) \right\} \quad \forall \tilde{\mu} \in \mathcal{W}. \tag{3.25b}$$

Next, armed with the gradients (3.25), we use a conjugate gradient scheme to update the unit cell's properties per the details given in the next session.

3.3.3 Inversion process

The stationary point of the Lagrangian is reached only when all of the optimality conditions (3.21) are satisfied for some distributions of ρ and μ. Otherwise, the properties ρ and μ must be updated at each inversion iteration; the updates can be cast as:

$$\rho^{(k+1)} = \rho^{(k)} + \alpha_\rho^{(k)}\, d_\rho^{(k)} \quad \text{and} \tag{3.26a}$$

$$\mu^{(k+1)} = \mu^{(k)} + \alpha_\mu^{(k)}\, d_\mu^{(k)}, \tag{3.26b}$$

where, $\rho^{(k+1)}$, $\mu^{(k+1)}$, $\rho^{(k)}$, and $\mu^{(k)}$ denote properties at the $(k+1)$-th and k-th iterations, respectively; $d_\rho^{(k)}$ and $d_\mu^{(k)}$ are the search directions, and $\alpha_\rho^{(k)}$ and $\alpha_\mu^{(k)}$ are search lengths at the k-th iteration. We use a conjugate gradient method [21, 49], where

$$d_\rho^{(k)} = \begin{cases} -g_\rho^{(k)}, & k = 0 \\ -\dfrac{g_\rho^{(k)} \cdot g_\rho^{(k)}}{g_\rho^{(k-1)} \cdot g_\rho^{(k-1)}} g_\rho^{(k)}, & k > 0 \end{cases} \quad \text{and}$$

$$d_\mu^{(k)} = \begin{cases} -g_\mu^{(k)}, & k = 0 \\ -\dfrac{g_\mu^{(k)} \cdot g_\mu^{(k)}}{g_\mu^{(k-1)} \cdot g_\mu^{(k-1)}} g_\mu^{(k)}, & k > 0 \end{cases} . \tag{3.27}$$

The search lengths are obtained using the backtracking algorithm [49]. The updates (3.26) are repeated until trials ρ and μ converge. To robustify the inversion process, we also use a frequency continuation scheme, discussed in the

numerical results section. We summarize the inversion process in Algorithm 2.

Algorithm 2 Inversion process

1: Sample the target group velocity v_g^m ($v_g^m = 0$ for band gaps) at discrete frequencies
2: Define the geometry of the unit cell (e.g., periodicity, number of distinct material elements, etc.)
3: Set the error tolerance ε.
4: Initialize the iteration counter $l \leftarrow 0$
5: Set the initial search length
6: Set initial guesses for the material properties ρ_0 and μ_0
7: **for** $\|M_{l+1} - M_l\| > \varepsilon \|M_l\|$ **do**
8: Solve the state eigenvalue problem and evaluate M_l ▷ equations (3.16) and (3.23)
9: Solve the adjoint eigenvalue problem ▷ equation (3.24)
10: Compute the gradient of L ▷ equation (3.25)
11: Obtain the search direction (e.g., conjugate gradient method)
12: Update the material properties ρ_{l+1} and μ_{l+1} using backtracking algorithm; stop if sufficient-decrease condition is violated
13: Set $l \leftarrow l + 1$
14: **end for**

3.4 Numerical results

The inverse metamaterial design algorithm was implemented using finite elements in a parallel `C` code with the aid of `PETSc` [5] and `SLEPc` [51]. We describe next one- and two- dimensional examples that help demonstrate the capability and performance of the methodology.

3.4.1 Unit cell design in 1D

We consider first the case of a 3-material unit cell, whose target group velocity profile is given. The unit cell's topology is fixed, consisting of 3 equal size homogeneous sections with properties (ρ_1^*, μ_1^*), (ρ_2^*, μ_2^*), and (ρ_3^*, μ_3^*) (Fig. 3.3(a)). We seek the properties that will result in the given target group velocity profile shown in Fig. 3.3(b). The group velocity profile is sampled at 21 points, marked with $\times$'s in Fig. 3.3(b); notice that the given profile includes a band gap between $\omega^* = 1.8$ and $\omega^* = 4.4$. The inversion process was initiated using near homogeneous properties $\rho_1^* = \mu_1^* = \rho_3^* = \mu_3^* = 1$ and $\rho_2^* = \mu_2^* = 0.9$.

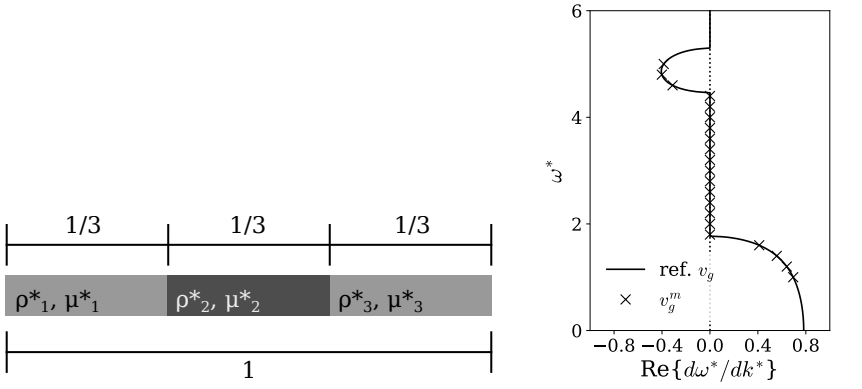

(a) Unit cell's topology (b) Target group velocity v_g^m

Figure 3.3: (a) Topology; (b) target group velocity profile of 1D unit cell design exhibiting a single band gap: solid line shows the synthetic group velocity profile, with $\times$ marking the sampling points

The optimizer resulted in the material distribution shown in Fig. 3.4(a); Fig. 3.4(b) depicts the group velocity and band structure of the unit cell using

the converged material parameters. As it can be seen, the inversely designed unit cell's velocity profile matches well the target profile.

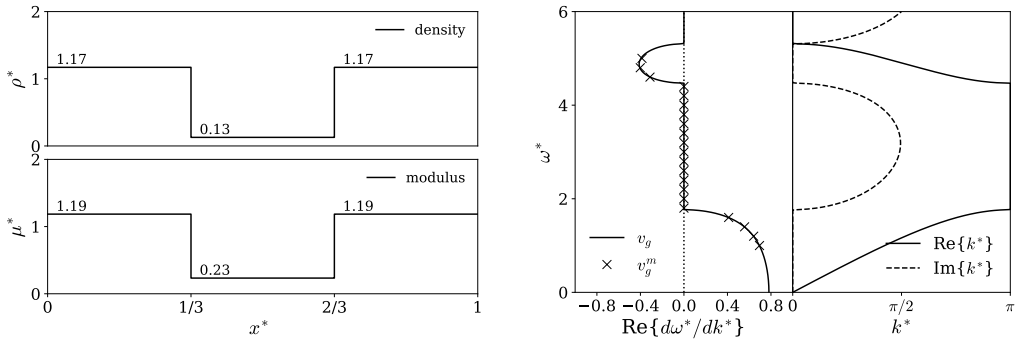

(a) Inverted material profile

(b) Inverted group velocity and band structure

Figure 3.4: (a) Inverted properties; (b) inverted group velocity profile and associated band structure exhibiting a single band gap

Using the same 3-material unit cell topology, we target next a design that ought to exhibit two band gaps, one in the $(2, 3)$ range, and a second one in the $(4.5, 5.5)$ range. We used 22 frequency points to populate the target velocity profile. We start the inversion process with $\rho_1^* = \mu_1^* = \rho_3^* = \mu_3^* = 1$ and $\rho_2^* = \mu_2^* = 0.9$. Fig. 3.5(a) shows the properties of the converged unit cell, characterized by $\rho_1^* = \rho_3^* = 1.29$, $\mu_1^* = \mu_3^* = 0.92$, $\rho_2^* = 0.68$, and $\mu_2^* = 0.36$, while Fig. 3.5(b) depicts the group velocity profile and associated band structure, where the target band gaps have been very clearly realized.

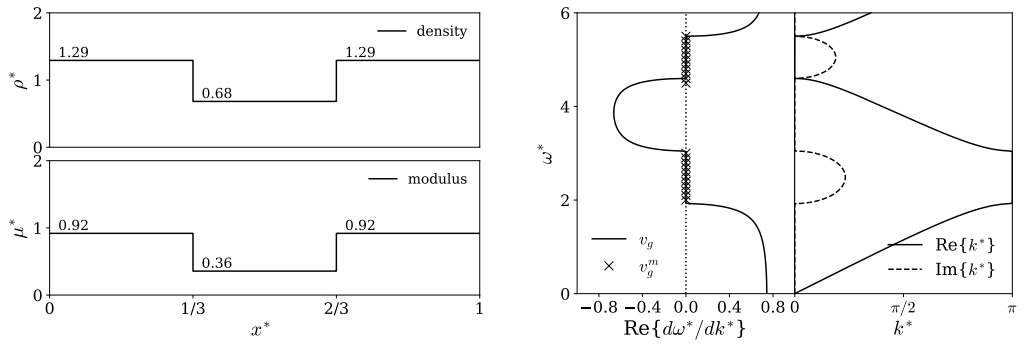

(a) Inverted material profile

(b) Inverted group velocity and band structure

Figure 3.5: (a) Inverted properties; (b) inverted group velocity profile and associated band structure exhibiting two band gaps

3.4.2 Unit cell design in 2D

To demonstrate the agility of the method, we consider next the design of a unit cell in two dimensions, where the design goal is for the metamaterial to exhibit an omni-directional band gap at a prescribed frequency range. Consider the 3-material, 4 meter-wide square unit cell depicted in Fig. 3.6(a); the Brillouin zone is shown in Fig. 3.6(b). The target band gap is set at $f \in (4.77, 10.25)$ Hz. The initial guesses are $\rho_1 = 8,250$ kg/m^3, $\mu_1 = 31.99$ MPa, $\rho_2 = 8,071$ kg/m^3, $\mu_2 = 19.72$ MPa, $\rho_3 = 7,919$ kg/m^3, $\mu_3 = 3.06$ MPa; the initial guesses are informed by a one-dimensional design problem targeting a similar band gap. We use 70 frequency points to mark the band gap ($N_{\text{freq}} = 70$); 2 directions ($N_{\text{dir}} = 2$, $\mathbf{d}_1 = (1, 0)$ and $\mathbf{d}_2 = (1/\sqrt{2}, 1/\sqrt{2})$); and 3 modes ($N_{\text{mode}} = 3$). Moreover, we use a staggered process, akin to frequency continuation, where we invert for the cell's properties by first driving the in-

version with a portion of the target band gap at $(4.77, 5.57)$ Hz. We then feed the converged material properties as initial guesses for a second stage, where the band gap is now defined between $(4.77, 6.37)$ Hz. We proceed similarly for a total of 7 stages by increasing the target range by 0.8 Hz at each stage, until the target band gap is completely covered.

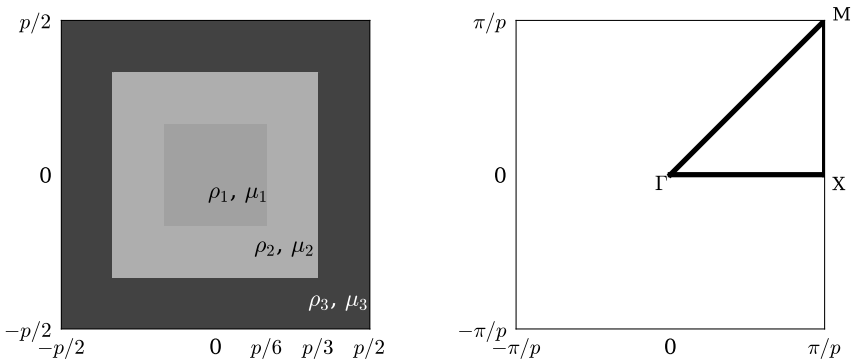

(a) Unit cell's topology (b) Brillouin zone

Figure 3.6: 2D design problem: (a) square unit cell; $p = 4$ m; (b) corresponding Brillouin zone and high symmetry lines Γ-M, Γ-X, and X-M

Fig. 3.7(a) shows the progression of the misfit functional M with the number of inversion iterations: notice that the end of each of stage is marked by a 7-order of magnitude reduction in the misfit. Fig. 3.7(b) shows the unit cell's inverted properties, while Fig. 3.8 shows the associated band structure, discriminant, and group velocity at the end of the first stage: a narrow band gap can be observed at the target range of the first stage, i.e., at $(4.77, 5.57)$ Hz. Fig. 3.9 shows the band structure, discriminant, and the group velocity at the end of the third stage: notice that, now, a wider band gap is achieved

at the target range of the third stage, i.e., at $f \in (4.77, 7.16)$ Hz, as intended. The band gap after the final stage is completed, is shown in Fig. 3.10: as it can be seen the target omni-directional band gap has been successfully attained at $f \in (4.77, 10.35)$ Hz.

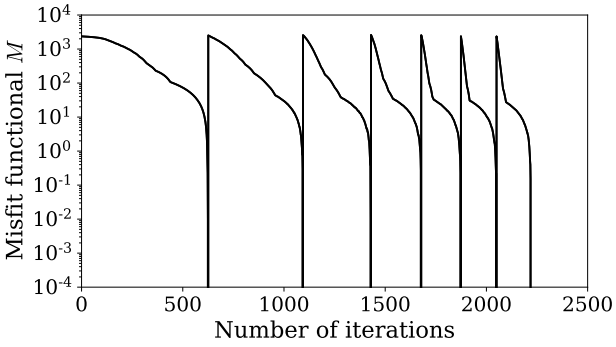

(a) Misfit functional M

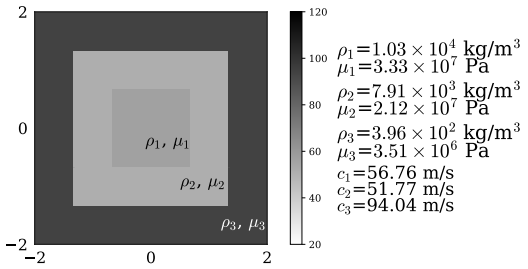

(b) Inverted unit cell material properties

Figure 3.7: 2D design example of an omni-directional band gap: (a) misfit functional progression under a 7-stage continuation scheme; (b) inverted unit cell material profile

3.4.3 Time-domain analyses

The 2D unit cell constructed in the preceding section's numerical experiment will perform as theoretically expected under ideal conditions of peri-

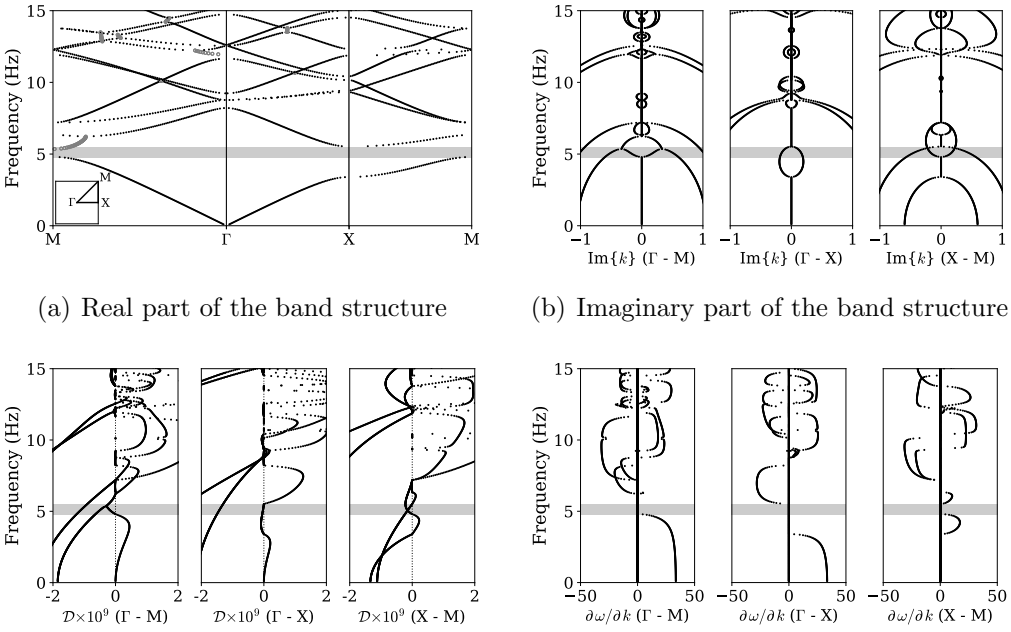

(a) Real part of the band structure

(b) Imaginary part of the band structure

(c) Discriminant $\mathcal{D}$

(d) Group velocity v_g

Figure 3.8: 2D omni-directional design example: band structure, discriminant, and group velocity at the end of the first inversion stage

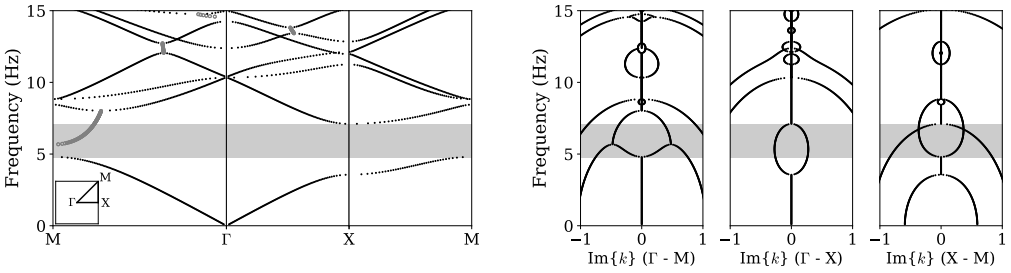

(a) Real part of the band structure

(b) Imaginary part of the band structure

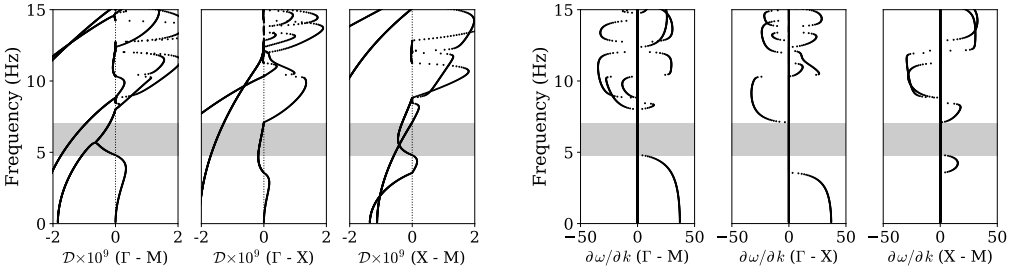

(c) Discriminant $\mathcal{D}$

(d) Group velocity v_g

Figure 3.9: 2D omni-directional design example: band structure, discriminant, and group velocity at the end of the third inversion stage

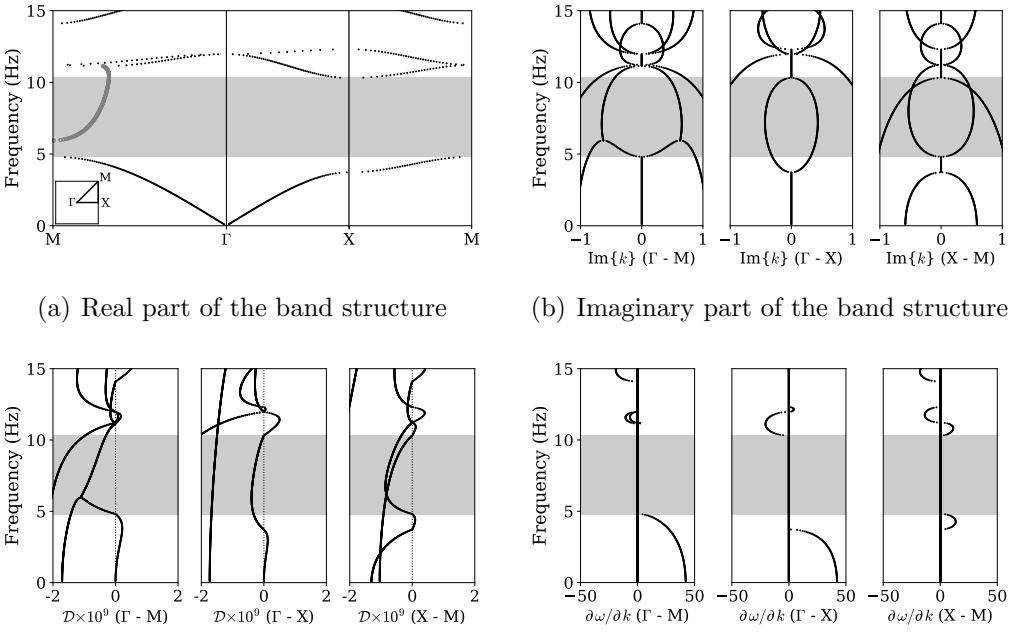

(a) Real part of the band structure

(b) Imaginary part of the band structure

(c) Discriminant $\mathcal{D}$

(d) Group velocity v_g

Figure 3.10: 2D omni-directional design example: band structure, discriminant, and group velocity at the end of the final inversion stage

odicity. However, in practice, a metamaterial can be realized only by stacking together a finite number of cells, thereby weakening periodicity. It is then of interest to assess a finite metamaterial block's (henceforth referred to as metablock) performance, especially in the time domain, which is typically the case with the strongest practical interest.

We use the unit cell depicted in Fig. 3.7(b) to create a metablock that is only 2 unit cells wide. The metablock occupies Ω_{m} and is embedded within a homogeneous domain Ω, as shown in Fig. 3.11. With the insertion of Ω_{m}, the homogeneous domain is partitioned into two parts, Ω_1 and Ω_2, such that $\Omega = \Omega_1 \cup \Omega_2 \cup \Omega_{\mathrm{m}}$. Moreover, the physical domain Ω is surrounded by a buffer of Perfectly-Matched-Layers (PMLs) Ω_{PML} to simulate wave propagation in an unbounded domain. Then, the computational domain becomes $\Omega \cup \Omega_{\mathrm{PML}}$. The material properties of the homogeneous domain $\Omega_1 \cup \Omega_2$ are $\rho = 2000$ kg/m^3 and $\mu = 80$ MPa; the corresponding wave speed is 200 m/s.

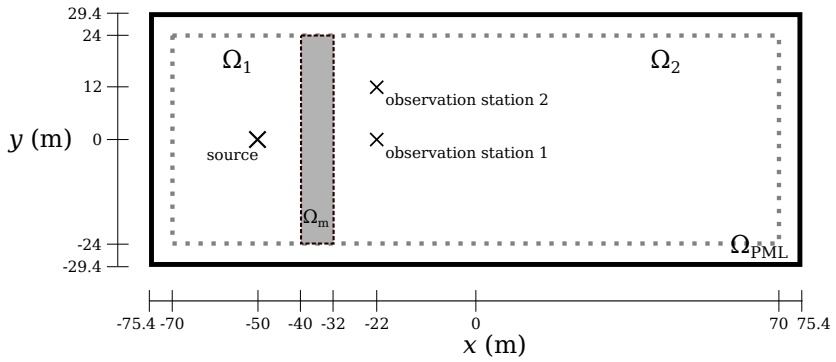

Figure 3.11: Computational domain for time-domain analyses; the metablock is placed in the shaded region

To examine whether an only 2-cell wide metablock is still capable of exhibiting an omni-directional band gap, we center the 8m-wide metablock at $(x, y) = (-36, 0)$m. A point source is placed at $(x, y) = (-50, 0)$m, and two observation stations are set at $(x, y) = (-22, 0)$m and $(-22, 12)$m, respectively. Two types of sources are used: monochromatic and a narrow-band Ricker pulse. To numerically simulate wave propagation within the heterogeneous metablock $\Omega_{\rm m}$ its homogeneous host $\Omega_1 \cup \Omega_2$, and the surrounding buffer $\Omega_{\rm PML}$, we use a symmetric mixed-field PML formulation, serendipity isoparametric finite elements, and a Newmark method for time integration; the details can be found in [32].

3.4.3.1 Monochromatic sources

To demonstrate the band-gap behavior of the metablock, we consider first two monochromatic sources: p_t^1 and p_t^2 driven at $f_1 = 2.5$ Hz and $f_2 = 8$ Hz, respectively, where

$$p_t^i = \sin(2\pi f_i t), \ i = 1 \text{ or } 2. \tag{3.28}$$

Recall that the frequency $f_1 = 2.5$ Hz is below the design band gap, while $f_2 = 8$ Hz is within the design band gap (Fig. 3.10). The first column of Fig. 3.12 shows snapshots, taken at $t = 4$s, of the wavefields resulting from p_t^1 for a homogeneous medium, i.e., in the absence of the metablock, whereas the second column of Fig. 3.12 depicts the wavefields generated in the presence of the metablock. As designed, and despite the small number of cells, the metablock allows the propagation of the 2.5Hz wave (Fig. 3.12(a) and 3.12(b)),

while arresting the propagation of the 8Hz wave (Fig. 3.12(c) and 3.12(d)). The third row of Fig. 3.12 shows the effect of the metablock on a dichromatic source driven by both frequencies (it is, effectively, the superposition of the two individual wavefields). It is noteworthy that the metablock's width (8m) is smaller than one-third of the shortest wavelength (25 m), which alludes to the metablock's subwavelength performance.

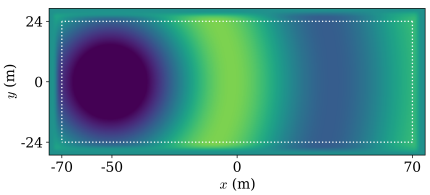

(a) Monochromatic source at $f_1 = 2.5$ Hz; without metablock

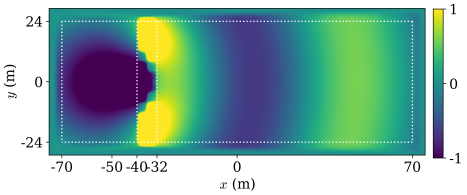

(b) Monochromatic source at $f_1 = 2.5$ Hz; with metablock

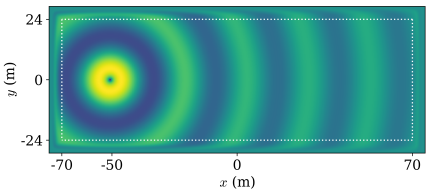

(c) Monochromatic source at $f_2 = 8$ Hz; without metablock

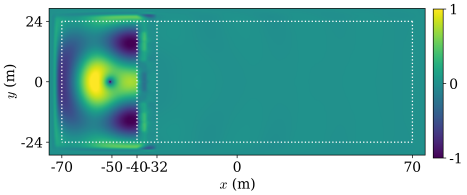

(d) Monochromatic source at $f_2 = 8$ Hz; with metablock

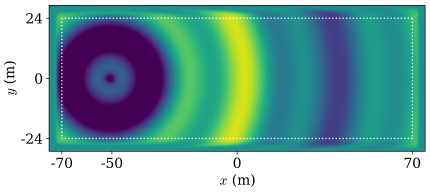

(e) Dichromatic source with $f_1 = 2.5$ Hz and $f_2 = 8$ Hz; without metablock

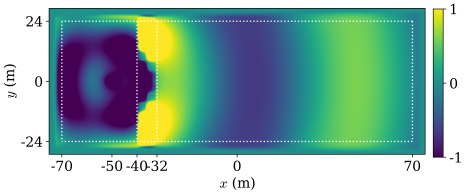

(f) Dichromatic source with $f_1 = 2.5$ Hz and $f_2 = 8$ Hz; with metablock

Figure 3.12: Snapshots at $t = 4$s of a wavefield induced by monochromatic and dichromatic sources

3.4.3.2 Ricker pulse - metablock width effect

Next, the same domain is excited using a source with a continuous narrow-band spectrum; specifically, we use a Ricker pulse with a central frequency of $f_r = 6$ Hz, or $\omega_r = 2\pi \cdot 6$ rad/s, defined as:

$$p_t^r = \frac{(0.25q^2 - 0.5)\, e^{0.25q^2} - 13e^{-13.5}}{0.5 + 13e^{-13.5}},\ 0 \leq t \leq \frac{6\sqrt{6}}{\omega_r}, \tag{3.29}$$

where $q = \omega_r t - 3\sqrt{6}$. Fig. 3.13(a) shows the time evolution of the wavefield in a homogeneous domain (no metablock), for reference. First, we compare the response when using metablocks of different widths: a 2 unit-cell-wide and a 4 unit-cell-wide metablock. Fig. 3.13(b) and Fig. 3.13(c) shows snapshots of the associated wavefields. Visually, it can be verified that low frequencies (below the band gap) pass undisturbed through the metablock in both cases. For a more detailed analysis, we use the time-domain response at the two observations stations.

Specifically, Figs. 3.14(a) and 3.14(b) compare the time traces with and without the metablocks: clearly, the 4 unit-cell-wide metablock's response shows a smoother response. The DFTs shown in Figs. 3.14(c) and 3.14(d) are more revealing: the presence of the design band gap between 4.77 Hz and 10.35 Hz is evident at both stations, suggesting also the omni-directionality feature of the metablock. Notice also that there is amplification (compared to the homogeneous case) at frequencies at the edges of the band gap, with stronger amplification at frequencies to the left than to the right of the band gap. If the amplification effect is undesirable, then the insertion of small material

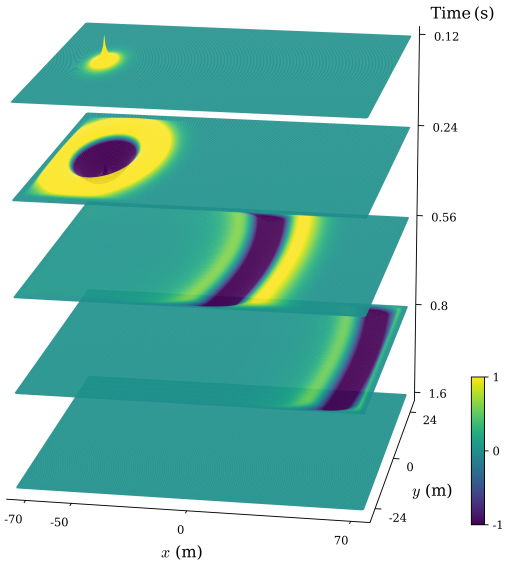

(a) Homogeneous domain

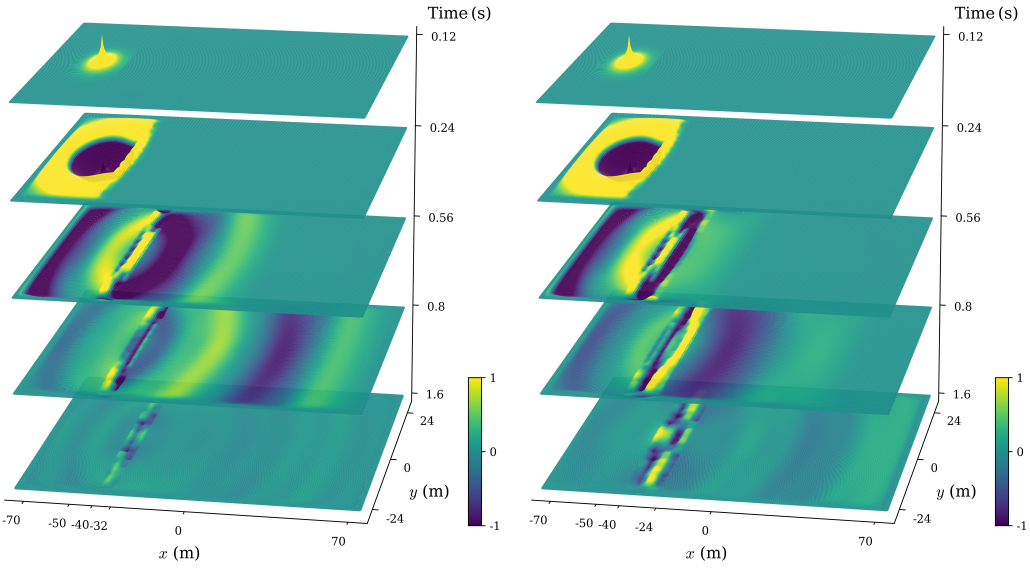

(b) With a 2 unit-cell-wide metablock at $x \in (-40, -32)$ m

(c) With a 4 unit-cell-wide metablock at $x \in (-40, -24)$ m

Figure 3.13: Various snapshots of a wavefield induced by a Ricker pulse with a central frequency of $f_r = 6$ Hz

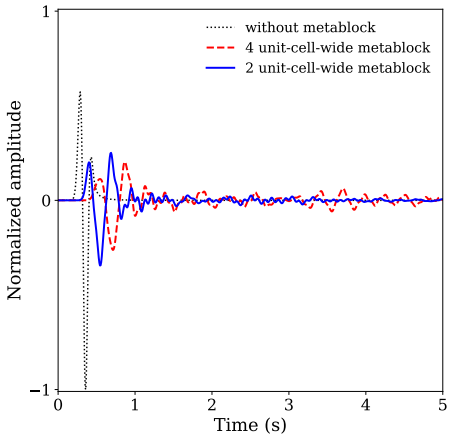

(a) Time trace at station 1 (-22,0)m

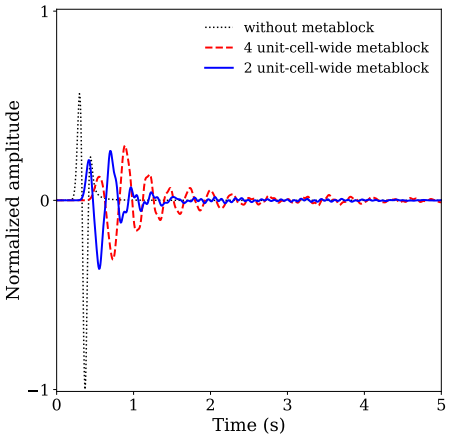

(b) Time trace at station 2 (-22,12)m

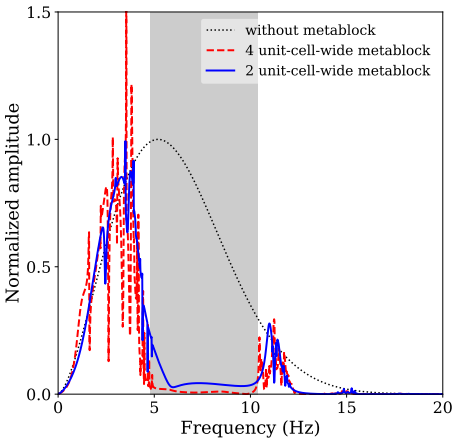

(c) DFT at station 1 (-22,0)m

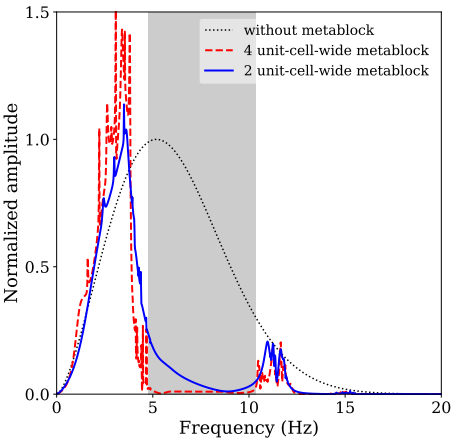

(d) DFT at station 2 (-22,12)m

Figure 3.14: (a),(b): Time traces at two observation stations; (c), (d): corresponding DFTs due to a Ricker pulse with $f_r = 6$ Hz; the target band gap is shaded in gray

damping in the unit cell could alleviate the response, without affecting the band gap (alternatively, the damping can also become part of the inversion problem). To demonstrate the effect, we introduce only in the metablock a 1% proportional damping [12] at $f = 2.5$ Hz. The resulting effect is shown in the time traces and the associated DFT of Fig. 3.15, where the amplification below the band gap has been reduced, with no appreciable effect on the band gap itself.

3.5 Conclusions

We proposed a systematic and general framework to design a unit cell of a periodic medium when given a user-defined target group velocity profile. The method can readily accommodate designing unit cells exhibiting one or more target band gaps. The inverse design metamaterial problem was cast as a dispersion-constrained optimization problem, which was then solved by enlisting an adjoint approach. We demonstrated the method with numerical results in one and two dimensions, including a problem involving the design of a two-dimensional unit cell exhibiting an omni-directional band gap. We also demonstrated the performance of the inversely designed metamaterials with numerical simulations in the time domain. The methodology is general and can be extended to three dimensions as well as to the case of vector waves.

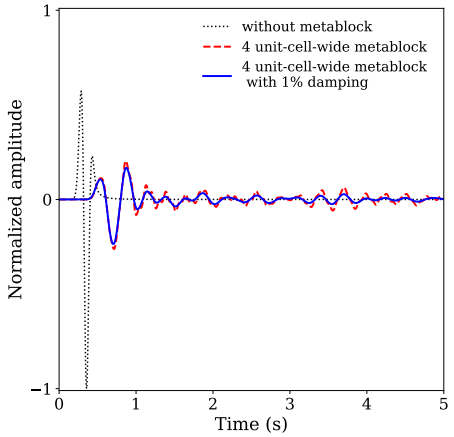

(a) Time trace at station 1 (-22,0)m

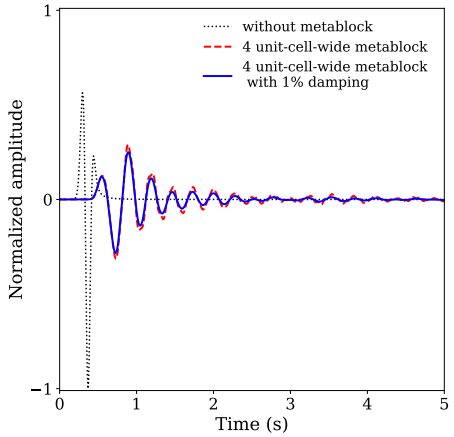

(b) Time trace at station 2 (-22,12)m

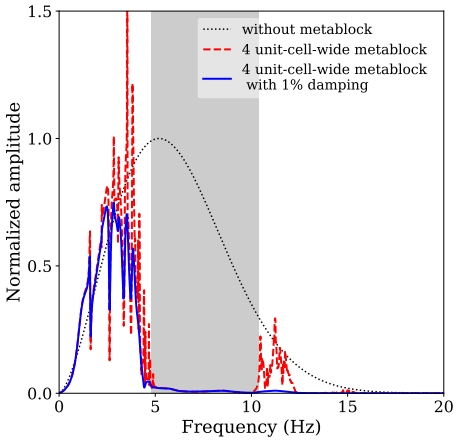

(c) DFT at station 1 (-22,0)m

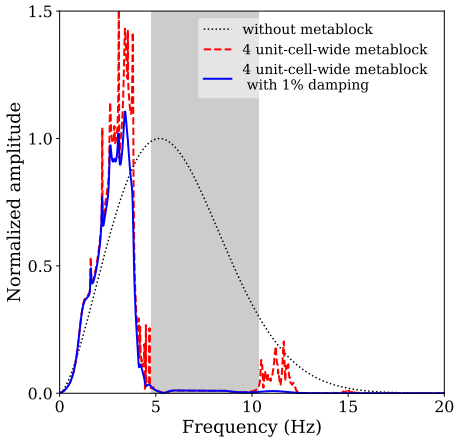

(d) DFT at station 2 (-22,12)m

Figure 3.15: (a),(b): Time traces at two observation stations; (c),(d): corresponding DFTs due to a Ricker pulse with $f_r = 6$ Hz; comparison of a lossless and lossy (1%) metablock; target band gap is shaded in gray

3.6 Acknowledgment

We wish to thank Professor Andrea Alù for fruitful discussions, as well as the anonymous reviewers for their constructive comments.

3.7 Appendix

3.7.1 Group velocity and band gap

We show that the vanishing of the group velocity at band gaps, i.e., that $\mathbf{v}_g \cdot \mathbf{d} = 0$, is equivalent to the negativity of the discriminant $\mathcal{D} < 0$ defined in (3.8). Taking the imaginary part of (3.5), when v is replaced by u, results in:

$$\begin{aligned} 0 &= \mathrm{Im}\left\{P(k)(u,u)\right\} \\ &= \mathrm{Im}\left\{k\right\} a_1(u,u) + 2\mathrm{Re}\left\{k\right\} \mathrm{Im}\left\{k\right\} a_2(u,u) \\ &= \mathrm{Im}\left\{k\right\} \left[a_1(u,u) + 2\mathrm{Re}\left\{k\right\} a_2(u,u)\right]. \end{aligned} \tag{3.30}$$

When $\mathcal{D} < 0$, then and only then is $\mathrm{Im}\left\{k\right\} \neq 0$, and from the above equation it must then also hold that:

$$0 = a_1(u,u) + 2\mathrm{Re}\left\{k\right\} a_2(u,u), \tag{3.31}$$

which is the numerator of the group velocity in the direction $\mathbf{d}$ in equation (3.13); qed.

3.7.2 Gâteaux derivatives of L

The Fréchet derivative g_u, or the gradient of L, is defined as [57]

$$\int_{\Omega_{\text{cell}}} \tilde{u} g_u d\Omega = \delta_u L[u](\tilde{u}), \tag{3.32}$$

where the Gâteaux derivative $\delta_u L$ is defined as

$$\delta_u L[u](\tilde{u}) = \left. \frac{d}{d\varepsilon} \right|_{\varepsilon=0} L[u + \varepsilon \tilde{u}]. \tag{3.33}$$

The Gâteaux derivatives with respect to the adjoint variables are

$$\delta_v L\left[\ldots\right](\tilde{v}) = \text{Re}\left\{P\left(k\right)(\tilde{v}, u)\right\} \quad \text{and} \tag{3.34a}$$

$$\delta_\xi L\left[\ldots\right]\left(\tilde{\xi}\right) = \frac{\tilde{\xi}}{2}\left[a_2\left(u,u\right) - 1\right] = \text{Re}\left\{\frac{\tilde{\xi}}{2}\left[a_2\left(u,u\right) - 1\right]\right\}. \tag{3.34b}$$

The Gâteaux derivatives with respect to the state variables are

$$\delta_u L\left[\ldots\right](\tilde{u}) = \delta_u M\left[\ldots\right](\tilde{u}) + \delta_u E\left[\ldots\right](\tilde{u}) \quad \text{and} \tag{3.35a}$$

$$\delta_k L\left[\ldots\right]\left(\tilde{k}\right) = \delta_k M\left[\ldots\right]\left(\tilde{k}\right) + \delta_k E\left[\ldots\right]\left(\tilde{k}\right), \tag{3.35b}$$

where

$$\begin{aligned}
\delta_u M\left[\ldots\right](\tilde{u}) = {} & \text{Re}\left\{-\frac{\text{Re}\left\{a_1(u,\tilde{u})\right\} + 2k\text{Re}\left\{a_2(u,\tilde{u})\right\}}{\omega a_{0,2}(u,u)}\right\}\left(v_g - v_g^m\right) \\
& + \text{Re}\left\{\frac{a_1(u,u) + 2ka_2(u,u)}{\omega\left[a_{0,2}(u,u)\right]^2}\text{Re}\left\{a_{0,2}(u,\tilde{u})\right\}\right\}\left(v_g - v_g^m\right) \\
& = \text{Re}\left\{-\frac{a_1(u,\tilde{u}) + 2\text{Re}\left\{k\right\}a_2(u,\tilde{u})}{\omega a_{0,2}(u,u)}\left(v_g - v_g^m\right)\right\} \\
& + \text{Re}\left\{\frac{a_1(u,u) + 2\text{Re}\left\{k\right\}a_2(u,u)}{\omega\left[a_{0,2}(u,u)\right]^2}a_{0,2}(u,\tilde{u})\left(v_g - v_g^m\right)\right\},
\end{aligned} \tag{3.36a}$$

$$\delta_k M\left[\ldots\right]\left(\tilde{k}\right) = \mathrm{Re}\left\{-\frac{\tilde{k}a_2(u,u)}{\omega a_{0,2}(u,u)}\right\}\left(v_g - v_g^m\right)$$
$$= \mathrm{Re}\left\{-\frac{\tilde{k}a_2(u,u)}{\omega a_{0,2}(u,u)}\left(v_g - v_g^m\right)\right\}, \tag{3.36b}$$

$$\delta_u E\left[\ldots\right](\tilde{u}) = \mathrm{Re}\left\{P(k)(v,\tilde{u})\right\} + \mathrm{Re}\left\{\xi a_2(u,\tilde{u})\right\}, \quad \text{and} \tag{3.36c}$$

$$\delta_k E\left[\ldots\right]\left(\tilde{k}\right) = \mathrm{Re}\left\{\tilde{k}a_1(v,u) + 2k\tilde{k}a_2(v,u)\right\}. \tag{3.36d}$$

The Gâteaux derivatives with respect to the design variables are

$$\delta_\rho L\left[\ldots\right](\tilde{\rho}) = \delta_\rho M\left[\ldots\right](\tilde{\rho}) + \delta_\rho E\left[\ldots\right](\tilde{\rho}) \quad \text{and} \tag{3.37a}$$

$$\delta_\mu L\left[\ldots\right](\tilde{\mu}) = \delta_\mu M\left[\ldots\right](\tilde{\mu}) + \delta_\mu E\left[\ldots\right](\tilde{\mu}), \tag{3.37b}$$

where

$$\delta_\rho M[\ldots](\tilde{\rho}) = \sum_{\alpha}^{N_{\mathrm{freq}}}\sum_{\beta}^{N_{\mathrm{dir}}}\sum_{\gamma}^{N_{\mathrm{mode}}} \mathrm{Re}\left\{-\left(\frac{\int_{\Omega_{\mathrm{cell}}} \mathrm{i}\left(\mathrm{grad}\,\overline{u}\cdot\mu\,\mathbf{d}u - \mathbf{d}\overline{u}\cdot\mu\mathrm{grad}\,u\right)d\Omega}{2\omega\left(\int_{\Omega_{\mathrm{cell}}}\overline{u}\rho u d\Omega\right)^2}\right.\right.$$
$$\left.\left. + \frac{2k\int_{\Omega_{\mathrm{cell}}}\overline{u}\mu u d\Omega}{2\omega\left(\int_{\Omega_{\mathrm{cell}}}\overline{u}\rho u d\Omega\right)^2}\right)\left(\int_{\Omega_{\mathrm{cell}}}\overline{u}\tilde{\rho}u d\Omega\right)\left(v_g - v_g^m\right)\right\}, \tag{3.38a}$$

$$\delta_\mu M[\ldots](\tilde{\mu}) = \sum_{\alpha}^{N_{\mathrm{freq}}}\sum_{\beta}^{N_{\mathrm{dir}}}\sum_{\gamma}^{N_{\mathrm{mode}}} \mathrm{Re}\left\{\left(\frac{\int_{\Omega_{\mathrm{cell}}} \mathrm{i}\left(\mathrm{grad}\,\overline{u}\cdot\tilde{\mu}\mathbf{d}u - \mathbf{d}\overline{u}\cdot\tilde{\mu}\mathrm{grad}\,u\right)d\Omega}{2\omega\int_{\Omega_{\mathrm{cell}}}\overline{u}\rho u d\Omega}\right.\right.$$
$$\left.\left. + \frac{2k\int_{\Omega_{\mathrm{cell}}}\overline{u}\tilde{\mu}u d\Omega}{2\omega\int_{\Omega_{\mathrm{cell}}}\overline{u}\rho u d\Omega}\right)\left(v_g - v_g^m\right)\right\}, \tag{3.38b}$$

$$\delta_\rho E[\ldots](\tilde{\rho}) = \sum_{\alpha}^{N_{\text{freq}}} \sum_{\beta}^{N_{\text{dir}}} \sum_{\gamma}^{N_{\text{mode}}} \operatorname{Re}\left\{ -\int_{\Omega_{\text{cell}}} \overline{v}\omega^2 \tilde{\rho}\, u d\Omega \right\}, \quad \text{and} \tag{3.38c}$$

$$\begin{aligned}
\delta_\mu E[\ldots](\tilde{\mu}) = & \sum_{\alpha}^{N_{\text{freq}}} \sum_{\beta}^{N_{\text{dir}}} \sum_{\gamma}^{N_{\text{mode}}} \operatorname{Re}\left\{ k \int_{\Omega_{\text{cell}}} \mathrm{i} \left(\operatorname{grad} \overline{v} \cdot \tilde{\mu}\, \mathbf{d}u - \mathbf{d}\overline{v} \cdot \tilde{\mu} \operatorname{grad} u \right) d\Omega \right\} \\
& + \sum_{\alpha}^{N_{\text{freq}}} \sum_{\beta}^{N_{\text{dir}}} \sum_{\gamma}^{N_{\text{mode}}} \operatorname{Re}\left\{ \int_{\Omega_{\text{cell}}} \operatorname{grad} \overline{v} \cdot \tilde{\mu} \operatorname{grad} u d\Omega \right\} \\
& + \sum_{\alpha}^{N_{\text{freq}}} \sum_{\beta}^{N_{\text{dir}}} \sum_{\gamma}^{N_{\text{mode}}} \operatorname{Re}\left\{ k^2 \int_{\Omega_{\text{cell}}} \overline{v}\tilde{\mu}\, u d\Omega \right\} \\
& + \sum_{\alpha}^{N_{\text{freq}}} \sum_{\beta}^{N_{\text{dir}}} \sum_{\gamma}^{N_{\text{mode}}} \operatorname{Re}\left\{ \frac{\xi}{2} \int_{\Omega_{\text{cell}}} \overline{u}\tilde{\mu}\, u d\Omega \right\}.
\end{aligned} \tag{3.38d}$$

Chapter 4

Inverse band gap design of elastic metamaterials for P and SV wave control[1]

We describe a systematic approach for engineering the dispersive properties of elastic metamaterials in order to band-gap, at user-defined frequency ranges, the propagation of elastic waves, accounting simultaneously for both P and SV waves. To this end, we focus on the inverse design of a metamaterial's unit cell, and cast the design problem as an optimization problem, driven by the desired band gap, and constrained only by the cell's dispersive characteristics; the latter are expressed in terms of the Floquet-Bloch eigenvalue problem. Numerical results in the time-domain, using metamaterial assemblies with only narrow periodicity, demonstrate that the engineered metamaterial attains the desired behavior. Extensions to wave steering, shielding, and other wave-control applications, follow naturally.

[1]This chapter has been submitted as a journal article for possible publication: Heedong Goh and Loukas F. Kallivokas, Inverse band gap design of elastic metamaterials for P and SV wave control, *Computer Methods in Applied Mechanics and Engineering*, 2020. The dissertation author had significant contributions to the article that included the development of the methodology, its implementation, the numerical results, and the related discussion.

4.1 Introduction

Fueled by recent advances in solid state physics, photonics, and phononics, dispersion engineering refers to the emerging field of engineering the properties of materials in order to achieve user-defined behavior, often uncommon in nature (thus giving rise to the metamaterial designation of such materials), which, in the context of wave propagation, would allow for novel ways of wave motion control. To attain the desired behavior, the materials need not necessarily be engineered *ab initio*; instead, for example, one could engineer the spatial arrangement of real materials in periodic (or even aperiodic) assemblies, in a manner that would then endow the assembly with the target dispersive behavior. In this way, wave-steering [46], wave-control [58], cloaking [3,43,55], band-gapping [47], lensing [35,45], and other wave-control effects become possible.

To date, engineering the dispersive behavior has been attempted mostly on an *ad hoc* basis, and primarily in the context of acoustics or electromagnetics, which enjoy the benefit of a single wave type/wave velocity. By contrast, in elastodynamics, the presence of two distinct wave types turns the engineering of the medium's dispersive characteristics into a particularly challenging task.

Engineering material behavior, based on user-defined performance metrics, is, fundamentally, an inverse medium problem, and, therefore, it can be treated using established mathematical approaches for inversion. Here, we build upon recent advances in engineering metamaterials for band-gapping

scalar waves (single wave type) [22, 23], to the all important and more challenging case of vector waves (two wave types). The goal is to be able to intercept propagating waves with suitably engineered metabarriers in order to arrest (filter) the propagation of elastic waves at user-defined frequency ranges (the band gaps). While the discussion herein is driven by band gaps, other wave control objectives can be similarly pursued by appropriately adapting the developed framework.

4.2 Preliminaries

Let us assume that the metamaterial, whose dispersive behavior we intend to engineer, consists of identical, periodically distributed, unit cells (Fig.4.1): due to the periodicity, it is sufficient to engineer the unit cell in order to endow the metamaterial with the desired target behavior. The dispersive behavior of the unit cell is completely defined by the associated eigenvalue problem (EP), cast over the unit cell and subject to periodic boundary conditions. While the EP captures the unit cell's dispersive characteristics, it cannot be readily manipulated to meet a specific design goal: instead, we use the EP to extract the band structure, i.e., the dispersion curves/surfaces associated with the irreducible Brillouin zone (IBZ). The IBZ affords us the necessary flexibility to accommodate wave-control design goals, and in particular when targeting directionality constraints. We highlight next the steps leading to the unit-cell design informed by the IBZ: in short, *dispersion engineering design goals* are first translated to specific *group velocity design profiles*, which are,

in turn, shown to uniquely depend on the characteristics of the unit cell's *EP and IBZ*.

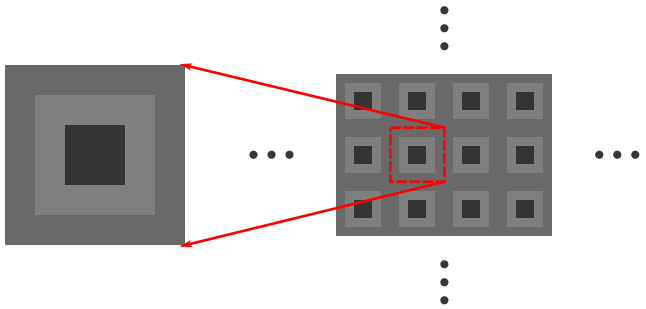

Figure 4.1: The unit cell and the metamaterial assembly consisting of periodically arranged heterogeneous unit cells

4.2.1 The eigenvalue problem for elastic waves in periodic media

In the frequency domain, the propagation of elastic waves in a heterogeneous domain is described by Navier's equations:

$$\mathbf{0} = \operatorname{div} \underline{\underline{\mathbf{C}}}(\boldsymbol{x}) \left[\operatorname{grad} \mathbf{U}(\boldsymbol{x})\right] + \rho(\boldsymbol{x}) \omega^2 \mathbf{U}(\boldsymbol{x}), \quad \boldsymbol{x} \in \mathbb{R}^{N_\mathrm{d}}, \tag{4.1}$$

where N_d denotes the order of the spatial dimensionality, $\mathbf{U}(\boldsymbol{x})$ is the displacement vector, ω is the circular frequency, $\rho(\boldsymbol{x})$ is mass density, and $\underline{\underline{\mathbf{C}}}(\boldsymbol{x})$ is the elasticity tensor. We use regular font to denote scalars, and boldfaced font for vectors, matrices, and first-rank tensors; a single underline is used for second-rank tensors; and a double underline is used for fourth-rank tensors. The elasticity tensor $\underline{\underline{\mathbf{C}}}$ for a linear isotropic medium reads:

$$\underline{\underline{\mathbf{C}}}(\boldsymbol{x})[\ ] = \mu(\boldsymbol{x})[\ ] + \mu(\boldsymbol{x})[\ ]^\intercal + \lambda(\boldsymbol{x}) \operatorname{tr}[\ ] \underline{\mathbf{I}}, \tag{4.2}$$

where $\lambda(\boldsymbol{x})$ and $\mu(\boldsymbol{x})$ are the Lamé parameters, $\underline{\mathbf{I}}$ is the identity tensor and $[\ ]^{\intercal}$ denotes the transpose of the subtended quantity. The problem implied by (4.1) becomes periodic when the material properties are periodic, i.e., when $\forall \boldsymbol{x} \in \mathbb{R}^{N_\mathrm{d}}$ and $\forall m_i \in \mathbb{Z}$,

$$\lambda(\boldsymbol{x}) = \lambda\left(\boldsymbol{x} + \sum_{i=1}^{N_\mathrm{d}} m_i \mathbf{p}_i\right), \tag{4.3a}$$

$$\mu(\boldsymbol{x}) = \mu\left(\boldsymbol{x} + \sum_{i=1}^{N_\mathrm{d}} m_i \mathbf{p}_i\right), \quad \text{and} \tag{4.3b}$$

$$\rho(\boldsymbol{x}) = \rho\left(\boldsymbol{x} + \sum_{i=1}^{N_\mathrm{d}} m_i \mathbf{p}_i\right). \tag{4.3c}$$

In the above, $\mathbf{p}_i \in \mathbb{R}^{N_\mathrm{d}}$ is the primitive vector that defines the periodicity in the i-th spatial direction. Then, the *Floquet-Bloch theorem* [4] provides the general solution of the periodic problem as:

$$\mathbf{U}(\boldsymbol{x}) = e^{\mathrm{i}\mathbf{k}\cdot\boldsymbol{x}}\mathbf{u}(\boldsymbol{x}), \tag{4.4}$$

where the displacement-like quantity $\mathbf{u}(\boldsymbol{x})$ is periodic with the same periodicity of the original problem, and $\mathbf{k}$ denotes the Floquet-Bloch wavevector. Substituting (4.4) into the Navier equation (4.1), yields the *Floquet-Bloch EP*. In weak form, the EP reads: given $\omega \in \mathbb{R}$ and $\mathbf{d} \in \mathbb{R}^{N_\mathrm{d}}$, find $k \in \mathbb{C}$ and $\mathbf{u} \in \mathcal{V}^{N_\mathrm{d}} \setminus \{\mathbf{0}\}$ such that

$$P(k)(\mathbf{v}, \mathbf{u}) \equiv a_0(\mathbf{v}, \mathbf{u}) + k a_1(\mathbf{v}, \mathbf{u}) + k^2 a_2(\mathbf{v}, \mathbf{u}) = 0, \quad \forall \mathbf{v} \in \mathcal{V}^{N_\mathrm{d}}, \tag{4.5}$$

where

$$\mathcal{V} = \left\{ w \in H^1\left(\Omega_{\text{cell}}\right) \,|\, w\left(\boldsymbol{x}\right) = w\left(\boldsymbol{x} + \sum_{i=1}^{N_{\text{d}}} m_i \mathbf{p}_i\right) \;\forall \boldsymbol{x} \in \partial\Omega_{\text{cell}} \right\}, \tag{4.6a}$$

$$a_0\left(\mathbf{v}, \mathbf{u}\right) = \int_{\Omega_{\text{cell}}} \left\{ \operatorname{grad} \overline{\mathbf{v}} : \underline{\underline{\mathbf{C}}} \left[\operatorname{grad} \mathbf{u}\right] - \overline{\mathbf{v}} \cdot \omega^2 \rho\, \mathbf{u} \right\} d\Omega, \tag{4.6b}$$

$$a_1\left(\mathbf{v}, \mathbf{u}\right) = \mathrm{i} \int_{\Omega_{\text{cell}}} \left\{ \operatorname{grad} \overline{\mathbf{v}} : \underline{\underline{\mathbf{C}}} \left[\mathbf{u} \otimes \mathbf{d}\right] - \left(\overline{\mathbf{v}} \otimes \mathbf{d}\right) : \underline{\underline{\mathbf{C}}} \left[\operatorname{grad} \mathbf{u}\right] \right\} d\Omega, \quad \text{and} \tag{4.6c}$$

$$a_2\left(\mathbf{v}, \mathbf{u}\right) = \int_{\Omega_{\text{cell}}} \left(\overline{\mathbf{v}} \otimes \mathbf{d}\right) : \underline{\underline{\mathbf{C}}} \left[\mathbf{u} \otimes \mathbf{d}\right] d\Omega. \tag{4.6d}$$

In the above, Ω_{cell} is the domain of a unit cell, $\mathbf{v}$ is a test function, an overline $\overline{(\,)}$ denotes a complex-conjugate of the subtended quantity, $(:)$ denotes double contraction, $\otimes$ denotes tensor product, and $\mathbf{d}$ is a direction of interest such that $\mathbf{k} = k\mathbf{d}$, with $|\mathbf{d}| = 1$.

We prefer to drive the unit cell's design using the quadratic EP (4.5), cast in terms of the wavenumber k, instead of the more common choice of the linear EP (cast in terms of ω^2), since, as discussed in [23], the quadratic EP provides a direct, quantitative, description of the band gaps, whereas the linear EP can only offer an indirect description. Thus, given a (real-valued) circular frequency ω, we use (4.5) to find the complex-valued wavenumbers (wavevectors) k ($\mathbf{k}$): the set of all dispersion curves/surfaces relating ω to $\mathbf{k}$ forms the *band structure* of the unit cell. We note that the Floquet-Bloch wavevector $\mathbf{k}$ is periodic in the wavevector space (or reciprocal space); the periodicity in the reciprocal space is captured by the reciprocal primitive vector $\mathbf{q}_i$, which is related to the physical space's primitive vector $\mathbf{p}_i$ via $\mathbf{p}_i \cdot \mathbf{q}_j = 2\pi\delta_{ij}$,

with δ_{ij} denoting the Kronecker delta. Similarly, the dispersion curves of a periodic problem are also periodic in the wavevector space with periodicity equal to that of the primitive vector $\mathbf{q}_i$.

To study the band structure we turn to the unit cell (the Wigner–-Seitz cell) in the reciprocal space: the Wigner-Seitz cell defines the Brillouin zone, which is, effectively, the (periodic) trace of the dispersion curves in the wavevector space. The dispersion curves have symmetries that allow a further reduction of the Brillouin zone to the, so-called, *irreducible Brillouin zone* (IBZ), which is delineated off of the Brillouin zone while ensuring that no information is lost. Practically, dispersion curves are often plotted over only the *high-symmetry lines*, which are the edges of the IBZ. For example, a square unit cell in the physical space has a square Wigner-Seitz cell in the reciprocal/wavevector space (i.e., a square Brillouin zone), which, upon reduction, results in a triangular IBZ (Fig. 4.2). The vertices of the triangular IBZ are denoted by Γ, X, and M, and the three high-symmetry lines are Γ-X, Γ-M, and X-M. In this paper, we plot dispersion curves for wavevectors corresponding only to the propagating states to avoid congesting the plots.

We remark that to compute the band structure on the high-symmetry lines that do not connect back to the origin Γ, e.g., X-M in Figure 4.2, an offset direction $\mathbf{d}_o$ is required, such that $\mathbf{k} = k\mathbf{d} + \mathbf{d}_o$: the associated EP with an offset direction is given in section 4.7.1.

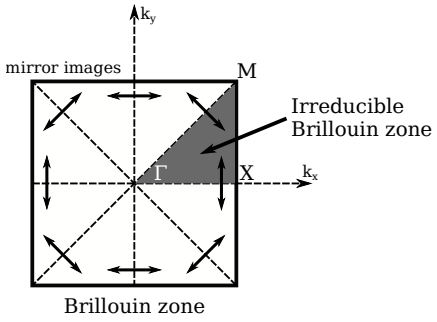

Figure 4.2: The Brillouin zone and the IBZ of a square unit cell in wavevector space

4.2.2 Group velocity, energy velocity, and the band gap

We are interested in engineering the unit cell to exhibit user-defined dispersive behavior, and in particular, to adhere to a user-prescribed group velocity profile. Band gaps are only a particular case of a group velocity profile. Specifically, a band gap is a frequency range $\mathcal{G}$ for which there are no propagating states: at the band gap frequencies, the Floquet-Bloch wavenumbers are complex-valued with nonzero imaginary parts ($\mathrm{Im}\{k\} \neq 0$, $\forall \omega \in \mathcal{G}$), whereas outside the gap the wavenumbers are purely real-valued ($k \in \mathbb{R}$, $\forall \omega \notin \mathcal{G}$). As will be discussed, band gaps arise when the group velocity vanishes. Then, to set up the inverse design problem, it is necessary to relate the group velocity to the unit-cell EP.

The group velocity $\mathbf{v}_g$ is defined as [39]:

$$\mathbf{v}_g = \mathrm{Re}\left\{\mathrm{grad}_k \omega\right\}, \tag{4.7}$$

while the directional group velocity along $\mathbf{d}$ is:

$$v_g = \mathbf{v}_g \cdot \mathbf{d} = \mathrm{Re}\left\{\frac{\partial \omega}{\partial k}\right\}. \tag{4.8}$$

To relate the group velocity to the EP, we differentiate (4.5) with respect to k, i.e.,

$$\begin{aligned} 0 &= \frac{\partial}{\partial k} P(k)(\mathbf{u}, \mathbf{u}) \\ &= 2\omega \frac{\partial \omega}{\partial k} a_{0,2}(\mathbf{u}, \mathbf{u}) + a_1(\mathbf{u}, \mathbf{u}) + 2k a_2(\mathbf{u}, \mathbf{u}) \\ &\quad + 2\mathrm{Re}\left\{P(k)\left(\frac{\partial \mathbf{u}}{\partial k}, \mathbf{u}\right)\right\}. \end{aligned} \tag{4.9}$$

In the above, the last term vanishes, assuming that $\partial \mathbf{u}/\partial k \in \mathcal{V}^{N_\mathrm{d}}$. Then, by taking the real part of the remainder of (4.9), while considering (4.8), yields:

$$v_g = -\frac{a_1(\mathbf{u}, \mathbf{u}) + 2\mathrm{Re}\{k\}\, a_2(\mathbf{u}, \mathbf{u})}{2\,\omega\, a_{0,2}(\mathbf{u}, \mathbf{u})}, \tag{4.10}$$

where

$$a_{0,2}(\mathbf{v}, \mathbf{u}) = -\int_{\Omega_\mathrm{cell}} \overline{\mathbf{v}} \cdot \rho\, \mathbf{u}\, d\Omega. \tag{4.11}$$

Expression (4.10) is the sought relation between the (directional) group velocity v_g and the eigenpair $(\mathbf{u}, k)$ of the Floquet-Bloch unit-cell EP: it can be viewed as the elastodynamic equivalent of the Hellmann-Feynman theorem in quantum mechanics, and it is a key element in the inverse unit-cell design problem, since, by specifying the left-hand-side of (4.10), it is possible to invert for the unit-cell properties associated with the eigenpair $(\mathbf{u}, k)$ that appears on the right-hand-side of (4.10). If, for example, it is of interest to realize a

band gap along any particular direction $\mathbf{d}$, then the directional group velocity must vanish [22], i.e.,

$$v_g = 0, \quad \forall\, \omega \in \mathcal{G}, \tag{4.12}$$

or, equivalently, by virtue of (4.10):

$$a_1\left(\mathbf{u}, \mathbf{u}\right) + 2\mathrm{Re}\left\{k\right\} a_2\left(\mathbf{u}, \mathbf{u}\right) = 0. \tag{4.13}$$

We note that the group velocity is defined with respect to the Floquet-Bloch wavevector corresponding to the ansatz (4.4), which differs from the usual definition for plane waves, and obscures the physical interpretation of the group velocity. However, as it is shown below, for propagating states, the group velocity is identical to the energy velocity, i.e.,

$$v_g = v_e, \quad \forall\, \omega \notin \mathcal{G} \tag{4.14}$$

The energy velocity $\mathbf{v}_e$ for a time-harmonic elastic wave is defined as [34, 60]:

$$\mathbf{v}_e = \frac{\mathrm{Re}\left\{\langle \mathbf{F} \rangle\right\}}{\langle \mathcal{E} \rangle}, \tag{4.15}$$

where $\langle\ \rangle$ denotes spatial average, $\mathbf{F}$ is the time-averaged Umov-Poynting vector, and $\mathcal{E}$ is time-averaged energy [60]. The time-averaged Umov-Poynting vector $\mathbf{F}$ and time-averaged energy $\mathcal{E}$ (assuming an $e^{-\mathrm{i}\omega t}$ harmonic factor) are defined as:

$$\mathbf{F} = -\frac{1}{2}\underline{\boldsymbol{\tau}}^{\intercal}\overline{(-\mathrm{i}\omega)\,\mathbf{U}}, \quad \text{and} \tag{4.16}$$

$$\mathcal{E} = U + K = \frac{1}{4}\mathrm{Re}\left\{\overline{\underline{\boldsymbol{\varepsilon}}} : \underline{\boldsymbol{\tau}}\right\} + \frac{1}{4}\rho\overline{(-\mathrm{i}\omega)\,\mathbf{U}} \cdot (-\mathrm{i}\omega)\,\mathbf{U}, \tag{4.17}$$

where U is time-averaged strain energy, K is time-averaged kinetic energy, $\underline{\boldsymbol{\tau}}$ is a stress tensor, $\underline{\boldsymbol{\varepsilon}}$ is a strain tensor. Then, the time-averaged Umov-Poynting vector in the direction $\mathbf{d}$ is:

$$\begin{aligned}
\mathbf{F}\cdot\mathbf{d} &= -\frac{1}{2}\left(\underline{\boldsymbol{\tau}}^{\intercal}\overline{(-\mathrm{i}\omega)\,\mathbf{U}}\right)\cdot\mathbf{d} \\
&= -\frac{1}{2}\underline{\boldsymbol{\tau}} : \left(\overline{(-\mathrm{i}\omega)\,\mathbf{U}}\otimes\mathbf{d}\right) \\
&= -\frac{1}{2}\underline{\underline{\mathbf{C}}}\left[\operatorname{grad}\mathbf{U}\right] : \left(\mathrm{i}\omega\overline{\mathbf{U}}\otimes\mathbf{d}\right) \\
&= -\frac{1}{2}\underline{\underline{\mathbf{C}}}\left[\operatorname{grad}\mathbf{u}+\mathbf{u}\otimes\mathrm{i}\mathbf{k}\right]e^{\mathrm{i}\mathbf{k}\cdot\boldsymbol{x}} : \left(\mathrm{i}\omega\overline{\mathbf{u}}e^{-\mathrm{i}\mathbf{k}\cdot\boldsymbol{x}}\otimes\mathbf{d}\right) \\
&= -\frac{1}{2}\omega\mathrm{i}\left(\overline{\mathbf{u}}\otimes\mathbf{d}\right) : \underline{\underline{\mathbf{C}}}\left[\operatorname{grad}\mathbf{u}\right] + \frac{1}{2}\omega k\left(\overline{\mathbf{u}}\otimes\mathbf{d}\right) : \underline{\underline{\mathbf{C}}}\left[\mathbf{u}\otimes\mathbf{d}\right]. \qquad (4.18)
\end{aligned}$$

In the above, the identity $(\underline{\mathbf{A}}^{\intercal}\mathbf{a})\cdot\mathbf{b} = \operatorname{tr}(\underline{\mathbf{A}}^{\intercal}\mathbf{a}\otimes\mathbf{b}) = \underline{\mathbf{A}} : (\mathbf{a}\otimes\mathbf{b})$ is used [25]. Taking the spatial average of the real part of (4.18), yields:

$$\begin{aligned}
|\Omega_{\mathrm{cell}}|\,\mathrm{Re}\left\{\langle\mathbf{F}\cdot\mathbf{d}\rangle\right\} &= \frac{1}{2}\omega\mathrm{Re}\left\{-\mathrm{i}\int_{\Omega_{\mathrm{cell}}}\left(\overline{\mathbf{u}}\otimes\mathbf{d}\right) : \underline{\underline{\mathbf{C}}}\left[\operatorname{grad}\mathbf{u}\right]d\Omega\right\} \\
&\quad + \frac{1}{2}\omega\mathrm{Re}\left\{k\int_{\Omega_{\mathrm{cell}}}\left(\overline{\mathbf{u}}\otimes\mathbf{d}\right) : \underline{\underline{\mathbf{C}}}\left[\mathbf{u}\otimes\mathbf{d}\right]d\Omega\right\} \\
&= \frac{1}{4}\omega\mathrm{Re}\left\{\mathrm{i}\int_{\Omega_{\mathrm{cell}}}\left\{\underline{\underline{\mathbf{C}}}\left[\operatorname{grad}\overline{\mathbf{u}}\right] : \left(\mathbf{u}\otimes\mathbf{d}\right)\right.\right. \\
&\quad \left.\left. - \left(\overline{\mathbf{u}}\otimes\mathbf{d}\right) : \underline{\underline{\mathbf{C}}}\left[\operatorname{grad}\mathbf{u}\right]\right\}d\Omega\right\} \\
&\quad + \frac{1}{2}\omega\mathrm{Re}\left\{k\int_{\Omega_{\mathrm{cell}}}\left(\overline{\mathbf{u}}\otimes\mathbf{d}\right) : \underline{\underline{\mathbf{C}}}\left[\mathbf{u}\otimes\mathbf{d}\right]d\Omega\right\} \\
&= \frac{1}{4}\omega\left[a_1\left(\mathbf{u},\mathbf{u}\right) + 2\mathrm{Re}\left\{k\right\}a_2\left(\mathbf{u},\mathbf{u}\right)\right], \qquad (4.19)
\end{aligned}$$

where $|\Omega_{\mathrm{cell}}|$ is the area of the unit cell. Next, we compute the time-averaged

energy by

$$\begin{aligned}
\mathcal{E} &= U + K \\
&= \frac{1}{4}\mathrm{Re}\left\{\underline{\boldsymbol{\tau}} : \overline{\underline{\boldsymbol{\varepsilon}}}\right\} + \frac{1}{4}\rho\left(-\mathrm{i}\omega\right)\mathbf{U}\cdot\overline{\left(-\mathrm{i}\omega\right)\mathbf{U}} \\
&= \frac{1}{4}\mathrm{Re}\left\{\underline{\underline{\mathbf{C}}}\left[\mathrm{grad}\,\mathbf{U}\right] : \overline{\mathrm{grad}\,\mathbf{U}}\right\} + \frac{1}{4}\rho\,\omega^2\mathbf{U}\cdot\overline{\mathbf{U}} \\
&= \frac{1}{4}\mathrm{Re}\left\{\underline{\underline{\mathbf{C}}}\left[\mathrm{grad}\,\mathbf{u} + \mathbf{u}\otimes\mathrm{i}\mathbf{k}\right] : \left(\mathrm{grad}\,\overline{\mathbf{u}} - \overline{\mathbf{u}}\otimes\mathrm{i}\mathbf{k}\right)\right\} + \frac{1}{4}\rho\,\omega^2\mathbf{u}\cdot\overline{\mathbf{u}} \\
&= \frac{1}{4}\mathrm{Re}\left\{\mathrm{grad}\,\overline{\mathbf{u}} : \underline{\underline{\mathbf{C}}}\left[\mathrm{grad}\,\mathbf{u}\right]\right\} \\
&\quad + \frac{1}{4}\mathrm{Re}\left\{k\mathrm{i}\left(\mathrm{grad}\,\overline{\mathbf{u}} : \underline{\underline{\mathbf{C}}}\left[\mathbf{u}\otimes\mathbf{d}\right] - \left(\overline{\mathbf{u}}\otimes\mathbf{d}\right) : \underline{\underline{\mathbf{C}}}\left[\mathrm{grad}\,\mathbf{u}\right]\right)\right\} \\
&\quad + \frac{1}{4}\mathrm{Re}\left\{k^2\left(\overline{\mathbf{u}}\otimes\mathbf{d}\right) : \underline{\underline{\mathbf{C}}}\left[\mathbf{u}\otimes\mathbf{d}\right]\right\} + \frac{1}{4}\rho\,\omega^2\mathbf{u}\cdot\overline{\mathbf{u}}. \qquad (4.20)
\end{aligned}$$

The energy's spatial average reads:

$$\begin{aligned}
\left|\Omega_{\mathrm{cell}}\right|\left\langle\mathcal{E}\right\rangle &= \frac{1}{4}\mathrm{Re}\left\{\int_{\Omega_{\mathrm{cell}}}\mathrm{grad}\,\overline{\mathbf{u}} : \underline{\underline{\mathbf{C}}}\left[\mathrm{grad}\,\mathbf{u}\right]d\Omega\right\} \\
&\quad + \frac{1}{4}\mathrm{Re}\left\{k\int_{\Omega_{\mathrm{cell}}}\mathrm{i}\left\{\mathrm{grad}\,\overline{\mathbf{u}} : \underline{\underline{\mathbf{C}}}\left[\mathbf{u}\otimes\mathbf{d}\right] - \left(\overline{\mathbf{u}}\otimes\mathbf{d}\right) : \underline{\underline{\mathbf{C}}}\left[\mathrm{grad}\,\mathbf{u}\right]\right\}d\Omega\right\} \\
&\quad + \frac{1}{4}\mathrm{Re}\left\{k^2\int_{\Omega_{\mathrm{cell}}}\left(\overline{\mathbf{u}}\otimes\mathbf{d}\right) : \underline{\underline{\mathbf{C}}}\left[\mathbf{u}\otimes\mathbf{d}\right]d\Omega\right\} + \frac{1}{4}\int_{\Omega_{\mathrm{cell}}}\rho\,\omega^2\mathbf{u}\cdot\overline{\mathbf{u}}d\Omega \\
&= \frac{1}{4}\mathrm{Re}\left\{P\left(k\right)\left(\mathbf{u},\mathbf{u}\right)\right\} + \frac{1}{2}\int_{\Omega_{\mathrm{cell}}}\rho\,\omega^2\mathbf{u}\cdot\overline{\mathbf{u}}d\Omega \\
&= -\frac{1}{2}\omega^2 a_{0,2}\left(\mathbf{u},\mathbf{u}\right). \qquad (4.21)
\end{aligned}$$

Substituting (4.19) and (4.21) into (4.15), yields

$$v_e = \frac{\mathrm{Re}\left\{\left\langle\mathbf{F}\cdot\mathbf{d}\right\rangle\right\}}{\left\langle\mathcal{E}\right\rangle} = -\frac{a_1\left(\mathbf{u},\mathbf{u}\right) + 2\mathrm{Re}\left\{k\right\}a_2\left(\mathbf{u},\mathbf{u}\right)}{2\,\omega\,a_{0,2}\left(\mathbf{u},\mathbf{u}\right)}, \quad \omega\notin\mathcal{G}. \qquad (4.22)$$

This completes the proof: equation (4.22) is identical to (4.10) and confirms that the group velocity is, for propagating states, physically identical to the energy velocity.

4.3 The metamaterial unit-cell design

In general, the unit-cell design is driven by a user-defined group velocity profile: this, for example, could drive designs that allow for slow or fast wave regimes at specific frequency ranges. Moreover, for the applications considered herein, a user-defined band gap is tantamount to requiring that the group velocity vanish within the desired frequency range. We describe next the inverse medium framework that would produce the unit-cell's design parameters, when given a target group velocity profile.

4.3.1 Dispersion-constrained inverse problem

The design problem is cast as a dispersion-constrained inverse problem, where the Lagrangian L consists of a misfit objective functional M, and of the dispersion constraint E. Accordingly, it reads: given $v_g^m \in \mathbb{R}$, find $\rho \in \mathcal{W}$, $\lambda \in \mathcal{W}$, and $\mu \in \mathcal{W}$ such that

$$\min L\left[\mathbf{u}, k, \mathbf{v}, \xi, \rho, \lambda, \mu\right], \tag{4.23}$$

where,

$$L\left[\mathbf{u},k,\mathbf{v},\xi,\rho,\lambda,\mu\right]=M\left[\mathbf{u},k,\rho,\lambda,\mu\right]+E\left[\mathbf{u},k,\mathbf{v},\xi,\rho,\lambda,\mu\right], \tag{4.24a}$$

$$M\left[\mathbf{u},k,\rho,\lambda,\mu\right]=\sum_{\alpha}^{N_{\text{freq}}}\sum_{\beta}^{N_{\text{dir}}}\sum_{\gamma}^{N_{\text{mode}}}\frac{1}{2}\left(v_{g,\alpha\beta\gamma}-v_{g,\alpha\beta\gamma}^{m}\right)^{2}, \tag{4.24b}$$

$$\begin{aligned}E\left[\mathbf{u},k,\mathbf{v},\xi,\rho,\lambda,\mu\right]=&\sum_{\alpha}^{N_{\text{freq}}}\sum_{\beta}^{N_{\text{dir}}}\sum_{\gamma}^{N_{\text{mode}}}\text{Re}\left\{P\left(k\right)\left(\mathbf{v},\mathbf{u}\right)\right\}_{\alpha\beta\gamma}\\&+\sum_{\alpha}^{N_{\text{freq}}}\sum_{\beta}^{N_{\text{dir}}}\sum_{\gamma}^{N_{\text{mode}}}\left[\frac{\xi}{2}\left\{a_{2}\left(\mathbf{u},\mathbf{u}\right)-1\right\}\right]_{\alpha\beta\gamma},\quad\text{and}\end{aligned} \tag{4.24c}$$

$$\begin{aligned}\mathcal{W}=\Bigg\{&w\in H^{0}\left(\Omega_{\text{cell}}\right)\,|\,w\left(\boldsymbol{x}\right)=w\left(\boldsymbol{x}+\sum_{i=1}^{N_{\text{d}}}m_{i}\mathbf{p}_{i}\right)\\&\forall\boldsymbol{x}\in\partial\Omega_{\text{cell}}\Bigg\}.\end{aligned} \tag{4.24d}$$

In the above, M is an objective functional defined as the misfit between the target (v_g^m) and the trial (v_g) group velocities, where the latter are computed based on trial unit-cell design parameters. In addition, E is the dispersion constraint, side-imposed in (4.24a) in terms of the Floquet-Block EP $P(k)$ of (4.5) and the corresponding orthonormality condition for the eigenfunctions $\mathbf{u}$; $\mathbf{v}$ is the adjoint eigenfunction, and ξ is the adjoint eigenvalue. We note that N_{freq} is the set of the discrete frequencies spanning the target band gap $\mathcal{G}$, N_{dir} are the user-defined directions along which the propagating waves will be band-gaped, and N_{mode} is the number of modes. For an omnidirectional band gap, the set of directions N_{dir} must cover the entire IBZ, or, at a minimum contain all the high-symmetry lines. It should be noted that for each frequency, direction, and mode, a separate EP arises, and thus, the dispersion

constraint E consists of $N_{\text{freq}} \times N_{\text{dir}} \times N_{\text{mode}}$ eigenvalue problems: this explains the triple $\alpha\beta\gamma$ subscripting of the EP in (4.24b), and of the computed $v_{g,\alpha\beta\gamma}$ and prescribed $v^m_{g,\alpha\beta\gamma}$ group velocities, respectively; however, henceforth, we drop the subscripting to reduce notational congestion.

4.3.2 Solution method

We seek solutions for the design variables of the unconstrained minimization problem (4.23) by requiring that the first-order optimality conditions be satisfied, i.e., by setting to zero the first-order derivatives of the Lagrangian $(M + E)$ with respect to the state variables ($\mathbf{u}$ and k), adjoint variables ($\mathbf{v}$ and ξ), and design variables (λ, μ, and ρ). The process is iterative: first, we choose a trial solution for the triad of the design variables; then, the derivative of L with respect to the adjoint variables $\mathbf{v}$ and ξ, yields:

State problem: given $\rho \in \mathcal{W}$, $\lambda \in \mathcal{W}$, and $\mu \in \mathcal{W}$, find $\mathbf{u} \in \mathcal{V}^{N_{\text{d}}} \setminus \{\mathbf{0}\}$ and $k \in \mathbb{C}$ such that

$$P(k)(\tilde{\mathbf{v}}, \mathbf{u}) = 0 \quad \forall \tilde{\mathbf{v}} \in \mathcal{V}^{N_{\text{d}}} \quad \text{and} \tag{4.25a}$$

$$\frac{\tilde{\xi}}{2}\{a_2(\mathbf{u}, \mathbf{u}) - 1\} = 0 \quad \forall \tilde{\xi} \in \mathbb{R}. \tag{4.25b}$$

Next, we take derivatives of L with respect to the state variables $\mathbf{u}$ and k, which results in the

Adjoint problem: given the solutions to the state problem $\mathbf{u} \in \mathcal{V}^{N_{\text{d}}} \setminus \{\mathbf{0}\}$, and $k \in \mathbb{C}$, and the triad of trial design variables $\rho \in \mathcal{W}$, $\lambda \in \mathcal{W}$, and $\mu \in \mathcal{W}$, find

$\mathbf{v} \in \mathcal{V}^{N_\mathrm{d}}$ and $\xi \in \mathbb{R}$ such that

$$P(k)(\mathbf{v}, \tilde{\mathbf{u}}) + \xi a_2(\mathbf{u}, \tilde{\mathbf{u}}) = \frac{a_1(\mathbf{u}, \tilde{\mathbf{u}}) + 2\mathrm{Re}\{k\} a_2(\mathbf{u}, \tilde{\mathbf{u}})}{\omega a_{0,2}(\mathbf{u}, \mathbf{u})} \left(v_g - v_g^m\right) - \frac{a_1(\mathbf{u}, \mathbf{u}) + 2\mathrm{Re}\{k\} a_2(\mathbf{u}, \mathbf{u})}{\omega \left[a_{0,2}(\mathbf{u}, \mathbf{u})\right]^2} a_{0,2}(\mathbf{u}, \tilde{\mathbf{u}}) \left(v_g - v_g^m\right) \quad \forall \tilde{\mathbf{u}} \in \mathcal{V}^{N_\mathrm{d}} \quad \text{and} \quad (4.26a)$$

$$\tilde{k} a_1(\mathbf{v}, \mathbf{u}) + 2k\tilde{k} a_2(\mathbf{v}, \mathbf{u}) = \frac{\tilde{k} a_2(\mathbf{u}, \mathbf{u})}{\omega a_{0,2}(\mathbf{u}, \mathbf{u})} \left(v_g - v_g^m\right) \quad \forall \tilde{k} \in \mathbb{C}. \quad (4.26b)$$

Finally, given the state and adjoint solutions, we take derivatives of L with respect to the design variables ρ, λ, and μ to obtain the gradients g_ρ, g_λ, and g_μ, respectively, i.e.,

Gradient of L: given $\mathbf{v} \in \mathcal{V}^{N_\mathrm{d}}$, $\xi \in \mathbb{R}$, $\mathbf{u} \in \mathcal{V}^{N_\mathrm{d}} \setminus \{\mathbf{0}\}$, $k \in \mathbb{C}$, $\rho \in \mathcal{W}$, $\lambda \in \mathcal{W}$, and $\mu \in \mathcal{W}$, there result:

$$\int_{\Omega_\mathrm{cell}} \tilde{\rho} g_\rho d\Omega = \sum_{\alpha}^{N_\mathrm{freq}} \sum_{\beta}^{N_\mathrm{dir}} \sum_{\gamma}^{N_\mathrm{mode}} \left(\frac{a_1(\mathbf{u}, \mathbf{u}) + 2\mathrm{Re}\{k\} a_2(\mathbf{u}, \mathbf{u})}{2\omega \left[a_{0,2}(\mathbf{u}, \mathbf{u})\right]^2} \right) \left(- \int_{\Omega_\mathrm{cell}} \overline{\mathbf{u}} \cdot \tilde{\rho} \mathbf{u} d\Omega \right) \left(v_g - v_g^m\right) + \sum_{\alpha}^{N_\mathrm{freq}} \sum_{\beta}^{N_\mathrm{dir}} \sum_{\gamma}^{N_\mathrm{mode}} \mathrm{Re} \left\{ - \int_{\Omega_\mathrm{cell}} \overline{\mathbf{v}} \cdot \tilde{\rho} \omega^2 \mathbf{u} d\Omega \right\} \quad \forall \tilde{\rho} \in \mathcal{W}, \quad (4.27a)$$

$$\int_{\Omega_{\text{cell}}} \tilde{\lambda} g_\lambda d\Omega = \sum_{\alpha}^{N_{\text{freq}}} \sum_{\beta}^{N_{\text{dir}}} \sum_{\gamma}^{N_{\text{mode}}}$$

$$\left(-\frac{\mathrm{i} \int_{\Omega_{\text{cell}}} \left\{ \text{grad}\, \overline{\mathbf{u}} : \delta_\lambda \underline{\underline{\mathbf{C}}} \left[\mathbf{u} \otimes \mathbf{d} \right] - \left(\overline{\mathbf{u}} \otimes \mathbf{d} \right) : \delta_\lambda \underline{\underline{\mathbf{C}}} \left[\text{grad}\, \mathbf{u} \right] \right\} d\Omega}{2\, \omega\, a_{0,2} \left(\mathbf{u}, \mathbf{u} \right)} \right.$$

$$\left. -\frac{2\text{Re} \left\{ k \right\} \int_{\Omega_{\text{cell}}} \left(\overline{\mathbf{u}} \otimes \mathbf{d} \right) : \delta_\lambda \underline{\underline{\mathbf{C}}} \left[\mathbf{u} \otimes \mathbf{d} \right] d\Omega}{2\, \omega\, a_{0,2} \left(\mathbf{u}, \mathbf{u} \right)} \right) \left(v_g - v_g^m \right)$$

$$+ \sum_{\alpha}^{N_{\text{freq}}} \sum_{\beta}^{N_{\text{dir}}} \sum_{\gamma}^{N_{\text{mode}}} \text{Re} \left\{ \int_{\Omega_{\text{cell}}} \text{grad}\, \overline{\mathbf{v}} : \delta_\lambda \underline{\underline{\mathbf{C}}} \left[\text{grad}\, \mathbf{u} \right] d\Omega \right\}$$

$$+ \sum_{\alpha}^{N_{\text{freq}}} \sum_{\beta}^{N_{\text{dir}}} \sum_{\gamma}^{N_{\text{mode}}} \text{Re} \left\{ \mathrm{i}k \int_{\Omega_{\text{cell}}} \left\{ \text{grad}\, \overline{\mathbf{v}} : \delta_\lambda \underline{\underline{\mathbf{C}}} \left[\mathbf{u} \otimes \mathbf{d} \right] \right. \right.$$

$$\left. \left. - \left(\overline{\mathbf{v}} \otimes \mathbf{d} \right) : \delta_\lambda \underline{\underline{\mathbf{C}}} \left[\text{grad}\, \mathbf{u} \right] \right\} d\Omega \right\}$$

$$+ \sum_{\alpha}^{N_{\text{freq}}} \sum_{\beta}^{N_{\text{dir}}} \sum_{\gamma}^{N_{\text{mode}}} \text{Re} \left\{ k^2 \int_{\Omega_{\text{cell}}} \left(\overline{\mathbf{v}} \otimes \mathbf{d} \right) : \delta_\lambda \underline{\underline{\mathbf{C}}} \left[\mathbf{u} \otimes \mathbf{d} \right] d\Omega \right\}$$

$$+ \sum_{\alpha}^{N_{\text{freq}}} \sum_{\beta}^{N_{\text{dir}}} \sum_{\gamma}^{N_{\text{mode}}} \text{Re} \left\{ \frac{\xi}{2} \int_{\Omega_{\text{cell}}} \left(\overline{\mathbf{v}} \otimes \mathbf{d} \right) : \delta_\lambda \underline{\underline{\mathbf{C}}} \left[\mathbf{u} \otimes \mathbf{d} \right] d\Omega \right\}$$

$$\forall \tilde{\lambda} \in \mathcal{W}, \quad \text{and} \qquad (4.27b)$$

$$\int_{\Omega_{\text{cell}}} \tilde{\mu} g_\mu d\Omega = \sum_{\alpha}^{N_{\text{freq}}} \sum_{\beta}^{N_{\text{dir}}} \sum_{\gamma}^{N_{\text{mode}}}$$
$$\left(-\frac{\mathrm{i} \int_{\Omega_{\text{cell}}} \left\{ \operatorname{grad} \overline{\mathbf{u}} : \delta_\mu \underline{\underline{\mathbf{C}}} \left[\mathbf{u} \otimes \mathbf{d} \right] - \left(\overline{\mathbf{u}} \otimes \mathbf{d} \right) : \delta_\mu \underline{\underline{\mathbf{C}}} \left[\operatorname{grad} \mathbf{u} \right] \right\} d\Omega}{2\, \omega\, a_{0,2} \left(\mathbf{u}, \mathbf{u} \right)} \right.$$
$$\left. - \frac{2\mathrm{Re} \left\{ k \right\} \int_{\Omega_{\text{cell}}} \left(\overline{\mathbf{u}} \otimes \mathbf{d} \right) : \delta_\mu \underline{\underline{\mathbf{C}}} \left[\mathbf{u} \otimes \mathbf{d} \right] d\Omega}{2\, \omega\, a_{0,2} \left(\mathbf{u}, \mathbf{u} \right)} \right) \left(v_g - v_g^m \right)$$
$$+ \sum_{\alpha}^{N_{\text{freq}}} \sum_{\beta}^{N_{\text{dir}}} \sum_{\gamma}^{N_{\text{mode}}} \mathrm{Re} \left\{ \int_{\Omega_{\text{cell}}} \operatorname{grad} \overline{\mathbf{v}} : \delta_\mu \underline{\underline{\mathbf{C}}} \left[\operatorname{grad} \mathbf{u} \right] d\Omega \right\}$$
$$+ \sum_{\alpha}^{N_{\text{freq}}} \sum_{\beta}^{N_{\text{dir}}} \sum_{\gamma}^{N_{\text{mode}}} \mathrm{Re} \left\{ \mathrm{i}k \int_{\Omega_{\text{cell}}} \left\{ \operatorname{grad} \overline{\mathbf{v}} : \delta_\mu \underline{\underline{\mathbf{C}}} \left[\mathbf{u} \otimes \mathbf{d} \right] \right. \right.$$
$$\left. \left. - \left(\overline{\mathbf{v}} \otimes \mathbf{d} \right) : \delta_\mu \underline{\underline{\mathbf{C}}} \left[\operatorname{grad} \mathbf{u} \right] \right\} d\Omega \right\}$$
$$+ \sum_{\alpha}^{N_{\text{freq}}} \sum_{\beta}^{N_{\text{dir}}} \sum_{\gamma}^{N_{\text{mode}}} \mathrm{Re} \left\{ k^2 \int_{\Omega_{\text{cell}}} \left(\overline{\mathbf{v}} \otimes \mathbf{d} \right) : \delta_\mu \underline{\underline{\mathbf{C}}} \left[\mathbf{u} \otimes \mathbf{d} \right] d\Omega \right\}$$
$$+ \sum_{\alpha}^{N_{\text{freq}}} \sum_{\beta}^{N_{\text{dir}}} \sum_{\gamma}^{N_{\text{mode}}} \mathrm{Re} \left\{ \frac{\xi}{2} \int_{\Omega_{\text{cell}}} \left(\overline{\mathbf{v}} \otimes \mathbf{d} \right) : \delta_\mu \underline{\underline{\mathbf{C}}} \left[\mathbf{u} \otimes \mathbf{d} \right] d\Omega \right\}$$
$$\forall \tilde{\mu} \in \mathcal{W}, \tag{4.27c}$$

where,

$$\delta_\lambda \underline{\underline{\mathbf{C}}} \left[\, \right] = \tilde{\lambda} \operatorname{tr} \left[\, \right] \underline{\mathbf{I}} \quad \text{and} \tag{4.28a}$$

$$\delta_\mu \underline{\underline{\mathbf{C}}} \left[\, \right] = \tilde{\mu} \left[\, \right] + \tilde{\mu} \left[\, \right]^{\mathsf{T}} . \tag{4.28b}$$

The detailed derivations are provided in section 4.7.2. The gradients (4.27) vanish only at a stationary point of the Lagrangian L; they are used, in the context of a conjugate gradient method [49], in order to update the design

variables. The algorithm for the inverse metamaterial design is summarized in Algorithm 3.

Algorithm 3 Inverse design process

1: Sample the target group velocity v_g^m ($v_g^m = 0$ for band gaps) at discrete frequencies, directions, and modes
2: Define the geometry of the unit cell (e.g., periodicity, number of distinct material elements, etc.)
3: Set the error tolerance ε.
4: Initialize the iteration counter $l \leftarrow 0$
5: Set the initial search length
6: Set initial guesses for the material properties ρ_0, λ_0, and μ_0
7: **for** $\|M_{l+1} - M_l\| > \varepsilon \|M_l\|$ **do**
8: Solve the state problem and evaluate M_l ▷ equations (4.24b) and (4.25)
9: Solve the adjoint problem ▷ equation (4.26)
10: Compute the reduced gradient of L ▷ equations (4.27)
11: Obtain the search direction (e.g., conjugate gradient method)
12: Update the material properties ρ_{l+1}, λ_{l+1}, and μ_{l+1} using backtracking algorithm; stop if sufficient-decrease condition is violated
13: Set $l \leftarrow l + 1$
14: **end for**

4.4 Metamaterial band-gap design examples

The proposed design method can invert for a unit cell's properties when provided with a user-defined group velocity profile. In the following examples, we demonstrate the method by inverting for the mass density and the Lamé parameters of multi-material unit cells to effect either uni- or omnidirectional user-defined band gaps. In all cases, we use finite elements (biquadratic serendipity elements) to solve the state and adjoint problems.

4.4.1 An omnidirectional band gap

First, we attempt to invert for the properties of a square unit cell to effect an omnidirectional band gap at $\mathcal{G} = (5, 10)$ Hz. The unit cell consists of three concentric squares of different materials, with sides 4m, 8/3m, and 4/3m, respectively (Fig. 4.3); the properties were seeded to $\rho_1 = 10081.370$ kg/m^3, $\lambda_1 = 63.266$ MPa, $\mu_1 = 33.266$ MPa, for the innermost square, $\rho_2 = 7730.992$ kg/m^3, $\lambda_2 = 41.213$ MPa, $\mu_2 = 21.213$ MPa, for the middle, and $\rho_3 = 73.61$ kg/m^3, $\lambda_3 = 7.443$ MPa, $\mu_3 = 3.843$ MPa for the outermost square.

We use fifty frequencies ($N_{\text{freq}} = 50$) to span $\mathcal{G}$, and ten directions to sweep over the IBZ ($N_{\text{dir}} = 10$) in order to enforce omnidirectional behavior; the number of modes N_{mode} equals the number of wavenumbers within the first Brillouin zone, and, thus, it varies per frequency. The target group velocities for all of the N_{freq} frequencies, the N_{dir} directions, and the N_{mode} modes are set to zero, i.e., $v^m_{g,\alpha\beta\gamma} = 0$. Figure 4.3(a) depicts the unit cell's converged material properties, while Fig. 4.3(b) and Fig. 4.3(c) show the band structure and group velocity profiles along the high-symmetry lines, respectively. As it can be deduced from the band structure the target band gap, shown in the figures with the shaded strip, was indeed realized (to minimize graphical congestion in the band structure, only the real-valued wavenumbers are plotted). Figure 4.4 shows the complete three-dimensional dispersion surfaces in the IBZ (Figure 4.4(a)), and by using graphic mirroring, in the Brillouin zone as well (Figure 4.4(b)): each plane represents a single wavevector computation, the width of which is proportional to the magnitude of the wavevector, and the

slope is guided by the group velocity.

4.4.2 Two omnidirectional band gaps

Next, we exercise the inversion algorithm by seeking a metamaterial that would exhibit simultaneously two user-defined band gaps, that is, $\mathcal{G} = (5, 10)\,\text{Hz} \cup (13, 15)\,\text{Hz}$. We seed the inversion algorithm with the converged properties of the preceding example's unit cell. Figure 4.5(a) shows the converged material profile, while Figs. 4.5(b) and 4.5(c) depict again the corresponding band structure and group velocity profiles, respectively. As it can be seen, the inversion algorithm successfully resulted in opening a second band gap at the target frequency range (13,15) Hz, while still maintaining the first gap at (5,10) Hz. Figure 4.6 shows the metamaterial's three-dimensional dispersion map.

4.4.3 A unidirectional band gap at $(5, 10)$ Hz

Next, we target a unidirectional band gap at $(5, 10)$ Hz along Γ-X only. Figure 4.7 shows that a unidirectional band gap is achieved exactly at the target frequency range. Figure 4.8 shows the three-dimensional dispersion map.

4.5 Metabarrier time-domain performance

The preceding development is predicated upon infinite periodicity, whereas, in practice, one may be able to install only a finite number of unit

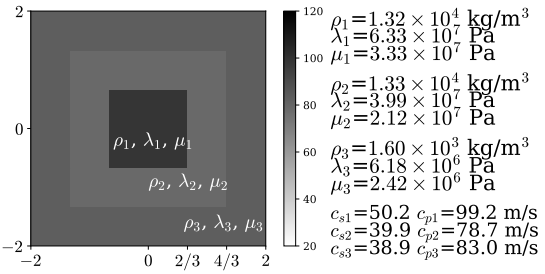

(a) Inverted unit-cell material properties

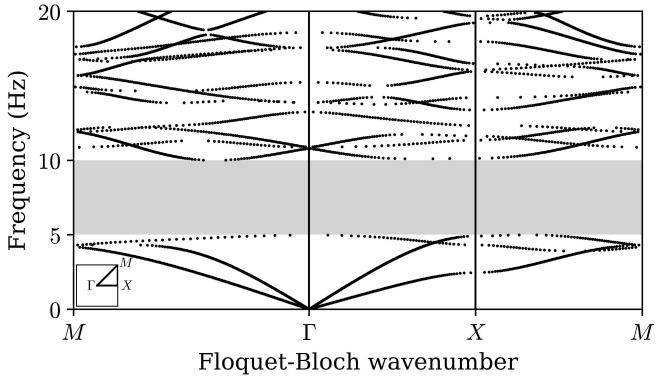

(b) Band structure along the high-symmetry lines

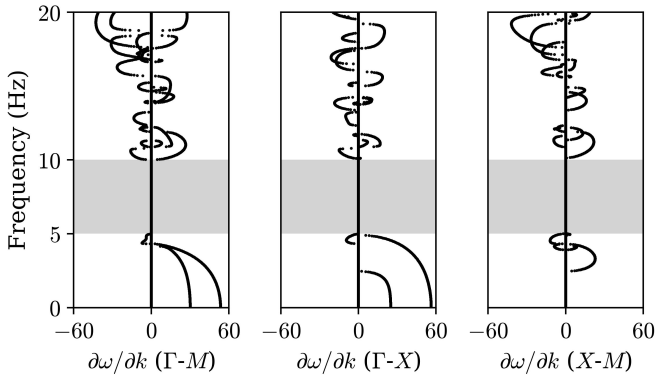

(c) Group velocity along the high-symmetry lines

Figure 4.3: Unit cell design for an omnidirectional band gap at $\mathcal{G} = (5, 10)$ Hz

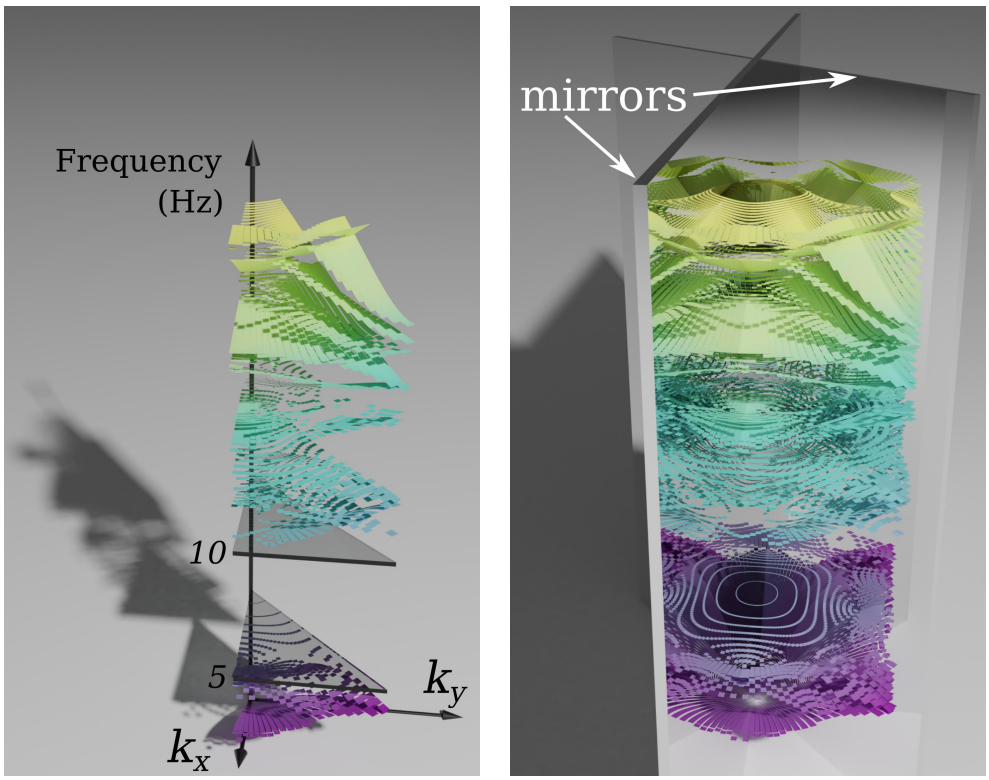

(a) Dispersion surfaces of the irreducible Brillouin zone - IBZ

(b) Dispersion surfaces of the Brillouin zone

Figure 4.4: Band structure showing an omnidirectional target band gap at $\mathcal{G} = (5, 10)$ Hz

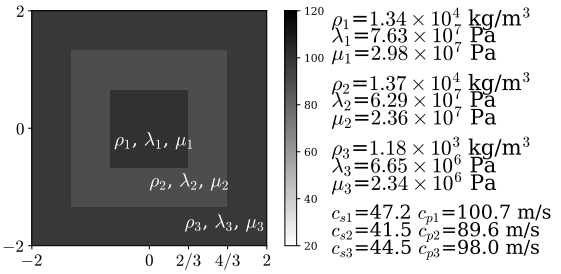

(a) Inverted unit-cell material properties

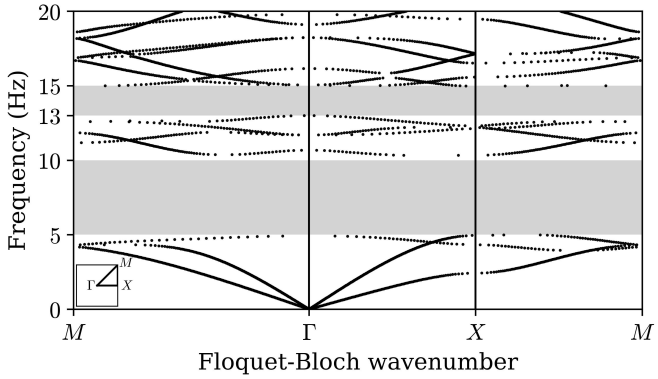

(b) Band structure along the high-symmetry lines

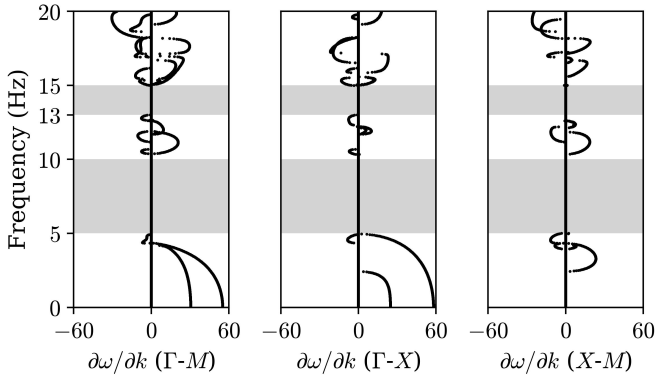

(c) Group velocity along the high-symmetry lines

Figure 4.5: Unit cell design for two omnidirectional band gaps at $\mathcal{G} = (5, 10) \cup (13, 15)$ Hz

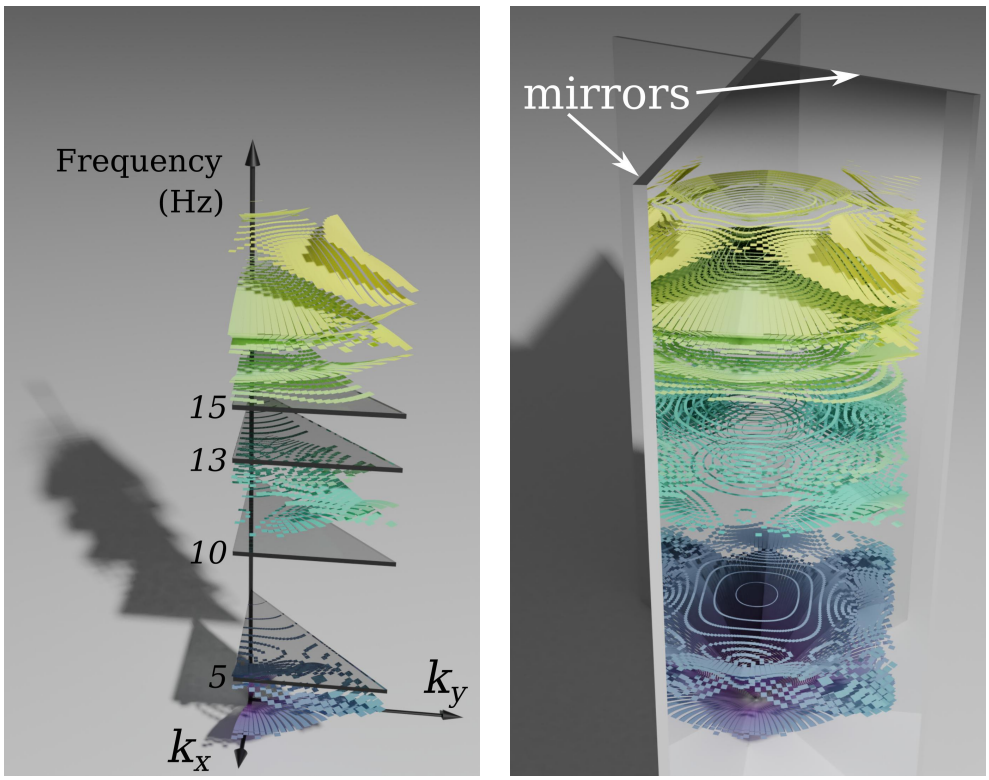

(a) Dispersion surfaces of the irreducible Brillouin zone - IBZ

(b) Dispersion surfaces of the Brillouin zone

Figure 4.6: Band structure showing two omnidirectional band gaps at $\mathcal{G} = (5, 10) \cup (13, 15)$ Hz

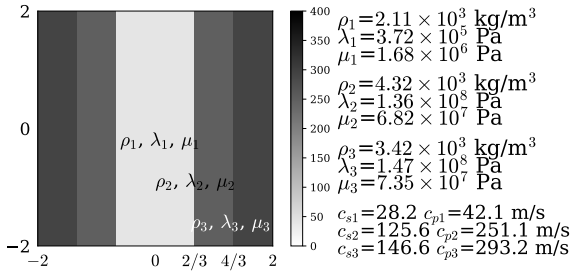

(a) Inverted unit-cell material properties

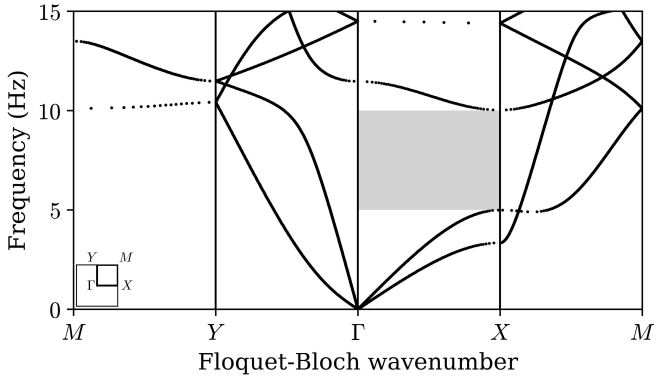

(b) Band structure along the high-symmetry lines

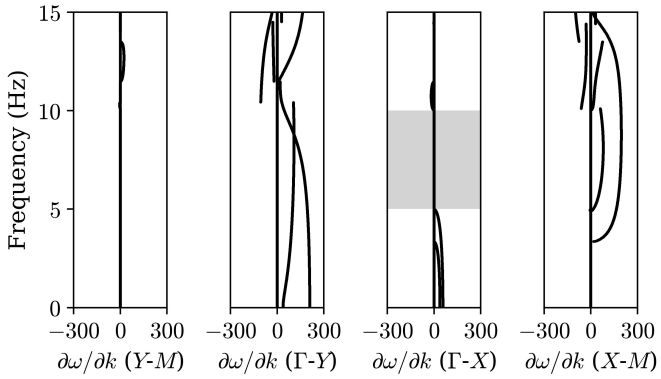

(c) Group velocity along the high-symmetry lines

Figure 4.7: Unit cell design for a unidirectional band gap at $\mathcal{G} = (5, 10)$ Hz

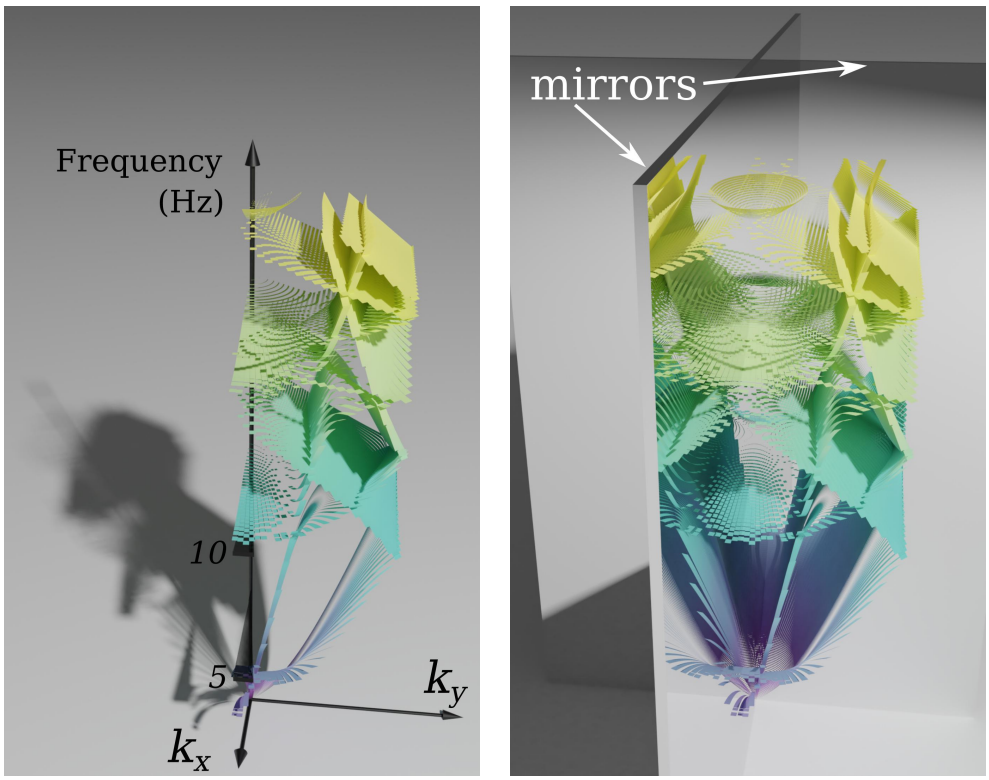

(a) Dispersion surfaces of the irreducible Brillouin zone - IBZ

(b) Dispersion surfaces of the Brillouin zone

Figure 4.8: Band structure showing an unidirectional band gap at $\mathcal{G} = (5, 10)$ Hz

cells in a host medium. In this section, we assess the performance of the unit cells in the time-domain –where it matters most for applications– by using the inverted-for unit cells to construct finite-size metabarriers, where the unit cells appear with a fairly narrow periodicity –only 2- or 4-unit-cell wide. The intent is to study via numerical simulations whether the metabarriers could still realize the directional or omnidirectional band gaps their constituent unit cells were designed for, even when the infinite periodicity assumption is violated.

4.5.1 An omnidirectional P and SV metabarrier

First, we discuss the P and SV omnidirectional band-gap case. As shown in Figure 4.9, a two-unit-cell-wide metabarrier Ω_{m} is embedded within an infinite homogeneous domain, truncated by Perfectly-Matched-Layers (PMLs) [19, 32]. The metabarrier is constructed using the unit cell of the first design example exhibiting a band gap at $\mathcal{G} = (5, 10)$ Hz (Figure 4.3). The host medium's properties are $\rho = 2000$ kg/m^3, $\lambda = 160$ MPa, and $\mu = 80$ MPa. A Ricker pulse with a central frequency of $f_c = 9$ Hz is applied at $(x, y) = (-36, 0)$ m. The point source creates cylindrical wave fronts impinging on the metabarrier at various angles of incidence.

Figures 4.10(a) and (b) depict snapshots of the displacement-field at $t = 0.26$ s for cases without and with the metabarrier, respectively. Visually, it appears that the metabarrier, despite its narrow periodicity, effectively arrested the propagation of the waves past the barrier. Figures 4.10 show the response DFT at two locations past the barrier: the dotted trace corre-

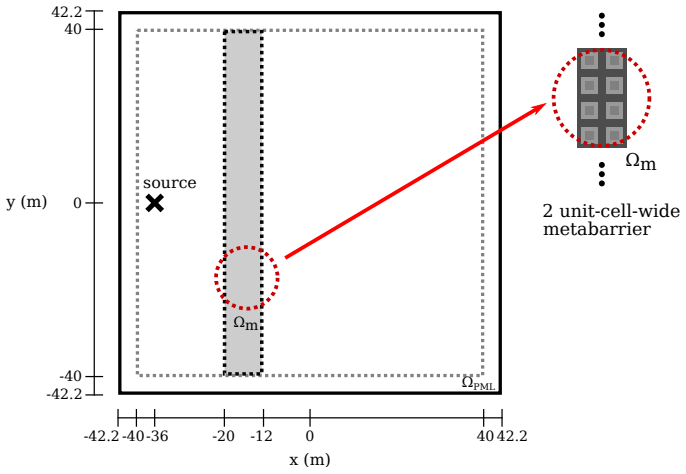

Figure 4.9: Schematic of an omnidirectional P and SV metabarrier

sponds to the case without the metabarrier, whereas the dashed and solid lines correspond to a two-unit-cell-wide and a four-unit-cell-wide metabarriers, respectively. The shaded strip delineates the frequency range of the design band gap: as it can be seen both barriers suppressed the motion at the band gap, as intended. Moreover, notice that even though the suppression is somewhat stronger with the four-unit-cell-wide metabarrier, the difference between the two is relatively small.

4.5.2 An omnidirectional vertical screen

We are interested in assessing whether the same finite-width engineered metabarrier of the preceding example can be used as a vertical screen in a halfspace, when the halfspace is subjected to a surficial line load in the vicinity of the screen. While the unit cell has been engineered for band-gapping P and SV waves, the line load on the halfspace's surface introduces additional waves

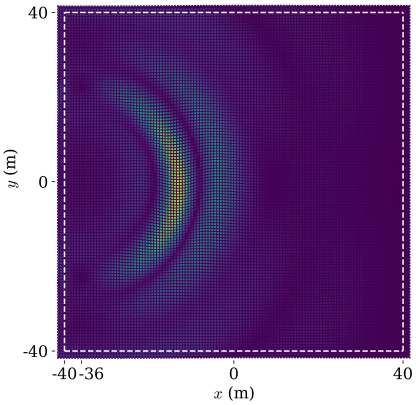

(a) Without metabarrier; snapshot at $t = 0.26$ s

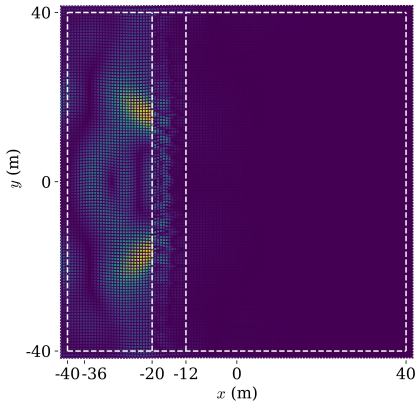

(b) With metabarrier (two-unit-cell-wide); snapshot at $t = 0.26$ s

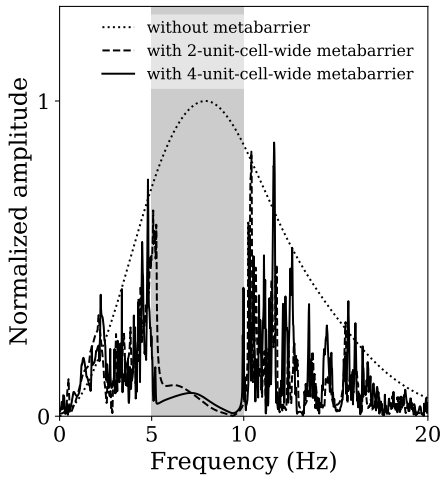

(c) DFT responses at $(x, y) = (0, 0)$ m

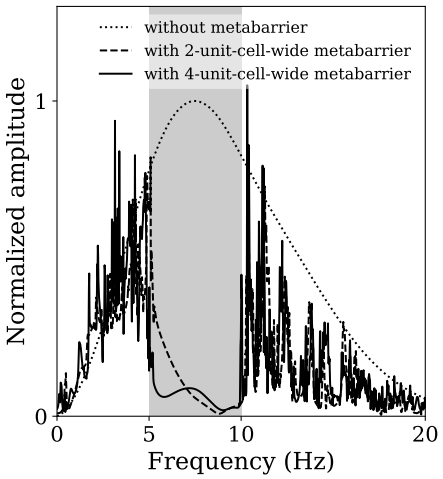

(d) DFT responses at $(x, y) = (0, 22)$ m

Figure 4.10: Omnidirectional metabarrier performance: snapshots and DFT response of wavefields induced by a Ricker pulse with a central frequency of $f_c = 9$ Hz

(Rayleigh, and the S head wave) that were not accounted for in the unit-cell design. Figure 4.11 captures the setting: a two-unit-cell-wide and eleven-unit-cell-long metabarrier is embedded in a two-dimensional semi-infinite domain truncated by PMLs. We use the unit cell of the first design example exhibiting a band gap at $\mathcal{G} = (5, 10)$ Hz to construct the metabarrier/vertical screen. A vertical line load is applied on the surface of the host medium. We visualize the response using waterfall plots, i.e., a horizontal stack of displacement-field snapshots over a time period of $t \in [0, 0.5]$ s.

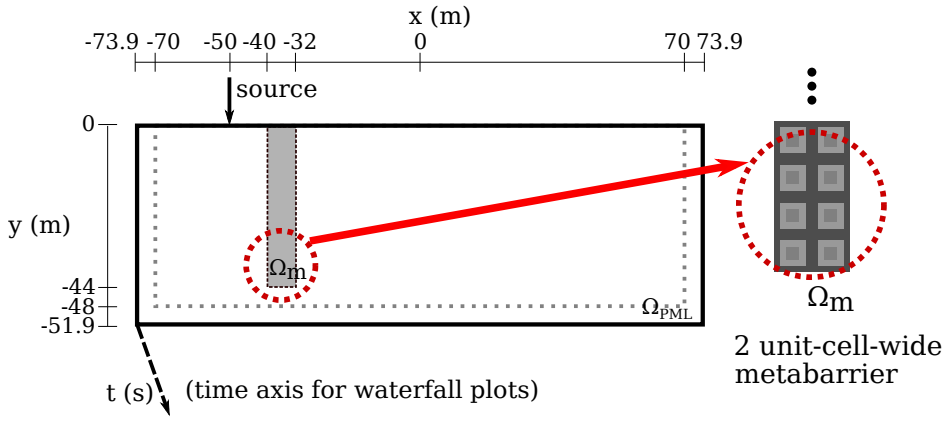

Figure 4.11: Schematic of an omnidirectional vertical screen

Three different signals are used to exercise the screen. A monochromatic source with frequency of $f = 2.5$ Hz is used first: the frequency lies outside of the unit cell's band gap, and, thus, propagation should not be arrested. Indeed, as shown in the waterfalls of Fig. 4.12(a),(b), the wave front propagates unimpeded through the screen, albeit with a phase delay. By contrast, when the monochromatic source operates at 8 Hz, which lies within the

design band gap, the waves are reflected by and/or trapped in the screen, effectively arresting propagation in the forward scatter region of the screen (Fig. 4.12(c),(d)). Next, we apply a Ricker pulse with a central frequency of $f_c = 9$ Hz; the Ricker pulse has a broad spectrum support, roughly between 3 and 27 Hz (three times the central frequency on each side of f_c). Figures 4.12(e),(f) capture the effect of the screen: as it can be seen, it appears that propagation has been arrested, as it was expected for at least the range for which the screen was designed (5 to 10 Hz). To better quantify our observations we compute the DFT of the response at four locations, two in the backscatter region (between the source and the metabarrier), and two in the forward scatter region of the metabarrier. In Fig. 4.13, the top row pertains to two points on the surface of the halfspace, whereas the second row pertains to two points at depth. The shaded strip in the DFT spans the design band gap: as it can be seen from the right column, which corresponds to points in the forward scatter region, the screen, almost perfectly, arrested propagation for frequencies within the gap. The DFT on the left column shows that there is motion amplification in the backscatter region at depth, but not on the surface; however, as shown in [22], introducing small amounts of damping in the screen can reduce the amplification in the backscatter zone.

4.5.3 Wave steering and shielding

Next, we turn to applications that could benefit from an omnidirectional design. First, we consider an infinite two-dimensional domain, which

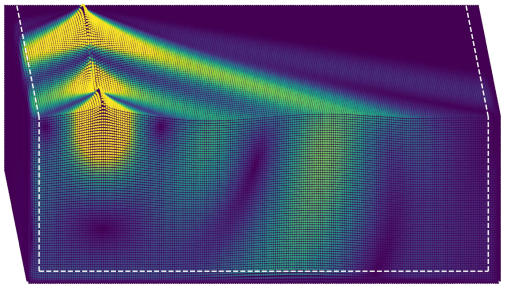

(a) Monochromatic source at $f = 2.5$ Hz $\notin \mathcal{G}$; without metabarrier

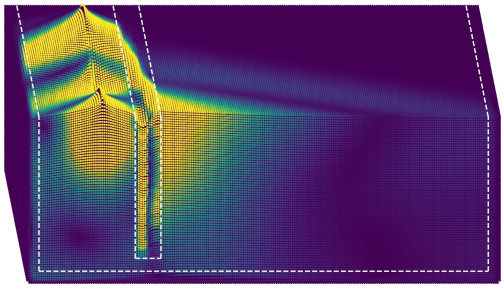

(b) Monochromatic source at $f = 2.5$ Hz $\notin \mathcal{G}$; with metabarrier

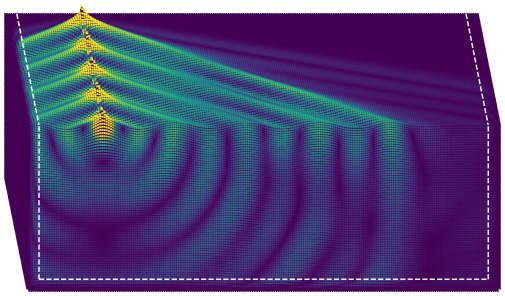

(c) Monochromatic source at $f = 8$ Hz $\in \mathcal{G}$; without metabarrier

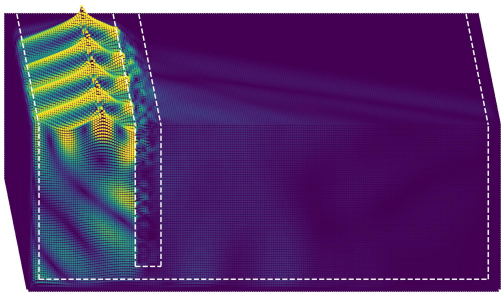

(d) Monochromatic source at $f = 8$ Hz $\in \mathcal{G}$; with metabarrier

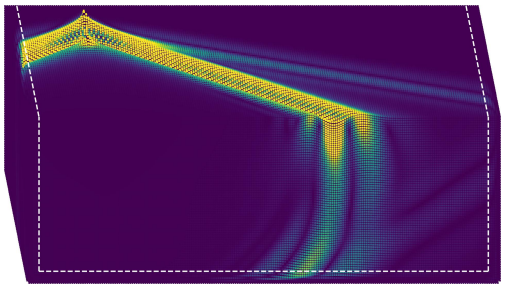

(e) Ricker pulse with $f_c = 9$ Hz; without metabarrier

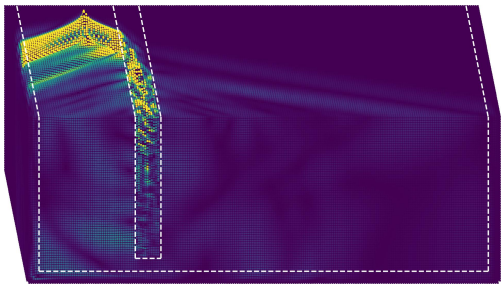

(f) Ricker pulse with $f_c = 9$ Hz; with metabarrier

Figure 4.12: Response of an engineered vertical metabarrier to various excitations

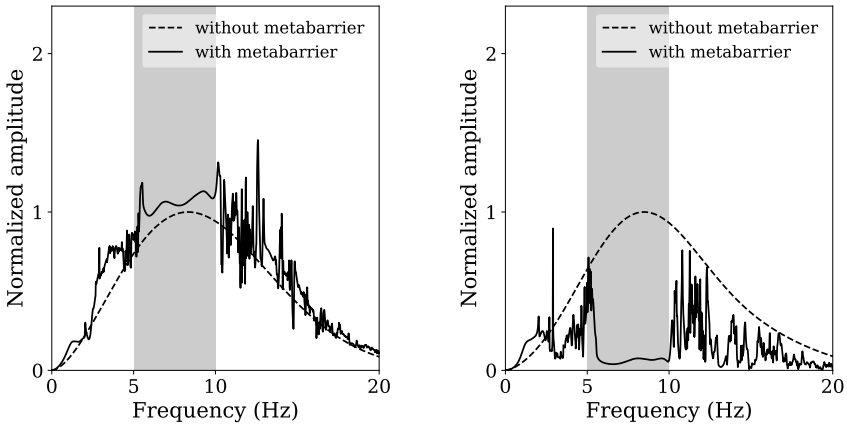

(a) $(x, y) = (-45, 0)$ m (b) $(x, y) = (-27, 0)$ m

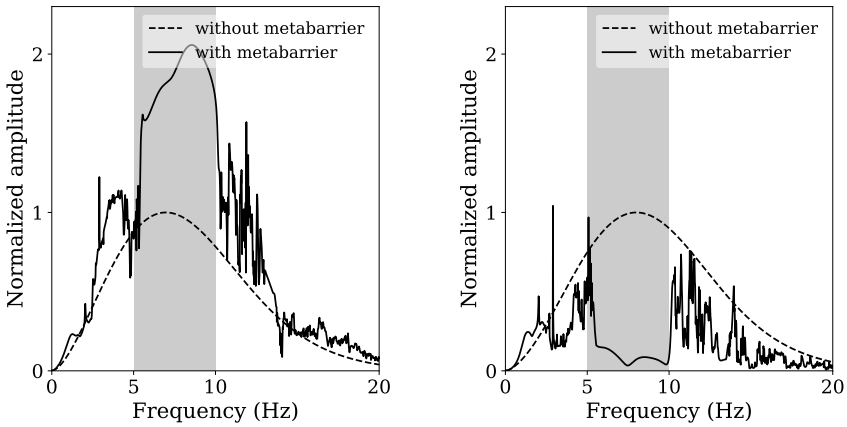

(c) $(x, y) = (-45, -14)$ m (d) $(x, y) = (-27, -14)$ m

Figure 4.13: DFT responses at various locations before (left column) and after (right column) the metabarrier

we truncate to a finite computational domain of 140 m $\times$ 48 m, surrounded on all sides by PMLs. We impregnate the mid half of the domain (80 m $\times$ 48 m) with the engineered unit cells (each cell is 4 m $\times$ 4 m) of the first design example, exhibiting an omnidirectional band gap at $(5, 10)$ Hz. Then, we intentionally modify part of the metastructure, by creating a one-unit-cell-wide channel made of the same material as the infinite domain. We then trigger a point load, located in the exterior of the metastructure and in the vicinity of the channel. The generated waves impinge at various angles on the metastructure: owing to the omnidirectional band gap, the motion in the metastructure is inhibited, allowing the waves to propagate only within the channel, effectively steering the waves through the artificial waveguide. Figure 4.14 shows a snapshot in time of the waveguide effect.

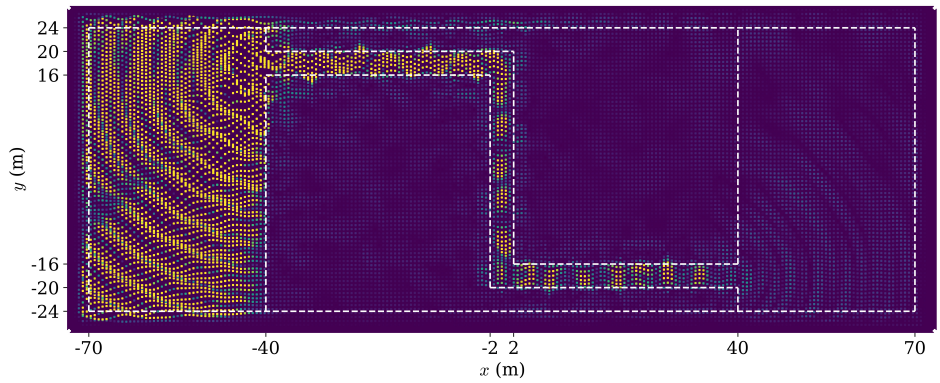

Figure 4.14: Wave steering in a homogeneous medium impregnated with metamaterials

Next, we use again the same unit-cell design, and create a hollow rectangle (Fig. 4.15) of two-unit-cell width. The intent is to examine whether the

interior of the rectangle could be protected/shielded from propagating waves that originate in the exterior of the shield, and impinge, asynchronously, on the shield at various angles. To this end, we place four point sources in the exterior of the shield (Fig. 4.15), which are triggered at different moments in time (Ricker pulses operating at a central frequency of $f_c = 9$ Hz), along different directions. To quantify the response of the shield, and compare it with

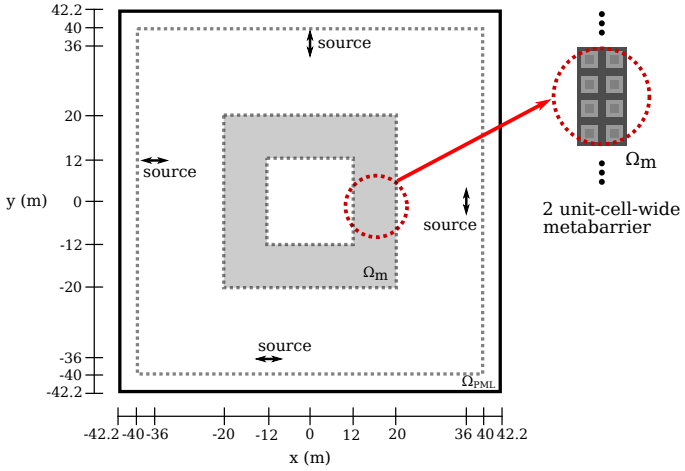

Figure 4.15: Schematic of a wave shield

the unshielded case, we compute the energy density E_{Ω^e}, normalized by the input energy, in order to track energy propagation within the computational domain. To this end, let:

$$E_{\Omega^e} = \frac{\frac{1}{2}\int_0^T \left\{ \int_{\Omega^e} \operatorname{grad} \mathbf{U}_t : \underline{\underline{\mathbf{C}}} \left[\operatorname{grad} \mathbf{U}_t \right] d\Omega + \int_{\Omega^e} \frac{\partial \mathbf{U}_t}{\partial t} \cdot \rho \frac{\partial \mathbf{U}_t}{\partial t} d\Omega \right\} dt}{\frac{1}{2}\int_0^T \int_{\Omega} \mathbf{f} \cdot \mathbf{U}_t \, d\Omega \, dt}, \qquad (4.29)$$

where $\mathbf{U}_t$ is the displacement field in the time-domain, and $\mathbf{f}$ is the source. Figure 4.17 depicts the energy density without and with the shield. We note

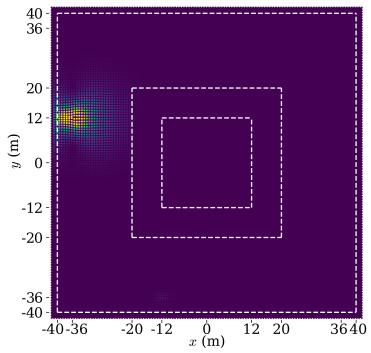

(a) West source triggered; snapshot at $t = 0.0975$ s

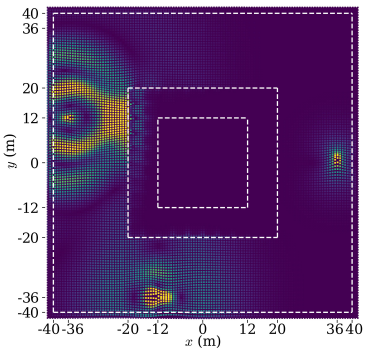

(b) South and east sources triggered; snapshot at $t = 0.1875$ s

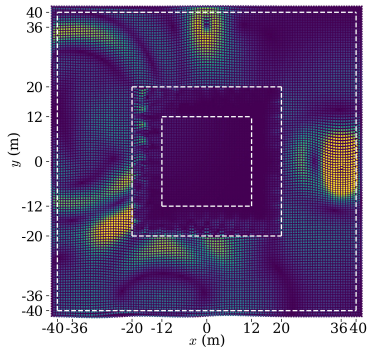

(c) All sources triggered; snapshot at $t = 0.2625$ s

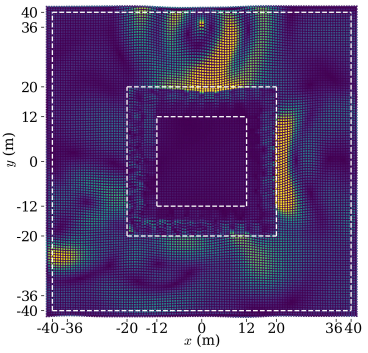

(d) Shield fully engaged; snapshot at $t = 0.3375$ s

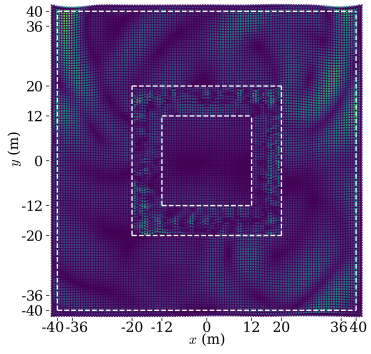

(e) Shield fully engaged; snapshot at $t = 0.4875$ s

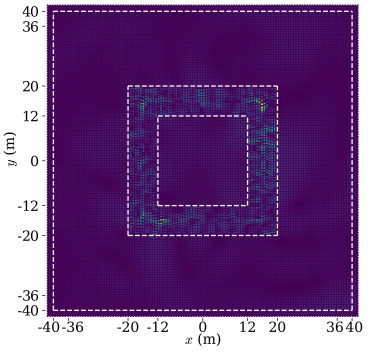

(f) Shield fully engaged; snapshot at $t = 0.8250$ s

Figure 4.16: Snapshots of a wave shield's response to asynchronously triggered sources

the near-silent center section of the domain, attesting to the shielding efficacy of the finite metabarrier, under the asynchronous P and SV wave load impinging on the shield at arbitrary angles.

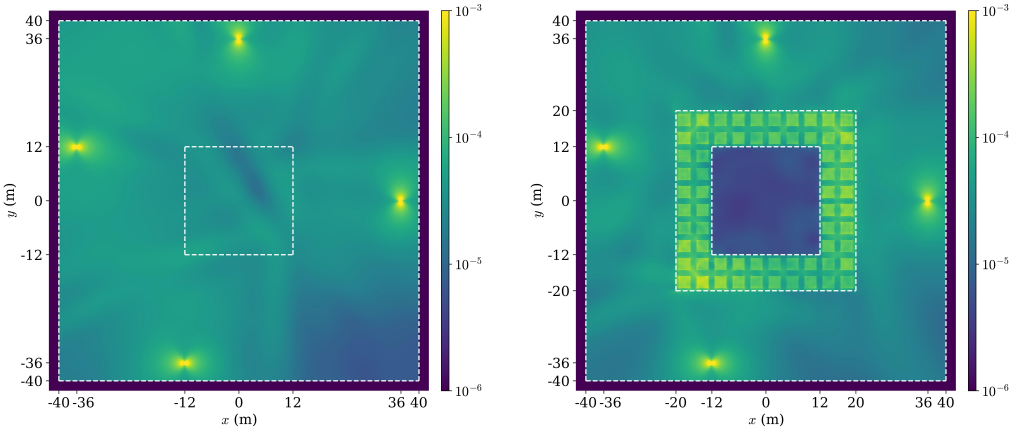

(a) Without the shield

(b) With the shield

Figure 4.17: Normalized energy density distribution due to four point source Ricker pulses operating at $f_c = 9$ Hz

4.6 Conclusions

We proposed a systematic design method for engineering the dispersive properties of periodic media as a means of controlling elastic wave propagation. Specifically, we cast the design problem as a dispersion-constrained inverse problem, comprising: a) a misfit functional between the design group velocity profile and the group velocity profile corresponding to trial design unit-cell variables, and: b) the side-imposition of the unit-cell Floquet-Bloch eigen-

value problem. The group velocity is expressed in terms of an eigenpair, thus readily allowing the use of any standard optimization scheme to resolve the inverse problem. The proposed inverse design framework can handle various unit-cell variables, including geometric and material parameters. We demonstrated the proposed method by designing unit cells exhibiting unidirectional or omnidirectional band gaps at user-specified frequency ranges. The time-domain analyses showed that metabarriers constructed with only a few unit cells, i.e., by severely limiting the periodicity, can still harness the benefits of the engineered unit-cell dispersive behavior. We showed that the developed framework can lead to metamaterial designs capable of band-gapping, wave steering, and shielding, in the presence of both P and SV waves, and, in fact, proved effective even for surface interface waves.

4.7 Appendix

4.7.1 Floquet-Bloch eigenvalue problem with an offset direction

A non-zero offset direction $\mathbf{d}_o$ is required for high-symmetry lines that do not connect to the origin Γ. Decomposing the Floquet-Bloch wavevector as $\mathbf{k} = k\mathbf{d} + \mathbf{d}_o$, the EP (4.5) is rewritten as

Given $\omega \in \mathbb{R}$, $\mathbf{d} \in \mathbb{R}^{N_\mathrm{d}}$, and $\mathbf{d}_o \in \mathbb{R}^{N_\mathrm{d}}$, find $k \in \mathbb{C}$ and $\mathbf{u} \in \mathcal{V}^{N_\mathrm{d}} \setminus \{\mathbf{0}\}$ such that

$$0 = b_0(\mathbf{v}, \mathbf{u}) + k b_1(\mathbf{v}, \mathbf{u}) + k^2 b_2(\mathbf{v}, \mathbf{u}) \quad \forall \mathbf{v} \in \mathcal{V}^{N_\mathrm{d}}, \tag{4.30}$$

where

$$b_0(\mathbf{v},\mathbf{u}) = \int_{\Omega_{\text{cell}}} \left\{\operatorname{grad}\overline{\mathbf{v}} : \underline{\underline{\mathbf{C}}}\left[\operatorname{grad}\mathbf{u}\right] - \overline{\mathbf{v}}\cdot\omega^2\rho\,\mathbf{u}\right\} d\Omega$$
$$+ \mathrm{i}\int_{\Omega_{\text{cell}}} \left\{\operatorname{grad}\overline{\mathbf{v}} : \underline{\underline{\mathbf{C}}}\left[\mathbf{u}\otimes\mathbf{d}_o\right] - \left(\overline{\mathbf{v}}\otimes\mathbf{d}_o\right) : \underline{\underline{\mathbf{C}}}\left[\operatorname{grad}\mathbf{u}\right]\right\} d\Omega$$
$$+ \int_{\Omega_{\text{cell}}} \left(\overline{\mathbf{v}}\otimes\mathbf{d}_o\right) : \underline{\underline{\mathbf{C}}}\left[\mathbf{u}\otimes\mathbf{d}_o\right] d\Omega, \tag{4.31a}$$

$$b_1(\mathbf{v},\mathbf{u}) = \mathrm{i}\int_{\Omega_{\text{cell}}} \left\{\operatorname{grad}\overline{\mathbf{v}} : \underline{\underline{\mathbf{C}}}\left[\mathbf{u}\otimes\mathbf{d}\right] - \left(\overline{\mathbf{v}}\otimes\mathbf{d}\right) : \underline{\underline{\mathbf{C}}}\left[\operatorname{grad}\mathbf{u}\right]\right\} d\Omega$$
$$+ \int_{\Omega_{\text{cell}}} \left\{\left(\overline{\mathbf{v}}\otimes\mathbf{d}\right) : \underline{\underline{\mathbf{C}}}\left[\mathbf{u}\otimes\mathbf{d}_o\right] + \left(\overline{\mathbf{v}}\otimes\mathbf{d}_o\right) : \underline{\underline{\mathbf{C}}}\left[\mathbf{u}\otimes\mathbf{d}\right]\right\} d\Omega, \quad \text{and} \tag{4.31b}$$

$$b_2(\mathbf{v},\mathbf{u}) = \int_{\Omega_{\text{cell}}} \left(\overline{\mathbf{v}}\otimes\mathbf{d}\right) : \underline{\underline{\mathbf{C}}}\left[\mathbf{u}\otimes\mathbf{d}\right] d\Omega. \tag{4.31c}$$

For example, the directions for a two-dimensional square Brillouin zone are $\mathbf{d} = (1,0)$ and $\mathbf{d}_o = (0,0)$ for Γ-X; $\mathbf{d} = (1,1)/\sqrt{2}$ and $\mathbf{d}_o = (0,0)$ for Γ-M; and $\mathbf{d} = (0,1)$ and $\mathbf{d}_o = (\pi/p, 0)$ for X-M; where $p = |\mathbf{p}_i|$ is the width of a square unit cell.

4.7.2 The Gâteaux derivatives of the Lagrangian L

The gradient of a functional $L[\mathbf{u}]$ with respect to $\mathbf{u}$, denoted by $\mathbf{g}_u$, is defined as [57]:

$$\int_{\Omega_{\text{cell}}} \tilde{\mathbf{u}}\cdot\mathbf{g}_u d\Omega = \delta_u L\left[\mathbf{u}\right](\tilde{\mathbf{u}}). \tag{4.32}$$

In the above, the Gâteaux derivative $\delta_u L[\mathbf{u}](\tilde{\mathbf{u}})$ is defined as:

$$\delta_u L\left[\mathbf{u}\right](\tilde{\mathbf{u}}) = \left.\frac{d}{d\varepsilon}\right|_{\varepsilon=0} L\left[\mathbf{u}+\varepsilon\tilde{\mathbf{u}}\right], \tag{4.33}$$

where $\tilde{\mathbf{u}}$ is a direction of the Gâteaux derivative. Then, the first-order optimality conditions read

$$\delta_v L\left[\ldots\right](\tilde{\mathbf{v}}) = 0 \quad \forall \tilde{\mathbf{v}} \in \mathcal{V}, \quad \delta_\xi L\left[\ldots\right]\left(\tilde{\xi}\right) = 0 \quad \forall \tilde{\xi} \in \mathbb{R} \tag{4.34a}$$

$$\delta_u L\left[\ldots\right](\tilde{\mathbf{u}}) = 0 \quad \forall \tilde{\mathbf{u}} \in \mathcal{V}, \quad \delta_k L\left[\ldots\right]\left(\tilde{k}\right) = 0 \quad \forall \tilde{k} \in \mathbb{C} \quad \text{and} \tag{4.34b}$$

$$\delta_\rho L\left[\ldots\right](\tilde{\rho}) = 0 \quad \forall \tilde{\rho} \in \mathcal{W}, \quad \delta_\lambda L\left[\ldots\right]\left(\tilde{\lambda}\right) = 0 \quad \forall \tilde{\lambda} \in \mathcal{W},$$

$$\delta_\mu L\left[\ldots\right](\tilde{\mu}) = 0 \quad \forall \tilde{\mu} \in \mathcal{W}. \tag{4.34c}$$

In the above, $[\ldots]$ is used to abbreviate arguments. First, the Gâteaux derivatives with respect to the adjoint variables (4.34a) are:

$$\delta_v L\left[\ldots\right](\tilde{\mathbf{v}}) = \mathrm{Re}\left\{P\left(k\right)(\tilde{\mathbf{v}}, \mathbf{u})\right\} \quad \text{and} \tag{4.35a}$$

$$\delta_\xi L\left[\ldots\right]\left(\tilde{\xi}\right) = \mathrm{Re}\left\{\frac{\tilde{\xi}}{2}\left[a_2\left(\mathbf{u}, \mathbf{u}\right) - 1\right]\right\}. \tag{4.35b}$$

Secondly, the Gâteaux derivative with respect to the state variables (4.34b) are:

$$\delta_u L\left[\ldots\right](\tilde{\mathbf{u}}) = \delta_u M\left[\ldots\right](\tilde{\mathbf{u}}) + \delta_u E\left[\ldots\right](\tilde{\mathbf{u}}) \quad \text{and} \tag{4.36a}$$

$$\delta_k L\left[\ldots\right]\left(\tilde{k}\right) = \delta_k M\left[\ldots\right]\left(\tilde{k}\right) + \delta_k E\left[\ldots\right]\left(\tilde{k}\right), \tag{4.36b}$$

where

$$\delta_u M\left[\ldots\right]\left(\tilde{\mathbf{u}}\right) = -\frac{\mathrm{Re}\left\{a_1\left(\mathbf{u},\tilde{\mathbf{u}}\right)\right\} + 2\mathrm{Re}\left\{k\right\}\mathrm{Re}\left\{a_2\left(\mathbf{u},\tilde{\mathbf{u}}\right)\right\}}{\omega a_{0,2}\left(\mathbf{u},\mathbf{u}\right)}\left(v_g - v_g^m\right) + \frac{a_1\left(\mathbf{u},\mathbf{u}\right) + 2\mathrm{Re}\left\{k\right\}a_2\left(\mathbf{u},\mathbf{u}\right)}{\omega\left[a_{0,2}\left(\mathbf{u},\mathbf{u}\right)\right]^2}\mathrm{Re}\left\{a_{0,2}\left(\mathbf{u},\tilde{\mathbf{u}}\right)\right\}\left(v_g - v_g^m\right), \tag{4.37a}$$

$$\delta_k M\left[\ldots\right]\left(\tilde{k}\right) = -\frac{\mathrm{Re}\{\tilde{k}\}a_2\left(\mathbf{u},\mathbf{u}\right)}{\omega a_{0,2}\left(\mathbf{u},\mathbf{u}\right)}\left(v_g - v_g^m\right), \tag{4.37b}$$

$$\delta_u E\left[\ldots\right]\left(\tilde{\mathbf{u}}\right) = \mathrm{Re}\left\{P\left(k\right)\left(\mathbf{v},\tilde{\mathbf{u}}\right)\right\} + \mathrm{Re}\left\{\xi a_2\left(\mathbf{u},\tilde{\mathbf{u}}\right)\right\}, \quad \text{and} \tag{4.37c}$$

$$\delta_k E\left[\ldots\right]\left(\tilde{k}\right) = \mathrm{Re}\left\{\tilde{k}a_1\left(\mathbf{v},\mathbf{u}\right) + 2k\tilde{k}a_2\left(\mathbf{v},\mathbf{u}\right)\right\}. \tag{4.37d}$$

Finally, the Gâteaux derivative with respect to the design variables (4.34c) are:

$$\delta_\rho L\left[\ldots\right]\left(\tilde{\rho}\right) = \delta_\rho M\left[\ldots\right]\left(\tilde{\rho}\right) + \delta_\rho E\left[\ldots\right]\left(\tilde{\rho}\right), \tag{4.38a}$$

$$\delta_\lambda L\left[\ldots\right]\left(\tilde{\lambda}\right) = \delta_\lambda M\left[\ldots\right]\left(\tilde{\lambda}\right) + \delta_\lambda E\left[\ldots\right]\left(\tilde{\lambda}\right), \quad \text{and} \tag{4.38b}$$

$$\delta_\mu L\left[\ldots\right]\left(\tilde{\mu}\right) = \delta_\mu M\left[\ldots\right]\left(\tilde{\mu}\right) + \delta_\mu E\left[\ldots\right]\left(\tilde{\mu}\right), \tag{4.38c}$$

where

$$\delta_\rho M\left[\ldots\right]\left(\tilde{\rho}\right) = \sum_{\alpha}^{N_{\mathrm{freq}}}\sum_{\beta}^{N_{\mathrm{dir}}}\sum_{\gamma}^{N_{\mathrm{mode}}} \left(\frac{a_1\left(\mathbf{u},\mathbf{u}\right) + 2\mathrm{Re}\left\{k\right\}a_2\left(\mathbf{u},\mathbf{u}\right)}{2\,\omega\left[a_{0,2}\left(\mathbf{u},\mathbf{u}\right)\right]^2}\right)\left(-\int_{\Omega_{\mathrm{cell}}}\overline{\mathbf{u}}\cdot\tilde{\rho}\mathbf{u}d\Omega\right)\left(v_g - v_g^m\right), \tag{4.39a}$$

$$\delta_\rho E\left[\ldots\right]\left(\tilde{\rho}\right) = \sum_{\alpha}^{N_{\mathrm{freq}}}\sum_{\beta}^{N_{\mathrm{dir}}}\sum_{\gamma}^{N_{\mathrm{mode}}}\mathrm{Re}\left\{-\int_{\Omega_{\mathrm{cell}}}\overline{\mathbf{v}}\cdot\tilde{\rho}\,\omega^2\mathbf{u}d\Omega\right\}, \tag{4.39b}$$

$$\delta_\lambda M\left[\ldots\right]\left(\tilde{\lambda}\right) = \sum_{\alpha}^{N_{\text{freq}}}\sum_{\beta}^{N_{\text{dir}}}\sum_{\gamma}^{N_{\text{mode}}} \left(-\frac{\mathrm{i}\int_{\Omega_{\text{cell}}}\left\{\operatorname{grad}\overline{\mathbf{u}} : \delta_\lambda\underline{\underline{\mathbf{C}}}\left[\mathbf{u}\otimes\mathbf{d}\right] - \left(\overline{\mathbf{u}}\otimes\mathbf{d}\right) : \delta_\lambda\underline{\underline{\mathbf{C}}}\left[\operatorname{grad}\mathbf{u}\right]\right\}d\Omega}{2\,\omega\,a_{0,2}\left(\mathbf{u},\mathbf{u}\right)} - \frac{2\mathrm{Re}\left\{k\right\}\int_{\Omega_{\text{cell}}}\left(\overline{\mathbf{u}}\otimes\mathbf{d}\right) : \delta_\lambda\underline{\underline{\mathbf{C}}}\left[\mathbf{u}\otimes\mathbf{d}\right]d\Omega}{2\,\omega\,a_{0,2}\left(\mathbf{u},\mathbf{u}\right)}\right)\left(v_g - v_g^m\right), \tag{4.39c}$$

$$\begin{aligned}\delta_\lambda E\left[\ldots\right]\left(\tilde{\lambda}\right) = {} & \sum_{\alpha}^{N_{\text{freq}}}\sum_{\beta}^{N_{\text{dir}}}\sum_{\gamma}^{N_{\text{mode}}} \mathrm{Re}\left\{\int_{\Omega_{\text{cell}}}\operatorname{grad}\overline{\mathbf{v}} : \delta_\lambda\underline{\underline{\mathbf{C}}}\left[\operatorname{grad}\mathbf{u}\right]d\Omega\right\} \\ & + \sum_{\alpha}^{N_{\text{freq}}}\sum_{\beta}^{N_{\text{dir}}}\sum_{\gamma}^{N_{\text{mode}}} \mathrm{Re}\left\{\mathrm{i}k\int_{\Omega_{\text{cell}}}\left\{\operatorname{grad}\overline{\mathbf{v}} : \delta_\lambda\underline{\underline{\mathbf{C}}}\left[\mathbf{u}\otimes\mathbf{d}\right] - \left(\overline{\mathbf{v}}\otimes\mathbf{d}\right) : \delta_\lambda\underline{\underline{\mathbf{C}}}\left[\operatorname{grad}\mathbf{u}\right]\right\}d\Omega\right\} \\ & + \sum_{\alpha}^{N_{\text{freq}}}\sum_{\beta}^{N_{\text{dir}}}\sum_{\gamma}^{N_{\text{mode}}} \mathrm{Re}\left\{k^2\int_{\Omega_{\text{cell}}}\left(\overline{\mathbf{v}}\otimes\mathbf{d}\right) : \delta_\lambda\underline{\underline{\mathbf{C}}}\left[\mathbf{u}\otimes\mathbf{d}\right]d\Omega\right\} \\ & + \sum_{\alpha}^{N_{\text{freq}}}\sum_{\beta}^{N_{\text{dir}}}\sum_{\gamma}^{N_{\text{mode}}} \mathrm{Re}\left\{\frac{\xi}{2}\int_{\Omega_{\text{cell}}}\left(\overline{\mathbf{v}}\otimes\mathbf{d}\right) : \delta_\lambda\underline{\underline{\mathbf{C}}}\left[\mathbf{u}\otimes\mathbf{d}\right]d\Omega\right\},\end{aligned} \tag{4.39d}$$

$$\delta_\mu M\left[\ldots\right]\left(\tilde{\mu}\right) = \sum_{\alpha}^{N_{\text{freq}}}\sum_{\beta}^{N_{\text{dir}}}\sum_{\gamma}^{N_{\text{mode}}} \left(-\frac{\mathrm{i}\int_{\Omega_{\text{cell}}}\left\{\operatorname{grad}\overline{\mathbf{u}} : \delta_\mu\underline{\underline{\mathbf{C}}}\left[\mathbf{u}\otimes\mathbf{d}\right] - \left(\overline{\mathbf{u}}\otimes\mathbf{d}\right) : \delta_\mu\underline{\underline{\mathbf{C}}}\left[\operatorname{grad}\mathbf{u}\right]\right\}d\Omega}{2\,\omega\,a_{0,2}\left(\mathbf{u},\mathbf{u}\right)} - \frac{2\mathrm{Re}\left\{k\right\}\int_{\Omega_{\text{cell}}}\left(\overline{\mathbf{u}}\otimes\mathbf{d}\right) : \delta_\mu\underline{\underline{\mathbf{C}}}\left[\mathbf{u}\otimes\mathbf{d}\right]d\Omega}{2\,\omega\,a_{0,2}\left(\mathbf{u},\mathbf{u}\right)}\right)\left(v_g - v_g^m\right), \quad \text{and} \tag{4.39e}$$

$$
\begin{aligned}
\delta_\mu E\left[\ldots\right](\tilde{\mu}) = &\sum_{\alpha}^{N_{\text{freq}}}\sum_{\beta}^{N_{\text{dir}}}\sum_{\gamma}^{N_{\text{mode}}} \operatorname{Re}\left\{\int_{\Omega_{\text{cell}}} \operatorname{grad}\overline{\mathbf{v}} : \delta_\mu\underline{\underline{\mathbf{C}}}\left[\operatorname{grad}\mathbf{u}\right] d\Omega\right\} \\
&+ \sum_{\alpha}^{N_{\text{freq}}}\sum_{\beta}^{N_{\text{dir}}}\sum_{\gamma}^{N_{\text{mode}}} \operatorname{Re}\Bigg\{\mathrm{i}k\int_{\Omega_{\text{cell}}} \left\{\operatorname{grad}\overline{\mathbf{v}} : \delta_\mu\underline{\underline{\mathbf{C}}}\left[\mathbf{u}\otimes\mathbf{d}\right]\right. \\
&\qquad\qquad \left. - \left(\overline{\mathbf{v}}\otimes\mathbf{d}\right) : \delta_\mu\underline{\underline{\mathbf{C}}}\left[\operatorname{grad}\mathbf{u}\right]\right\} d\Omega\Bigg\} \\
&+ \sum_{\alpha}^{N_{\text{freq}}}\sum_{\beta}^{N_{\text{dir}}}\sum_{\gamma}^{N_{\text{mode}}} \operatorname{Re}\left\{k^2\int_{\Omega_{\text{cell}}} \left(\overline{\mathbf{v}}\otimes\mathbf{d}\right) : \delta_\mu\underline{\underline{\mathbf{C}}}\left[\mathbf{u}\otimes\mathbf{d}\right] d\Omega\right\} \\
&+ \sum_{\alpha}^{N_{\text{freq}}}\sum_{\beta}^{N_{\text{dir}}}\sum_{\gamma}^{N_{\text{mode}}} \operatorname{Re}\left\{\frac{\xi}{2}\int_{\Omega_{\text{cell}}} \left(\overline{\mathbf{v}}\otimes\mathbf{d}\right) : \delta_\mu\underline{\underline{\mathbf{C}}}\left[\mathbf{u}\otimes\mathbf{d}\right] d\Omega\right\}. \qquad (4.39\text{f})
\end{aligned}
$$

In the above, we used:

$$
\delta_\lambda\underline{\underline{\mathbf{C}}}\left[\,\right] = \tilde{\lambda}\operatorname{tr}\left[\,\right]\underline{\mathbf{I}} \quad \text{and} \qquad (4.40\text{a})
$$

$$
\delta_\mu\underline{\underline{\mathbf{C}}}\left[\,\right] = \tilde{\mu}\left[\,\right] + \tilde{\mu}\left[\,\right]^{\mathsf{T}}. \qquad (4.40\text{b})
$$

Chapter 5

Topology design of periodic media for group velocity control

We are interested in designing the topology of the unit cell when a user-defined group velocity profile is given. We use the framework of the inverse metamaterial design approach introduced in previous chapters, suitably modified to account for design variables parameterizing the geometry of the unit cell. The modifications affect only the gradient of the Lagrangian, thus leaving the state and the adjoint problems intact.

5.1 Introduction

We revisit the group velocity-driven design framework [22, 24] with a modification on the choice of design variables to allow inversion for geometric parameters of a unit cell instead of the material properties. Topology design entails manufacturability advantages, especially in light of recent developments in 3D printing technologies that facilitate manufacturing of complex structures at various length scales.

We demonstrate the approach by considering a unit cell exhibiting internal cavities, while its outer boundary remains fixed. The internal bound-

aries are parameterized, while using the same Lagrangian introduced in [22,24]. Then, the first two optimality conditions, leading to the state and adjoint problems, remain the same. In this chapter, we focus mainly on the derivation of the gradient of the Lagrangian, i.e., on the third optimality condition, when the geometry of the unit cell becomes the design objective.

5.2 Problem definition

Consider a unit cell in N_{d} dimension encompassing internal cavities of arbitrary shape (Figure 5.1). Then, the strong form of the eigenvalue problem reads:

$$\operatorname{div}\left\{\underline{\underline{\mathbf{C}}}\left[\operatorname{grad}\mathbf{U}\right]\right\}+\rho\,\omega^2\mathbf{U}=\mathbf{0}\quad \boldsymbol{x}\in\Omega_{\mathrm{cell}}. \tag{5.1}$$

In the above, $\mathbf{U}$ is displacement field, $\underline{\underline{\mathbf{C}}}$ is the elasticity tensor, ρ is mass density, and Ω_{cell} is the unit cell's domain. The boundary of the unit cell is denoted by $\Gamma_{\mathrm{cell}}=\Gamma_{\mathrm{B}}\cup\Gamma_{\mathrm{C}}$, where Γ_{B} is the outer boundary (fixed) of the unit cell and Γ_{C} is the union of the boundaries of all internal cell cavities. Each cavity boundary is denoted by Γ_{C_i}, $i=1,2,\ldots,n$, and thus, $\Gamma_{\mathrm{C}}=\Gamma_{C_1}\cup\Gamma_{C_2}\cup\ldots\cup\Gamma_{C_n}$. We apply the Floquet-Bloch periodic boundary condition on Γ_{B}, and homogeneous Neumann boundary conditions on Γ_{C}, i.e.,

$$\underline{\underline{\mathbf{C}}}\left[\operatorname{grad}\mathbf{U}\right]\mathbf{n}=\mathbf{0},\quad \boldsymbol{x}\in\Gamma_{\mathrm{C}}\quad\text{and} \tag{5.2a}$$

$$\mathbf{U}\left(\boldsymbol{x}\right)-\mathrm{e}^{\pm\mathrm{i}\mathbf{k}\cdot\mathbf{p}_i}\mathbf{U}\left(\boldsymbol{x}\pm\mathbf{p}_i\right)=\mathbf{0},\quad \boldsymbol{x}\in\Gamma_{\mathrm{B}},\ i=1,2,\ldots,N_{\mathrm{d}}. \tag{5.2b}$$

In the above, $\mathbf{n}$ is an outward normal vector on the boundary, $\mathbf{p}_i$ are primitive vectors, and $\mathbf{k}$ is the Floquet-Bloch wavevector.

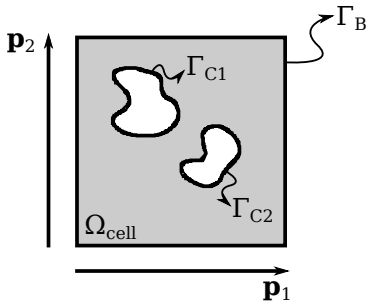

Figure 5.1: Two-dimensional unit cell with two cavities

Alternatively, one can formulate the Floquet-Bloch eigenvalue problem by replacing $\mathbf{U}$ with the Floquet-Bloch wave, i.e.,

$$\mathbf{U}(\boldsymbol{x}) = \mathrm{e}^{\mathrm{i}\mathbf{k}\cdot\boldsymbol{x}}\mathbf{u}(\boldsymbol{x}). \tag{5.3}$$

In the above, $\mathbf{u}$ is a periodic function with the same periodicity as that of the unit cell. Then, the weak form of the Floquet-Bloch eigenvalue problem (EP) reads

Floquet-Bloch EP: given $\omega \in \mathbb{R}$ and $\mathbf{d} \in \mathbb{R}^{N_\mathrm{d}}$, find $k \in \mathbb{C}$ and $\mathbf{u} \in \mathcal{V}^{N_\mathrm{d}} \setminus \{\mathbf{0}\}$ such that

$$P(k)(\mathbf{v},\mathbf{u}) \equiv a_0(\mathbf{v},\mathbf{u}) + k a_1(\mathbf{v},\mathbf{u}) + k^2 a_2(\mathbf{v},\mathbf{u}) = 0, \quad \forall \mathbf{v} \in \mathcal{V}^{N_\mathrm{d}}, \tag{5.4}$$

where

$$\mathcal{V} = \left\{ w \in H^1\left(\Omega_{\text{cell}}\right) \,|\, w\left(\boldsymbol{x}\right) = w\left(\boldsymbol{x} + \sum_{i=1}^{N_{\text{d}}} m_i \mathbf{p}_i\right) \;\forall \boldsymbol{x} \in \partial\Omega_{\text{cell}} \right\}, \tag{5.5a}$$

$$a_0\left(\mathbf{v}, \mathbf{u}\right) = \int_{\Omega_{\text{cell}}} \left\{ \operatorname{grad} \overline{\mathbf{v}} : \underline{\underline{\mathbf{C}}} \left[\operatorname{grad} \mathbf{u}\right] - \overline{\mathbf{v}} \cdot \omega^2 \rho\, \mathbf{u} \right\} d\Omega, \tag{5.5b}$$

$$a_1\left(\mathbf{v}, \mathbf{u}\right) = \mathrm{i} \int_{\Omega_{\text{cell}}} \left\{ \operatorname{grad} \overline{\mathbf{v}} : \underline{\underline{\mathbf{C}}} \left[\mathbf{u} \otimes \mathbf{d}\right] - \left(\overline{\mathbf{v}} \otimes \mathbf{d}\right) : \underline{\underline{\mathbf{C}}} \left[\operatorname{grad} \mathbf{u}\right] \right\} d\Omega, \quad \text{and} \tag{5.5c}$$

$$a_2\left(\mathbf{v}, \mathbf{u}\right) = \int_{\Omega_{\text{cell}}} \left(\overline{\mathbf{v}} \otimes \mathbf{d}\right) : \underline{\underline{\mathbf{C}}} \left[\mathbf{u} \otimes \mathbf{d}\right] d\Omega. \tag{5.5d}$$

In the above, $\mathbf{v}$ is a test function, an overline $\overline{(\,)}$ denotes a complex-conjugate of the subtended quantity, $(:)$ denotes double contraction, $\otimes$ denotes tensor product, and $\mathbf{d}$ is a direction of interest such that $\mathbf{k} = k\mathbf{d}$, with $|\mathbf{d}| = 1$.

The directional group velocity along $\mathbf{d}$ can be expressed in terms of the above functionals as:

$$\begin{aligned} v_g &= \mathbf{v}_g \cdot \mathbf{d} = \operatorname{Re}\left\{ \frac{\partial \omega}{\partial k} \right\} \\ &= -\frac{a_1\left(\mathbf{u}, \mathbf{u}\right) + 2\operatorname{Re}\left\{k\right\} a_2\left(\mathbf{u}, \mathbf{u}\right)}{2\,\omega\, a_{0,2}\left(\mathbf{u}, \mathbf{u}\right)}, \end{aligned} \tag{5.6}$$

where

$$a_{0,2}\left(\mathbf{v}, \mathbf{u}\right) = -\int_{\Omega_{\text{cell}}} \overline{\mathbf{v}} \cdot \rho\, \mathbf{u}\, d\Omega. \tag{5.7}$$

We note that the cavities boundary Γ_{C} is parameterized, and its parameters are treated as the inversion variables, which, consequently, are updated at each inversion iteration. This process forces the evolution of Γ_{C} at each

inversion iteration, from Γ_{C} to Γ'_{C} (Figure 5.2). Accordingly, let the point on the boundary $\boldsymbol{x}$ evolve to $\boldsymbol{x}'$, i.e., let

$$\boldsymbol{x}' = \boldsymbol{x} + \Delta\boldsymbol{x}. \tag{5.8}$$

In the above, the update amount $\Delta\boldsymbol{x}$ at any position on the boundary $\boldsymbol{x} \in \Gamma_{\mathrm{C}}$ is parameterized by a vector of nodal coordinate updates $\mathbf{s} \in \mathbb{R}^{N_{\mathrm{bn}} \cdot N_{\mathrm{d}}}$, where N_{bn} is the number of nodes resulting from the parameterization of the boundary Γ_{C}. We discuss the boundary parameterization in section 5.3.

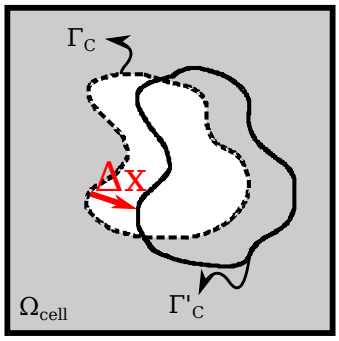

Figure 5.2: Evolving boundary

Thus, the inverse design problem is defined as

Inverse metamaterial design: given $v_g^m \in \mathbb{R}$ and initial topology of a unit cell Ω_{cell}, find $\mathbf{s} \in \mathbb{R}^{N_{\mathrm{bn}} \cdot N_{\mathrm{d}}}$ such that

$$\min L\left[\mathbf{u}, k, \mathbf{v}, \xi, \mathbf{s}\right], \tag{5.9}$$

where,

$$L\left[\mathbf{u},k,\mathbf{v},\xi,\mathbf{s}\right] = M\left[\mathbf{u},k,\mathbf{s}\right] + E\left[\mathbf{u},k,\mathbf{v},\xi,\mathbf{s}\right], \tag{5.10a}$$

$$M\left[\mathbf{u},k,\mathbf{s}\right] = \sum_{\alpha}^{N_{\text{freq}}}\sum_{\beta}^{N_{\text{dir}}}\sum_{\gamma}^{N_{\text{mode}}}\frac{1}{2}\left(v_{g,\alpha\beta\gamma} - v^{m}_{g,\alpha\beta\gamma}\right)^{2}, \quad \text{and} \tag{5.10b}$$

$$\begin{aligned} E\left[\mathbf{u},k,\mathbf{v},\xi,\mathbf{s}\right] = &\sum_{\alpha}^{N_{\text{freq}}}\sum_{\beta}^{N_{\text{dir}}}\sum_{\gamma}^{N_{\text{mode}}}\text{Re}\left\{P\left(k\right)\left(\mathbf{v},\mathbf{u}\right)\right\}_{\alpha\beta\gamma} \\ &+ \sum_{\alpha}^{N_{\text{freq}}}\sum_{\beta}^{N_{\text{dir}}}\sum_{\gamma}^{N_{\text{mode}}}\left[\frac{\xi}{2}\left\{a_2\left(\mathbf{u},\mathbf{u}\right)-1\right\}\right]_{\alpha\beta\gamma}. \end{aligned} \tag{5.10c}$$

In the above, M is an objective functional, E is the dispersion constraint, $\mathbf{u}$ is the eigenfunction, k is the eigenvalue, $\mathbf{v}$ is the adjoint eigenfunction, and ξ is the adjoint eigenvalue. N_{freq} is the set of the discrete target frequencies, N_{dir} are the user-defined directions, and N_{mode} is the number of modes. In the following, we drop the indices α, β, and γ to reduce notational congestion.

5.3 Isoparametric boundary

We parameterize positions $\boldsymbol{x}$ and, therefore $\Delta\boldsymbol{x}$ as well, using the same parameterization used for the eigenfunction $\mathbf{u}$, i.e.,

$$\Delta\boldsymbol{x} \approx \bigcup_{e} \Delta\boldsymbol{x}^{e}. \tag{5.11}$$

In the above, $\Delta\boldsymbol{x}^{e}$ is the elemental boundary update, and $\bigcup_{e}$ denotes finite element summation. For a finite element with N_{node} number of elemental nodes, $\Delta\boldsymbol{x}^{e}$ is parameterized by

$$\Delta\boldsymbol{x}^{e} = \boldsymbol{\Phi}\mathbf{s}^{e} \quad \text{or in terms of indices} \quad \Delta x_i^{e} = \Phi_{ij}s_j^{e}, \tag{5.12}$$

where $\mathbf{\Phi}$ is a two-dimensional array with the size of $N_{\mathrm{d}} \times N_{\mathrm{node}} \cdot N_{\mathrm{d}}$, and $\mathbf{s}^e$ is an elemental vector of nodal updates of size $N_{\mathrm{d}} \cdot N_{\mathrm{node}}$. For example a two dimensional problem ($N_{\mathrm{d}} = 2$) using quadratic triangular elements ($N_{\mathrm{node}} = 6$), yields:

$$\begin{aligned}
\mathbf{\Phi} &= \begin{bmatrix} \Phi_{11} & \Phi_{12} & \Phi_{13} & \Phi_{14} & \dots & \Phi_{1(11)} & \Phi_{1(12)} \\ \Phi_{21} & \Phi_{22} & \Phi_{23} & \Phi_{24} & \dots & \Phi_{2(11)} & \Phi_{2(12)} \end{bmatrix} \\
&= \begin{bmatrix} N_1 & 0 & N_2 & 0 & \cdots & N_6 & 0 \\ 0 & N_1 & 0 & N_2 & \cdots & 0 & N_6 \end{bmatrix} \quad \text{and} \qquad (5.13a) \\
\mathbf{s}^e &= \begin{pmatrix} x_1 & y_2 & x_2 & y_2 & \dots & x_6 & y_6 \end{pmatrix}^{\mathsf{T}}. \qquad (5.13b)
\end{aligned}$$

In the above, each shape function N_i is a function of three parent coordinates q_i, $i = 1, 2, 3$ called barycentric or area coordinates such that $\sum_i q_i = 1$, i.e.,

$$N_1 = (2q_1 - 1)q_1, \qquad (5.14a)$$

$$N_2 = (2q_2 - 1)q_2, \qquad (5.14b)$$

$$N_3 = (2q_3 - 1)q_3, \qquad (5.14c)$$

$$N_4 = 4q_1q_2, \qquad (5.14d)$$

$$N_5 = 4q_2q_3, \quad \text{and} \qquad (5.14e)$$

$$N_6 = 4q_3q_1. \qquad (5.14f)$$

Figure 5.3 shows the numbering for the elemental nodes and the area coordinates of a quadratic triangular element. Note that a parameterized quantity on the side of an element only depends on the nodal values on the same side; thus, the boundary update $\Delta\boldsymbol{x}$ is described only by the nodes on the boundary.

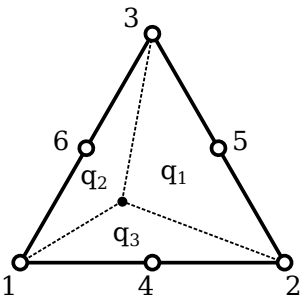

Figure 5.3: Quadratic triangular element

Since the cavities boundary Γ_C evolves during inversion iterations, the boundary and domain integrals have to be evaluated over, effectively, "moving" boundaries and "moving" domains. In this sense, the problem is no different than moving boundary problems in time. Accordingly, we use the Reynolds transport theorem to differentiate functionals with respect to each entry of the nodal update vector $\mathbf{s}$. The theorem is written in terms of a pseudo-time-derivative of an integral form over a pseudo-time-evolving domain, i.e.,

$$\frac{d}{dt}\int_{\Omega(t)} f\left(t\right) d\Omega = \int_{\Omega(t)} \frac{\partial f\left(t\right)}{\partial t} d\Omega + \int_{\Gamma(t)} \mathbf{w}\cdot\mathbf{n} f\left(t\right) d\Gamma, \tag{5.15}$$

where f is an arbitrary scalar function, $\mathbf{n}$ is the normal vector on the boundary, and $\mathbf{w}$ is the velocity of the evolving domain. Let s_i denote the i-th component of the nodal updates $\mathbf{s}$. Then, the velocity term $\mathbf{w}_i$ corresponding to d/ds_i becomes

$$\mathbf{w}_i = \frac{\partial \Delta \boldsymbol{x}}{\partial s_i} = \frac{\partial}{\partial s_i}\bigcup_e \mathbf{\Phi}\mathbf{s}^e = \bigcup_e \mathbf{\Phi}\frac{\partial \mathbf{s}^e}{\partial s_i}. \tag{5.16}$$

Then, the Reynolds transport theorem (5.15) yields:

$$\frac{d}{ds_i}\int_{\Omega(\mathbf{s})} f\left(\mathbf{s}\right) d\Omega = \int_{\Omega(\mathbf{s})} \frac{\partial f\left(\mathbf{s}\right)}{\partial s_i} d\Omega + \int_{\Gamma(\mathbf{s})} \mathbf{w}_i\cdot\mathbf{n} f\left(\mathbf{s}\right) d\Gamma. \tag{5.17}$$

Let $\boldsymbol{x}^{(l)}$ denote the coordinate at the l-th inversion iteration; then, the coordinate of the next iteration can be written as

$$\boldsymbol{x}^{(l+1)} = \boldsymbol{x}^{(l)} + \Delta\boldsymbol{x}. \tag{5.18}$$

Thus, in the above discretized evolution, we evaluate the derivative with respect to s_i, at $\mathbf{s} = \mathbf{0}$. In general, the most complete evolution of the boundary should allow for boundary nodes to move along two possible directions (in 2D) (e.g., tangential and normal to the boundary). However, for small increments, it is sufficient to constrain the boundary updates such that the position $\boldsymbol{x}$ moves only in the direction perpendicular to the boundary, i.e., along the outward normal vector directions. In such a case, we replace $\Delta\boldsymbol{x}$ with $\Delta\boldsymbol{X}$, i.e.,

$$\Delta\boldsymbol{X} = (\mathbf{n} \otimes \mathbf{n})\, \Delta\boldsymbol{x}. \tag{5.19}$$

In the above, $\mathbf{n}$ is the normal vector of the boundary and $\Delta\boldsymbol{X}$ is the constrained boundary update. Then, the corresponding velocity term becomes

$$\mathbf{w}_i = \frac{\partial \Delta\boldsymbol{X}}{\partial s_i} = (\mathbf{n} \otimes \mathbf{n}) \bigcup_e \boldsymbol{\Phi} \frac{\partial \mathbf{s}^e}{\partial s_i}. \tag{5.20}$$

5.4 Solution method

We seek a stationary point of the optimization problem by satisfying the first-order optimality conditions, i.e.,

$$\frac{\delta L}{\delta \mathbf{v}} = \mathbf{0}, \quad \frac{\partial L}{\partial \xi} = 0, \tag{5.21a}$$

$$\frac{\delta L}{\delta \mathbf{u}} = \mathbf{0}, \quad \frac{\partial L}{\partial k} = 0, \quad \text{and} \tag{5.21b}$$

$$\left.\frac{dL}{ds_i}\right|_{\mathbf{s}=\mathbf{0}} = 0, \quad i = 1, 2, \ldots, N_{\mathrm{d}} \cdot N_{\mathrm{bn}}. \tag{5.21c}$$

In the above, $\delta L/\delta \mathbf{x}$ denotes a Fréchet derivative of a functional L with respect to a function $\mathbf{x}$. The optimality conditions are not satisfied unless we evaluate them at a stationary point. Otherwise, the first two optimality conditions, (5.21a) and (5.21b), yield the state and adjoint problems, respectively, identical to those defined in [24]. The left-hand-side of the third optimality condition (5.21c) gives the gradient of L with respect to $\mathbf{s}$. Then, any gradient based algorithm, e.g., conjugate gradient method, can be used to update the cell's trial topology.

5.4.1 State and adjoint problems

Because the state and adjoint problems are identical to those defined in [24], we omit the derivations and restate them below in weak form.

State problem: given a trial domain Ω_{cell}, find $\mathbf{u} \in \mathcal{V}^{N_{\mathrm{d}}} \setminus \{\mathbf{0}\}$ and $k \in \mathbb{C}$ such

that

$$P(k)(\tilde{\mathbf{v}}, \mathbf{u}) = 0 \quad \forall \tilde{\mathbf{v}} \in \mathcal{V}^{N_\mathrm{d}} \quad \text{and} \tag{5.22a}$$

$$\frac{\tilde{\xi}}{2}\{a_2(\mathbf{u}, \mathbf{u}) - 1\} = 0 \quad \forall \tilde{\xi} \in \mathbb{R}. \tag{5.22b}$$

Adjoint problem: given the solutions to the state problem $\mathbf{u} \in \mathcal{V}^{N_\mathrm{d}} \setminus \{\mathbf{0}\}$, and $k \in \mathbb{C}$, find $\mathbf{v} \in \mathcal{V}^{N_\mathrm{d}}$ and $\xi \in \mathbb{R}$ such that

$$\begin{aligned} P(k)(\mathbf{v}, \tilde{\mathbf{u}}) + \xi a_2(\mathbf{u}, \tilde{\mathbf{u}}) &= \frac{a_1(\mathbf{u}, \tilde{\mathbf{u}}) + 2\mathrm{Re}\{k\} a_2(\mathbf{u}, \tilde{\mathbf{u}})}{\omega\, a_{0,2}(\mathbf{u}, \mathbf{u})}\left(v_g - v_g^m\right) \\ - \frac{a_1(\mathbf{u}, \mathbf{u}) + 2\mathrm{Re}\{k\} a_2(\mathbf{u}, \mathbf{u})}{\omega\left[a_{0,2}(\mathbf{u}, \mathbf{u})\right]^2} a_{0,2}(\mathbf{u}, \tilde{\mathbf{u}})&\left(v_g - v_g^m\right) \quad \forall \tilde{\mathbf{u}} \in \mathcal{V}^{N_\mathrm{d}} \quad \text{and} \end{aligned} \tag{5.23a}$$

$$\tilde{k} a_1(\mathbf{v}, \mathbf{u}) + 2k\tilde{k} a_2(\mathbf{v}, \mathbf{u}) = \frac{\tilde{k} a_2(\mathbf{u}, \mathbf{u})}{\omega\, a_{0,2}(\mathbf{u}, \mathbf{u})}\left(v_g - v_g^m\right) \quad \forall \tilde{k} \in \mathbb{C}. \tag{5.23b}$$

In the above, a tilde $\tilde{(\,)}$ denotes the direction of a Gâteaux derivative which is related to the Fréchet derivative as

$$\int_{\Omega_\mathrm{cell}} \tilde{\mathbf{x}} \cdot \frac{\delta F}{\delta \mathbf{x}} d\Omega = \left.\frac{d}{d\varepsilon}\right|_{\varepsilon=0} F\left[\mathbf{x} + \varepsilon\tilde{\mathbf{x}}\right]. \tag{5.24}$$

Note that the vanishing of a Gâteaux derivative for all directions is equivalent to the vanishing of the corresponding Fréchet derivative; thus, the vanishing of the above weak forms implies the satisfaction of the first and second optimality conditions (5.21a) and (5.21b), respectively.

5.4.2 Reduced gradient of L

We use (5.17) to take the derivatives of functionals with respect to $\mathbf{s}$. First, we introduce the following notations for boundary integrals on Γ_{cell}:

$$b_0^i(\mathbf{v},\mathbf{u})_{\Gamma_{\text{cell}}} = \int_{\Gamma_{\text{cell}}} \mathbf{w}_i \cdot \mathbf{n} \left\{ \operatorname{grad} \overline{\mathbf{v}} : \underline{\underline{\mathbf{C}}} [\operatorname{grad} \mathbf{u}] - \overline{\mathbf{v}} \cdot \omega^2 \rho \, \mathbf{u} \right\} d\Gamma, \tag{5.25a}$$

$$\begin{aligned} b_1^i(\mathbf{v},\mathbf{u})_{\Gamma_{\text{cell}}} = \mathrm{i} \int_{\Gamma_{\text{cell}}} \mathbf{w}_i \cdot \mathbf{n} \big\{ & \operatorname{grad} \overline{\mathbf{v}} : \underline{\underline{\mathbf{C}}} [\mathbf{u} \otimes \mathbf{d}] \\ & - (\overline{\mathbf{v}} \otimes \mathbf{d}) : \underline{\underline{\mathbf{C}}} [\operatorname{grad} \mathbf{u}] \big\} \, d\Gamma, \end{aligned} \tag{5.25b}$$

$$b_2^i(\mathbf{v},\mathbf{u})_{\Gamma_{\text{cell}}} = \int_{\Gamma_{\text{cell}}} \mathbf{w}_i \cdot \mathbf{n} \, (\overline{\mathbf{v}} \otimes \mathbf{d}) : \underline{\underline{\mathbf{C}}} [\mathbf{u} \otimes \mathbf{d}] \, d\Gamma, \quad \text{and}$$

$$b_{0,2}^i(\mathbf{v},\mathbf{u})_{\Gamma_{\text{cell}}} = - \int_{\Gamma_{\text{cell}}} \mathbf{w}_i \cdot \mathbf{n} \, (\overline{\mathbf{v}} \cdot \rho \, \mathbf{u}) \, d\Gamma. \tag{5.25c}$$

Then, the derivative of the misfit M with respect to s_i, $i = 1, 2, \ldots, N_{\text{bn}} \cdot N_{\text{d}}$, becomes

$$\begin{aligned} \frac{dM}{ds_i} = & - \frac{\operatorname{Re}\left\{ a_1\left(\mathbf{u}, \frac{\partial}{\partial s_i}\mathbf{u}\right)\right\} + 2\operatorname{Re}\{k\} \operatorname{Re}\left\{ a_2\left(\mathbf{u}, \frac{\partial}{\partial s_i}\mathbf{u}\right)\right\}}{\omega a_{0,2}(\mathbf{u},\mathbf{u})} \left(v_g - v_g^m\right) \\ & + \frac{a_1(\mathbf{u},\mathbf{u}) + 2\operatorname{Re}\{k\} a_2(\mathbf{u},\mathbf{u})}{\omega \left[a_{0,2}(\mathbf{u},\mathbf{u})\right]^2} \operatorname{Re}\left\{ a_{0,2}\left(\mathbf{u}, \frac{\partial}{\partial s_i}\mathbf{u}\right)\right\} \left(v_g - v_g^m\right) \\ & - \frac{a_2(\mathbf{u},\mathbf{u})}{\omega a_{0,2}(\mathbf{u},\mathbf{u})} \operatorname{Re}\left\{ \frac{\partial k}{\partial s_i}\right\} \left(v_g - v_g^m\right) \\ & - \frac{\operatorname{Re}\left\{ b_1^i(\mathbf{u},\mathbf{u})_{\Gamma_{\text{cell}}}\right\} + 2\operatorname{Re}\{k\} \operatorname{Re}\left\{ b_2^i(\mathbf{u},\mathbf{u})_{\Gamma_{\text{cell}}}\right\}}{\omega a_{0,2}(\mathbf{u},\mathbf{u})} \left(v_g - v_g^m\right) \\ & + \frac{a_1(\mathbf{u},\mathbf{u}) + 2\operatorname{Re}\{k\} a_2(\mathbf{u},\mathbf{u})}{\omega \left[a_{0,2}(\mathbf{u},\mathbf{u})\right]^2} \operatorname{Re}\left\{ b_{0,2}^i(\mathbf{u},\mathbf{u})_{\Gamma_{\text{cell}}}\right\} \left(v_g - v_g^m\right) \end{aligned} \tag{5.26a}$$

and the derivative of the constraint E becomes

$$\begin{aligned}\frac{dE}{ds_i} &= \mathrm{Re}\left\{ P(k)\left(\frac{\partial}{\partial s_i}\mathbf{v}, \mathbf{u}\right) + P(k)\left(\mathbf{v}, \frac{\partial}{\partial s_i}\mathbf{u}\right) \right\} \\ &+ \mathrm{Re}\left\{ \frac{\partial k}{\partial s_i} a_1(\mathbf{v}, \mathbf{u}) + 2k\frac{\partial k}{\partial s_i} a_2(\mathbf{v}, \mathbf{u}) \right\} \\ &+ \mathrm{Re}\left\{ b_0^i(\mathbf{v}, \mathbf{u})_{\Gamma_{\mathrm{cell}}} + k b_1^i(\mathbf{v}, \mathbf{u})_{\Gamma_{\mathrm{cell}}} + k^2 b_2^i(\mathbf{v}, \mathbf{u})_{\Gamma_{\mathrm{cell}}} \right\} \\ &+ \mathrm{Re}\left\{ \xi a_2\left(\mathbf{u}, \frac{\partial}{\partial s_i}\mathbf{u}\right) + \frac{\partial \xi}{\partial s_i}\frac{1}{2}\left[a_2(\mathbf{u}, \mathbf{u}) - 1\right] + \frac{\xi}{2} b_2^i(\mathbf{u}, \mathbf{u})_{\Gamma_{\mathrm{cell}}} \right\}. \end{aligned} \tag{5.26b}$$

In the above, summation symbols $\sum_{\alpha}^{N_{\mathrm{freq}}} \sum_{\beta}^{N_{\mathrm{dir}}} \sum_{\gamma}^{N_{\mathrm{mode}}}$ are omitted on the right-hand-side of equations. Finally, we have

Reduced gradient of L: given the solutions to the state and adjoint problems $\mathbf{v} \in \mathcal{V}^{N_{\mathrm{d}}}$, $\xi \in \mathbb{R}$, $\mathbf{u} \in \mathcal{V}^{N_{\mathrm{d}}} \setminus \{\mathbf{0}\}$, $k \in \mathbb{C}$, there result:

$$\begin{aligned} g_i \equiv \left.\frac{dL}{ds_i}\right|_{\mathbf{s}=\mathbf{0}} &= \left.\frac{dM}{ds_i}\right|_{\mathbf{s}=\mathbf{0}} + \left.\frac{dE}{ds_i}\right|_{\mathbf{s}=\mathbf{0}} \\ &= \sum_{\alpha}^{N_{\mathrm{freq}}} \sum_{\beta}^{N_{\mathrm{dir}}} \sum_{\gamma}^{N_{\mathrm{mode}}} \\ &\Bigg[-\frac{\mathrm{Re}\left\{b_1^i(\mathbf{u}, \mathbf{u})_{\Gamma_{\mathrm{C}}}\right\} + 2\mathrm{Re}\left\{k\right\}\mathrm{Re}\left\{b_2^i(\mathbf{u}, \mathbf{u})_{\Gamma_{\mathrm{C}}}\right\}}{\omega a_{0,2}(\mathbf{u}, \mathbf{u})}\left(v_g - v_g^m\right) \\ &+ \frac{a_1(\mathbf{u}, \mathbf{u}) + 2\mathrm{Re}\left\{k\right\} a_2(\mathbf{u}, \mathbf{u})}{\omega\left[a_{0,2}(\mathbf{u}, \mathbf{u})\right]^2}\mathrm{Re}\left\{b_{0,2}^i(\mathbf{u}, \mathbf{u})_{\Gamma_{\mathrm{C}}}\right\}\left(v_g - v_g^m\right) \\ &+ \mathrm{Re}\left\{b_0^i(\mathbf{v}, \mathbf{u})_{\Gamma_{\mathrm{C}}} + k b_1^i(\mathbf{v}, \mathbf{u})_{\Gamma_{\mathrm{C}}} + k^2 b_2^i(\mathbf{v}, \mathbf{u})_{\Gamma_{\mathrm{C}}}\right\} \\ &+ \mathrm{Re}\left\{\frac{\xi}{2} b_2^i(\mathbf{u}, \mathbf{u})_{\Gamma_{\mathrm{C}}}\right\} \Bigg]_{\mathbf{s}=\mathbf{0}} \qquad i = 1, 2, \ldots, N_{\mathrm{bn}} \cdot N_{\mathrm{d}}. \end{aligned} \tag{5.27}$$

Note that, assuming $\partial\mathbf{v}/\partial s_i, \partial\mathbf{u}/\partial s_i \in \mathcal{V}^{N_{\mathrm{d}}}$, all terms involving $\partial/\partial s_i$ vanish when the state and adjoint problems are satisfied. In addition, we constrain

Γ_{B} to be constant; thus, we integrate along Γ_{C} only.

5.4.3 Inversion process

We update the boundary Γ_{C} informed by the reduced gradient of L. Let $\mathbf{p}^{(l)}$ denote the nodal coordinate at the l-th inversion iteration; then, the nodal coordinates of the next iteration is

$$\mathbf{p}^{(l+1)} = \mathbf{p}^{(l)} + \zeta \mathbf{d}^{(l)}, \tag{5.28}$$

where $\mathbf{d}^{(l)}$ is the search direction and $\zeta \in \mathbb{R}$ is the step length. The steepest descent method uses

$$\left[\mathbf{d}^{(l)}\right]_i = -g_i^{(l)} \tag{5.29}$$

where

$$g_i^{(l)} = \left(\frac{dL}{ds_i}\bigg|_{\mathbf{s}=\mathbf{0}} \right)^{(l)}. \tag{5.30}$$

Alternatively, the conjugate gradient method [49] uses

$$\left[\mathbf{d}^{(l)}\right]_i = \begin{cases} -g_i^{(l)}, & l = 0 \\ -\dfrac{\sum\limits_j g_j^{(l)} g_j^{(l)}}{\sum\limits_j g_j^{(l-1)} g_j^{(l-1)}} g_i^{(l)}, & l > 0 \end{cases}. \tag{5.31}$$

Backtracking algorithm can be used to determine ζ [49]. Any update of $\boldsymbol{x}$ requires re-meshing the domain when evaluating the misfit functional M. To reduce computational cost, however, we omit the re-meshing at each step of the backtracking algorithm resulting in an inexact evaluation of M. Instead, we re-mesh only at the end of each inversion iteration.

The inverse design process is summarized in Algorithm 4.

Algorithm 4 Inverse topology design

1: Sample the target group velocity v_g^m ($v_g^m = 0$ for band gaps) at discrete frequencies, directions, and modes
2: Define the material properties ρ, λ, and μ
3: Set the error tolerance ε.
4: Initialize the iteration counter $l \leftarrow 0$
5: Set the initial search length
6: Set initial topology (mesh) of the unit cell.
7: **for** $\|M_{l+1} - M_l\| > \varepsilon \|M_l\|$ **do**
8: Solve the state problem and evaluate M_l ▷ equations (5.10b) and (5.22)
9: Solve the adjoint problem ▷ equation (5.23)
10: Compute the gradient of L ▷ equations (5.27)
11: Obtain the search direction (e.g., conjugate gradient method)
12: Update the topology of the unit cell using backtracking algorithm; stop if sufficient-decrease condition is violated
13: Re-mesh the domain Ω_{cell}
14: Set $l \leftarrow l + 1$
15: **end for**

5.5 Summary remarks

In the above, we formulated a topology design problem to engineer the group velocity profile of a periodic medium using the same framework of the material design problems [22, 24]. We used the geometric parameters of the internal boundaries of a unit cell as the design variables of the inverse problem. The state and adjoint problems remained the same as those associated with the inverse material design problems. We use the Reynolds transport theorem to derive the gradient of the Lagrangian with respect to design variables.

Chapter 6

Conclusions

A systematic design method for engineering the dispersive properties of periodic wave-supporting media is developed, leading to novel metamaterial designs.

The design problems are cast as dispersion-constrained inverse problems, where two objective functionals are proposed to serve different design objectives: (1) a discriminant-driven method suitable for band-gap designs only; and (2) a group velocity-driven method for general dispersion engineering.

The design/inversion variables can be chosen to be either the material properties or topology parameters, or both, of a unit cell of a periodic medium, thus allowing for a fairly flexible unit-cell design framework.

The proposed inversion methodology is demonstrated in settings involving scalar and vector waves, while time-domain simulations showed the subwavelength performance capabilities of narrow periodicity metastructures constructed using the inverted-for unit cells. It was further shown that the inversion methodology led to the design of metamaterials capable of exhibiting omni-directional band gaps in the presence of both P and SV waves.

Bibliography

[1] V. Akçelik, G. Biros, O. Ghattas, D. Keyes, K. Ko, L.-Q. Lee, and E.G. Ng. Adjoint methods for electromagnetic shape optimization of the low-loss cavity for the international linear collider. *Journal of Physics: Conference Series*, 16(1):435, 2005.

[2] B.B. Alagoz and S. Alagoz. Towards earthquake shields: a numerical investigation of earthquake shielding with seismic crystals. *Open Journal of Acoustics*, 1(03):63, 2011.

[3] A. Alù and N. Engheta. Achieving transparency with plasmonic and metamaterial coatings. *Physical Review E*, 72(1):016623, 2005.

[4] N.W. Ashcroft. *Solid State Physics*. Holt, Rinehart and Winston, 1976.

[5] S. Balay, S. Abhyankar, M.F. Adams, J. Brown, P. Brune, K. Buschelman, L. Dalcin, V. Eijkhout, W.D. Gropp, D. Kaushik, M.G. Knepley, L.C. McInnes, K. Rupp, B.F. Smith, S. Zampini, H. Zhang, and H. Zhang. PETSc users manual. Technical Report ANL-95/11 - Revision 3.7, Argonne National Laboratory, 2016.

[6] B. Banerjee. *An introduction to metamaterials and waves in composites*. CRC Press, 2011.

[7] G. Biros, L.F. Kallivokas, and S.-W. Na. Distributed parameter control of a 2D acoustic Helmholtz problem on a halfspace. In *XXI International Conference on Theoretical and Applied Mechanics (ICTAM04) - Special Sessions on Acoustics*, 2004.

[8] L. Brillouin. *Wave propagation in periodic structures: electric filters and crystal lattices*. McGraw-Hill Book Company, Inc., 1946.

[9] M. Brun, S. Guenneau, and A.B. Movchan. Achieving control of in-plane elastic waves. *Applied physics letters*, 94(6):061903, 2009.

[10] C. Campos and J. E. Roman. Parallel Krylov solvers for the polynomial eigenvalue problem in SLEPc. *SIAM J. Sci. Comput.*, 2016.

[11] D. Castelló-Lurbe, E. Silvestre, et al. Inverse dispersion engineering in silicon waveguides. *JOSA B*, 31(8):1829–1835, 2014.

[12] A.K. Chopra. *Dynamics of Structures: International Version*. Pearson Education, Limited, 2011.

[13] A. Climente, D. Torrent, and J. Sánchez-Dehesa. Gradient index lenses for flexural waves based on thickness variations. *Applied Physics Letters*, 105(6):064101, 2014.

[14] A. Colombi. Resonant metalenses for flexural waves in plates. *The Journal of the Acoustical Society of America*, 140(5):EL423–EL428, 2016.

[15] A. Colombi, D. Colquitt, P. Roux, S. Guenneau, and R. Craster. A seismic metamaterial: The resonant metawedge. *Scientific reports*, 6:27717, 2016.

[16] A. Colombi, S. Guenneau, P. Roux, and R.V. Craster. Transformation seismology: composite soil lenses for steering surface elastic Rayleigh waves. *Scientific reports*, 6:25320, 2016.

[17] M. Dubois, M. Farhat, E. Bossy, S. Enoch, S. Guenneau, and P. Sebbah. Flat lens for pulse focusing of elastic waves in thin plates. *Applied Physics Letters*, 103(7):071915, 2013.

[18] A. Fathi, L.F. Kallivokas, and B. Poursartip. Full-waveform inversion in three-dimensional PML-truncated elastic media. *Computer Methods in Applied Mechanics and Engineering*, 296:39 – 72, 2015.

[19] A. Fathi, B. Poursartip, and L.F. Kallivokas. Time-domain hybrid formulations for wave simulations in three-dimensional PML-truncated heterogeneous media. *International Journal for Numerical Methods in Engineering*, 101(3):165–198, 2015.

[20] G. Finocchio, O. Casablanca, G. Ricciardi, U. Alibrandi, F. Garescì, M. Chiappini, and B. Azzerboni. Seismic metamaterials based on isochronous mechanical oscillators. *Applied Physics Letters*, 104(19):191903, 2014.

[21] R. Fletcher and C. M. Reeves. Function minimization by conjugate gradients. *The Computer Journal*, 7(2):149–154, 1964.

[22] H. Goh and L.F. Kallivokas. Group velocity-driven inverse metamaterial design. *Journal of Engineering Mechanics*, 145(12):04019094, 2019.

[23] H. Goh and L.F. Kallivokas. Inverse metamaterial design for controlling band gaps in scalar wave problems. *Wave Motion*, 88:85 – 105, 2019.

[24] H. Goh and L.F. Kallivokas. Inverse band gap design of elastic metamaterials for P and SV wave control. *Computer Methods in Applied Mechanics and Engineering*, 2020 (submitted).

[25] M.E. Gurtin, E. Fried, and L. Anand. *The mechanics and thermodynamics of continua*. Cambridge University Press, 2010.

[26] J. Huang, W. Liu, and Z. Shi. Surface-wave attenuation zone of layered periodic structures and feasible application in ground vibration reduction. *Construction and Building Materials*, 141:1 – 11, 2017.

[27] M.I. Hussein, M.J. Leamy, and M. Ruzzene. Dynamics of Phononic Materials and Structures: Historical Origins, Recent Progress, and Future Outlook. *Applied Mechanics Reviews*, 66(4):040802–040802–38, May 2014.

[28] L.F. Kallivokas, A. Fathi, S. Kucukcoban, K.H. Stokoe, J. Bielak, and O. Ghattas. Site characterization using full waveform inversion. *Soil Dynamics and Earthquake Engineering*, 47:62 – 82, 2013.

[29] C. Kittel. *Introduction to solid state physics*. Wiley, 2005.

[30] S. Krödel, N. Thomé, and C. Daraio. Wide band-gap seismic metastructures. *Extreme Mechanics Letters*, 4:111–117, 2015.

[31] S. Kucukcoban, H. Goh, and L.F. Kallivokas. On the full-waveform inversion of lamé parameters in semi-infinite solids in plane strain. *International Journal of Solids and Structures*, 164:104 – 119, 2019.

[32] S. Kucukcoban and L.F. Kallivokas. A symmetric hybrid formulation for transient wave simulations in PML-truncated heterogeneous media. *Wave Motion*, 50(1):57 – 79, 2013.

[33] M. S. Kushwaha, P. Halevi, L. Dobrzynski, and B. Djafari-Rouhani. Acoustic band structure of periodic elastic composites. *Phys. Rev. Lett.*, 71:2022–2025, Sep 1993.

[34] K. J. Langenberg, R. Marklein, and K. Mayer. Energy vs. group velocity for elastic waves in homogeneous anisotropic solid media. In *2010 URSI International Symposium on Electromagnetic Theory*, pages 733–736, Aug 2010.

[35] C. Luo, S.G. Johnson, J.D. Joannopoulos, and J.B. Pendry. Subwavelength imaging in photonic crystals. *Phys. Rev. B*, 68:045115, Jul 2003.

[36] H. Mashayekh, L.F. Kallivokas, and J.L. Tassoulas. Parameter estimation in layered media using dispersion-constrained inversion. *Journal of Engineering Mechanics*, 144(11):04018099, 2018.

[37] F. Meseguer, M. Holgado, D. Caballero, N. Benaches, J. Sánchez-Dehesa, C. López, and J. Llinares. Rayleigh-wave attenuation by a semi-infinite two-dimensional elastic-band-gap crystal. *Physical Review B*, 59(19):12169, 1999.

[38] M. Miniaci, A. Krushynska, F. Bosia, and N.M. Pugno. Large scale mechanical metamaterials as seismic shields. *New Journal of Physics*, 18(8):083041, 2016.

[39] R.P. Moiseyenko and V. Laude. Material loss influence on the complex band structure and group velocity in phononic crystals. *Phys. Rev. B*, 83:064301, Feb 2011.

[40] F. R. Montero de Espinosa, E. Jiménez, and M. Torres. Ultrasonic band gap in a periodic two-dimensional composite. *Phys. Rev. Lett.*, 80:1208–1211, Feb 1998.

[41] A.B. Movchan, N.V. Movchan, I.S. Jones, and D.J. Colquitt. *Mathematical Modelling of Waves in Multi-Scale Structured Media*. Chapman & Hall/CRC Monographs and Research Notes in Mathematics. CRC Press, 2017.

[42] I. Newton. *Philosophiae Naturalis Pincipia Mathematica ("Mathematical Principles of Natural Philosophy"*. 1687,1713,1726.

[43] A.N. Norris. Acoustic cloaking theory. In *Proceedings of the Royal Society of London A: Mathematical, Physical and Engineering Sciences*,

volume 464, pages 2411–2434. The Royal Society, 2008.

[44] A. Palermo, S. Krödel, K.H. Matlack, R. Zaccherini, V.K. Dertimanis, E.N. Chatzi, A. Marzani, and C. Daraio. Hybridization of guided surface acoustic modes in unconsolidated granular media by a resonant metasurface. *Phys. Rev. Applied*, 9:054026, May 2018.

[45] J. B. Pendry. Negative refraction makes a perfect lens. *Phys. Rev. Lett.*, 85:3966–3969, Oct 2000.

[46] J.B. Pendry, A. Aubry, D.R. Smith, and S.A. Maier. Transformation optics and subwavelength control of light. *science*, 337(6094):549–552, 2012.

[47] C.G. Poulton, A.B. Movchan, R.C. McPhedran, N.A. Nicorovici, and Y.A. Antipov. Eigenvalue problems for doubly periodic elastic structures and phononic band gaps. *Proceedings of the Royal Society of London. Series A: Mathematical, Physical and Engineering Sciences*, 456(2002):2543–2559, 2000.

[48] X. Qian and O. Sigmund. Isogeometric shape optimization of photonic crystals via Coons patches. *Computer Methods in Applied Mechanics and Engineering*, 200(25):2237 – 2255, 2011.

[49] A. Quarteroni, R. Sacco, and F. Saleri. *Numerical mathematics*, volume 37. Springer Science & Business Media, 2010.

[50] Lord Rayleigh. Xvii. on the maintenance of vibrations by forces of double frequency, and on the propagation of waves through a medium endowed with a periodic structure. *The London, Edinburgh, and Dublin Philosophical Magazine and Journal of Science*, 24(147):145–159, 1887.

[51] J. E. Roman, C. Campos, E. Romero, and A. Tomas. SLEPc users manual. Technical Report DSIC-II/24/02 - Revision 3.7, D. Sistemes Informàtics i Computació, Universitat Politècnica de València, 2016.

[52] C.J. Rupp, A. Evgrafov, K. Maute, and M.L. Dunn. Design of phononic materials/structures for surface wave devices using topology optimization. *Structural and Multidisciplinary Optimization*, 34(2):111–121, Aug 2007.

[53] H. Sadeghi and S. Nemat-Nasser. Design optimization of layered periodic composites for desired elastodynamic response. In T. Kundu, editor, *Proc. SPIE, Health Monitoring of Structural and Biological Systems*, volume 9438, pages 94380T1– 94380T8, 2015.

[54] K. Sakoda. *Optical properties of photonic crystals*, volume 80. Springer Science & Business Media, 2004.

[55] D. Schurig, J. J. Mock, B. J. Justice, S. A. Cummer, J.B. Pendry, A.F. Starr, and D.R. Smith. Metamaterial electromagnetic cloak at microwave frequencies. *Science*, 314(5801):977–980, 2006.

[56] O. Sigmund and J. Søndergaard Jensen. Systematic design of phononic band–gap materials and structures by topology optimization. *Philo-*

sophical Transactions of the Royal Society of London A: Mathematical, Physical and Engineering Sciences, 361(1806):1001–1019, 2003.

[57] M. Stone and P. Goldbart. *Mathematics for physics: a guided tour for graduate students*. Cambridge University Press, 2009.

[58] X. Su, Z. Lu, and A.N. Norris. Elastic metasurfaces for splitting sv- and p-waves in elastic solids. *Journal of Applied Physics*, 123(9):091701, 2018.

[59] D. Torrent, Y. Pennec, and B. Djafari-Rouhani. Omnidirectional refractive devices for flexural waves based on graded phononic crystals. *Journal of Applied Physics*, 116(22):224902, 2014.

[60] V. Červený and I. Pšenčík. Energy flux in viscoelastic anisotropic media. *Geophysical Journal International*, 166(3):1299–1317, 2006.

[61] P.-R. Wagner, V.K. Dertimanis, E.N. Chatzi, and J.L. Beck. Robust-to-uncertainties optimal design of seismic metamaterials. *Journal of Engineering Mechanics*, 144(3):04017181, 2018.

[62] Y. Wang, Z. Luo, N. Zhang, and Z. Kang. Topological shape optimization of microstructural metamaterials using a level set method. *Computational Materials Science*, 87:178 – 186, 2014.

Vita

Heedong Goh received Bachelor of Science and Master of Science degrees in Civil Engineering at Seoul National University. He then joined the doctoral program in the Department of Civil, Architectural and Environmental Engineering at The University of Texas at Austin.

In his free time in Austin, he enjoyed listening to music by Bach, Scarlatti, Mozart, Prokofiev, Piazzolla, and Seo Yoon Kim. He also loved to hear sounds of birds[1], insects[2], amphibians, mammals, winds, rains, thunders, trains, a drummer in his neighbor, and a gorgeous New York strip steak in a smoking hot pan.

Address: heedong.goh@utexas.edu

This manuscript was typed by the author.

[1] grackles, starlings, cardinals, mockingbirds, blue jays, chickadees, finches, crows, hawks, flycatchers, parakeets, doves, ducks, woodpeckers, and other birds he could not identify

[2] except for a roach accidentally trapped inside an Amazon delivery box trying to escape